MODELING ELASTIC ANISOTROPY IN DIFFRACTION EXPERIMENTS USING FINITE ELEMENTS

A Dissertation

Presented to the Faculty of the Graduate School

of Cornell University

in Partial Fulfillment of the Requirements for the Degree of

Doctor of Philosophy

by

Hadas Ritz

August 2008

MODELING ELASTIC ANISOTROPY IN DIFFRACTION EXPERIMENTS USING FINITE ELEMENTS

Hadas Ritz, Ph.D.

Cornell University 2008

The focus of this work is on the elastic response of cubic polycrystals, particularly aluminum alloys, as explored through neutron diffraction with *in situ* mechanical loading, coupled with elastoplastic finite element simulations. It includes a set of data from experiments, an initial set of finite element simulations of those experiments, an expanded suite of simulations to explore the effects of grain discretization on the results, and a new method of stress estimation from diffraction experiments.

Chapter 1 includes an explanation of the methods used along with a presentation of the experimental data referred to throughout the work. It contains the material from [1]. The experiments are neutron diffraction with *in situ* uniaxial tension loading of aluminum-magnesium alloys of various compositions. The data are reduced with an emphasis on observing elastic anisotropy in the materials.

The second and third chapters cover finite element simulation of the experiments. Chapter 2 describes the simulation framework along with results from simulations of the experiments using dodecahedral grain definitions. The ability of the simulations to capture the elastically anisotropic behavior of the materials is discussed. Chapter 3 expands the set of simulations to include meshes with different grain discretizations. It demonstrates the different results that are possible with respect to capturing stress variations within a polycrystal aggregate.

A method of estimating stresses in various sets of crystals from diffraction

experiments based on the yield surface of face-centered cubic single crystals in presented in Chapter 4. The method requires no knowledge of material properties and represents an improvement over an assumption of the macroscopic stress state being identical to that of all crystals.

The final chapter is a brief summary of the preceding chapters highlighting the main findings.

BIOGRAPHICAL SKETCH

Hadas Ritz was born and raised a townie in Urbana, IL. There she developed a love of corn, flat land, and the environment of a college town. She attended the University of Illinois at Urbana-Champaign, majoring in Mechanical Engineering, minoring in Mathematics, and graduating with a Bachelor of Science degree in May 2001. She moved to Ithaca, "the Urbana of New York," in August 2001 to begin her graduate work at Cornell.

To my family, especially my father, Dr. Zvi Ritz.

I know at times you worried you wouldn't see this.

I'm so glad you will.

ACKNOWLEDGEMENTS

Funding for this work has been provided by a National Science Foundation graduate research fellowship and ONR grant number #N00014-03-1-0250. Thanks to the Journal of Neutron Research for allowing use of a portion of this work which has previously appeared there in a slightly modified form [1]. The Center for Advanced Computing (formerly Cornell Theory Center) provided computing resources; thanks to Daniel Sverdlik and Linda Callahan there for their help. Neutron diffraction experiments were performed in Chalk River, Ontario, Canada at the NRU reactor. Thanks to instrument scientist Ron Rogge for his help with the experiments and his tips on keeping warm in -40° (Fahrenheit or Celsius, take your pick) weather.

Thanks to Prof. Leigh Phoenix for serving on my special committee. Thanks to Marcia Sawyer who has solved bureaucratic problems, large and small, for me. Thanks to all of my colleagues in DPLab over the years, particularly Joel Bernier and Tito Marin, whose valued friendship and camaraderie made even my most difficult times at Cornell both easier and more enjoyable. Donald Boyce has been ever patient with my questions and generous with his time. Both the contents and presentation of this document are much improved due to his expertise and assistance.

Matthew Miller taught me a lot about how to be a better teacher during my experiences as a TA for his classes and always provided honest and valuable feedback on my research and writing in his role as special committee member. Thanks to him for all of his help and advice.

My special committee chairman, Paul Dawson, has gone above and beyond the call of duty of academic advisor. In addition to his extensive and integral advice and collaboration in all aspects of this work, I greatly appreciate the steps he took

to assist me during an unexpected medical situation I faced. His matter-of-course help during that time significantly reduced my stress and means a lot to me.

I could never have completed this work without the love and support of my family. Thanks to my parents for trying their best to keep their encouragement on the constructive rather than the harrying side. Thanks to my siblings who gave me just enough of a hard time and always dangled the carrot of trips to Las Vegas as rewards for hard work. My visits home to Illinois have always been wonderfully fun and restorative. Thanks also to my new New York family who have welcomed me with open arms. April Peress has provided a much-appreciated home away from home. My first four-legged family member, Da Bubba, created a new cat-shaped place in my heart. I miss you very much, Bubba. And I don't know where to begin to thank Irina Peress for all she has done for me during the past six years. Her unconditional love and support has been an enormous factor in whatever success I have achieved. I love all of you very much.

TABLE OF CONTENTS

LIST OF TABLES

LIST OF FIGURES

CHAPTER 1

MEASURING THE INFLUENCE OF MAGNESIUM ON THE ELASTIC ANISOTROPY OF ALUMINUM USING *IN SITU* NEUTRON DIFFRACTION EXPERIMENTS

1.1 Introduction

Polycrystalline metals comprise an important class of engineering materials, and accurately predicting their response to mechanical manipulation and loading allows increased efficiency in their forming and utilization. Modelling on the polycrystal, or aggregate, level gives insight into material behaviours such as orientational texture evolution and formation of residual stresses. Here, an aggregate is a group of crystals that act collectively to define the bulk behaviour. Understanding the micromechanical state of materials can lead to improved ability to predict failure which can often result from damage on the grain scale, including for example microcracking and void formation which tend to occur at highly stressed locations within an aggregate. Any computer simulation can only be trusted in as much as it is able to accurately predict behaviors observable in a physical experimental setting. In using experiments and simulations together there are benefits to each. If experimental results can be explained through the use of simulations that have a theoretical basis in physical phenomena, those experimental results can be located in a larger framework in terms of material properties or behaviors. Theoretical models can be used to relate results from different experiments to each other in this way. In terms of model validation, using simulations to mimic experiments and accurately predicting some aspects of the behaviors gives confidence that other behaviors more easily explored through simulation than through experiment may also be accurately predicted. For example, if a model is able to accurately predict

the lattice strains in some groups of crystals, as verified by experiments, then there is greater confidence that the stress distribution throughout the simulated domain may also reflect a physically realistic response. In this work the simulations are all finite element analyses and the experiments are neutron diffraction with *in situ* mechanical loading of aluminum alloys.

All models have target applications and assessing the fidelity of a model involves determining its accuracy within its scope. The targeted behavior of the finite element (FE) model considered here is the elastoplastic response of polycrystalline materials under mechanical loading at moderate strain rates. The specifics of that model come from [2, 3] and are described in §2.1. The experiments used throughout this work are described in detail in this chapter.

Diffraction (x-ray or neutron) provides lattice spacing data. Using changes in the spacing during *in situ* mechanical loading, individual components of the lattice (elastic) strain can be determined. The crystal stress may be evaluated directly from the strain using Hooke's law, provided the strain tensor is completely determined and the single crystal properties are well known. Lattice strains can be measured within a single grain via micro-diffraction or for sets of crystals corresponding to a particular crystallographic fiber via bulk diffraction. From these data, it is possible to quantify, for example, the elastic anisotropy via directional diffraction elastic moduli, and the variability of strain, either between grains of different orientation (using bulk diffraction) or within small sets of grains (using micro-diffraction). In the past there has been incomplete success in predicting the degree of elastic anisotropy that manifests during deformation [4, 5]. The FE simulations tend to show less difference in lattice strains between crystals with different orientations relative to the experiments. The main impetus of this work is exploring how the elastic anisotropy can be captured in both diffraction and the

FE simulations. The experiments presented in this chapter focus on whether part of the discrepancy between simulation and experiment in this regard can be attributed to physical changes in the single crystal material properties upon alloying, as has been suggested in the past [6]. All materials considered are aluminum alloys with small amounts of added magnesium as the only alloying element. The Al-Mg system was chosen as a simple version of the AA-5182 alloy studied in [4]. These simpler alloys are single phase materials with face-centered cubic (FCC) structure throughout.

1.2 Diffraction measurements during *in situ* mechanical loading

In situ diffraction experiments consist of macroscopically loading a specimen through a predetermined deformation path and performing diffraction measurements at various loads. Typically the macroscopic loading is uniaxial in nature and can be either tensile or compressive, though other types of loading are possible, such as high temperature and pressure [7, 8]; here the loading is uniaxial tension. Both x-ray diffraction (XRD) and neutron diffraction (ND) are useful tools, each with their own strengths [9]. The specimens used in these experiments, described in detail in §2.2.3, have large grains ($\sim 200 - 1000\mu$m) which demand large sampling volumes to improve the statistical significance of the diffraction data. This need favors the use of neutrons, which typically have a larger penetration depth, over x-rays [10].

The ND measurements themselves consist of lattice strains at certain macroscopic stress levels. Since these are uniaxial tension experiments, the macroscopic stress value is simply the force applied, measured by a load cell, divided by the

initial specimen cross-sectional area, measured before the test begins. The lattice strains are found by taking advantage of Bragg's law [11]:

$$n\lambda = 2\bar{d}_{hkl} \sin \bar{\theta}_{hkl}, \tag{1.1}$$

where n is an integer, λ is the wavelength of the incoming radiation, $\bar{\theta}_{hkl}$ is the diffraction angle (or Bragg angle), and $\bar{d}_{hkl}$ is the spacing between $\{hkl\}$ lattice planes. The measured spacing, $\bar{d}_{hkl}$, is compared to the reference spacing, $\bar{d}^0_{hkl}$, (measured at a nominally zero load prior to any deformation) through equation 1.2 to determine the average normal component of lattice strain on $\{hkl\}$ planes in the scattering direction, $\epsilon^D_{\langle hkl \rangle}$,

$$\epsilon^D_{\langle hkl \rangle} = \frac{\bar{d}_{hkl} - \bar{d}^0_{hkl}}{\bar{d}^0_{hkl}}. \tag{1.2}$$

Taking into account equation 1.1, equation 1.2 can be rewritten as:

$$\epsilon^D_{\langle hkl \rangle} = \frac{\sin \bar{\theta}^0_{hkl}}{\sin \bar{\theta}_{hkl}} - 1, \tag{1.3}$$

where $\bar{\theta}^0_{hkl}$ is the reference angle corresponding to $\bar{d}^0_{hkl}$.

During a ND experiment for a particular $\langle hkl \rangle$[1], constructive interference consistent with Bragg's law occurs along a fiber in orientation space defined by:

$$\mathbf{R}\boldsymbol{c} = \pm \boldsymbol{s}, \tag{1.4}$$

where $\mathbf{R}$ is the orientation matrix of a crystal, $\boldsymbol{c}$ is the crystallographic direction corresponding to the $\langle hkl \rangle$ currently under consideration, and $\boldsymbol{s}$ is the sample direction corresponding to the scattering vector, usually aligned either parallel or normal to the uniaxial tension axis. The diffraction measurements cannot distinguish between grains satisfying equation 1.4. Therefore, in diffraction of bulk specimens where the radiation beam covers a large volume of the specimen all $\bar{\theta}_{hkl}$

[1]In the cubic crystals considered here, $\langle hkl \rangle$ is always the direction perpendicular to the $\{hkl\}$ planes, and the convention of uvw to denote directions is not used.

and $\bar{d}_{hkl}$ measurements are averages over groups of crystals, including both crystals with identical orientations and crystals related by a simple rotation about the $\boldsymbol{s}$ axis. The overbar notation $(\bar{\cdot})$ emphasizes this averaging. Furthermore, there is a certain amount of experimental leeway in the alignment necessary between $\boldsymbol{c}$ and $\boldsymbol{s}$ to contribute to a measurement. Equation 1.4 need not be satisfied exactly, but an alignment between $\boldsymbol{c}$ and $\boldsymbol{s}$ within a small angular range (up to as much as 5° for certain experiments, though typically more on the order of 0.5° [10]) results in a contribution to the diffraction measurement. An example of a measured diffraction peak is shown in figure 1.1. The individual data points are counts from the detector at each specific angle. A Gaussian distribution is fit to the measured data, and the center of that peak is $\bar{\theta}_{hkl}$. The peak intensity is related to the multiplicity of the (hkl) under consideration and the length of time that the detector was counting and is not a factor for this study.

1.3 Elastic anisotropy

The lattice strains as measured by bulk ND experiments will in general show different levels of strain for different crystallographic fibers. This is for the most part due to elastic anisotropy, though grain morphology and crystallographic texture can also play a significant role. There are two manifestations of elastic anisotropy of concern in this study. The first is the single crystal elastic anisotropy and the second is the diffraction anisotropy, which is measured from a bulk polycrystal. If grain interactions had no effect on the deformation response of each individual grain within a polycrystal aggregate the diffraction anisotropy would closely mimic the single crystal value, but as will be shown in §3.4.1 that is not the case.

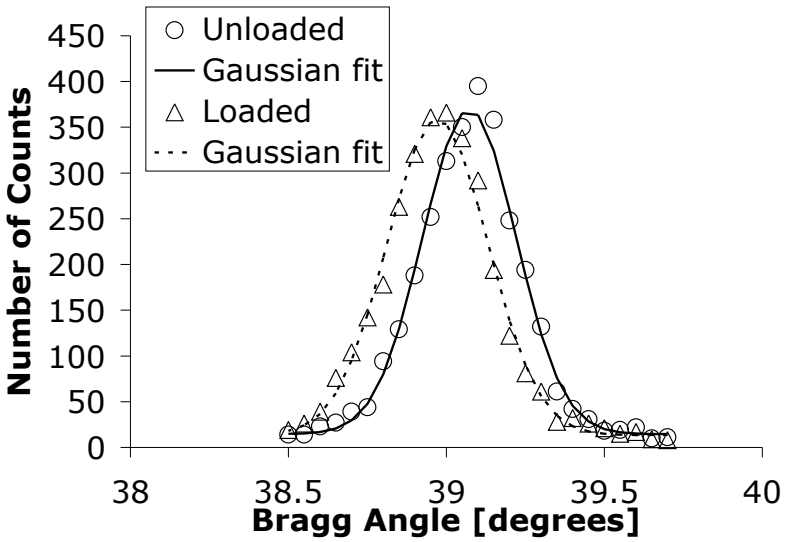

Figure 1.1: A typical measured diffraction peak, both unloaded and under load, along with Gaussian distributions fit to the data. The individual data points refer to the number of neutrons detected at the corresponding Bragg angle during a diffraction measurement.

1.3.1 Single crystal

The single crystal elastic anisotropy, r_E,

$$r_E = \frac{E_{\langle 111 \rangle}}{E_{\langle 100 \rangle}}, \tag{1.5}$$

is defined in the context of uniaxial tension tests on single crystal specimens that have been manufactured with their tension axes aligned with particular crystallographic directions. In equation 1.5, $E_{\langle hkl \rangle}$ is Young's modulus in the $\langle hkl \rangle$ crystallographic direction,

$$E_{\langle hkl \rangle} = \frac{\sigma_{\langle hkl \rangle}}{\epsilon_{\langle hkl \rangle}}. \tag{1.6}$$

Here $\sigma_{\langle hkl \rangle}$ and $\epsilon_{\langle hkl \rangle}$ are the normal components of crystal stress and lattice strain, respectively, along the $\langle hkl \rangle$ direction which is the tension axis in the single crystal uniaxial experiment. In face-centered cubic (FCC) materials, $\langle 111 \rangle$ is typically the stiffest direction and $\langle 100 \rangle$ the most compliant; the ratio of the moduli in those two directions gives the greatest anisotropy for the material for a given loading. The property r_E is defined entirely on the single crystal scale and values for various materials can be found in handbooks. Typical values in metals include approximately 1 in tungsten, 2.1 in iron, and 2.9 in copper; aluminum is reported as having r_E=1.2 [12].

1.3.2 Polycrystal

The second important manifestation of elastic anisotropy is the diffraction anisotropy, r_D, which is the value found from ND experiments on polycrystals and is inherently multiscale in nature. Lattice strains are measured in groups of crystals instead of in single grains. Therefore, $\epsilon_{\langle hkl \rangle}$ is unavailable, and the lattice strains must instead be $\epsilon^D_{\langle hkl \rangle}$ from equation 1.2. Also, since the particular stresses that are present in the individual grains are unknown, $\sigma_{\langle hkl \rangle}$ is unavailable as well. The stress in the

calculation must instead be σ_{macro}, which is the axial component of the macroscopic engineering stress applied to the test specimen. Using these values, the diffraction modulus in the $\langle hkl \rangle$ direction, $E^D_{\langle hkl \rangle}$, is:

$$E^D_{\langle hkl \rangle} = \frac{\sigma_{\text{macro}}}{\epsilon^D_{\langle hkl \rangle}}. \tag{1.7}$$

Further, r_D may now be defined as,

$$r_D = \frac{E^D_{\langle 111 \rangle}}{E^D_{\langle 100 \rangle}}. \tag{1.8}$$

From equations 1.7 and 1.8 it would appear that r_D could also be calculated simply as $\epsilon^D_{\langle 100 \rangle}/\epsilon^D_{\langle 111 \rangle}$ since σ_{macro} appears in both the numerator and the denominator, but in general diffraction measurements of different (hkl)s are not made simultaneously. Though the nominal desired load may be identical between measurements, the actual load, and therefore the actual σ_{macro}, may differ and equation 1.8 should be used.

Clearly, r_D is far from the single crystal property r_E. In addition to linking scales between the macroscopic stress and the lattice strains, r_D is also a product of averaging responses in groups of largely independent crystals, each of which is subjected to a slightly different micromechanical stress state from its physical neighbors within the aggregate. While the diffraction anisotropy is influenced by the single crystal value, the two are not expected to be equal. Studies have also shown that lattice strains measured after plastic deformation can exhibit different behavior than those measured during purely elastic deformation, further complicating measurement of elastic anisotropy [13–15]. The FE simulations utilized here provide a method of connecting r_D to r_E. This gives an indication of what single crystal value may be present when the experimentally measured results are found.

The method of determining r_D from experimental data is essentially to take a ratio of slopes, each of which relates a change in macroscopic stress to a change

in directional lattice strain. The ND experiments collect lattice strains as in equation 1.2, which can then be plotted against the scalar value of macroscopic stress at which they are measured. When that process is repeated for each measurement of a specific lattice direction, a plot such as figure 1.2(a) results. A simple linear regression can then be performed on the data, and the slope of the fit line, as shown in figure 1.2(b), is identified as $E^D_{\langle hkl \rangle}$.

In FCC materials diffraction only occurs off of planes in which the (hkl) are either all even or all odd [16]. Therefore, the $\{111\}$ planes can create a diffraction peak but the $\{100\}$ planes cannot. In practice each material will produce different peaks at more or less convenient angles for each particular experimental set-up. Measuring either $\epsilon^D_{\langle 111 \rangle}$ or $\epsilon^D_{\langle 222 \rangle}$ should produce the same results for $E^D_{\langle 111 \rangle}$ within experimental accuracy since the same physical lattice planes are involved in both diffraction peaks. For the particular experimental set-up employed here (and described in detail in §1.4), the most convenient planes were $\{222\}$ and $\{400\}$. The process described above for calculating $E^D_{\langle hkl \rangle}$ is repeated for $\{222\}$ and $\{400\}$ planes, which provide $E^D_{\langle 111 \rangle}$ and $E^D_{\langle 100 \rangle}$, respectively. Taking the ratio of these two values gives r_D for the sample.

1.3.3 Relating r_E to single crystal elastic moduli

In addition to relating anisotropy to directional Young's moduli, it is also possible to begin with the single crystal elastic stiffness matrix, $\mathbb{C}$, to define r_E. The elastic stiffness matrix relates stress in the single crystal to strain as follows:

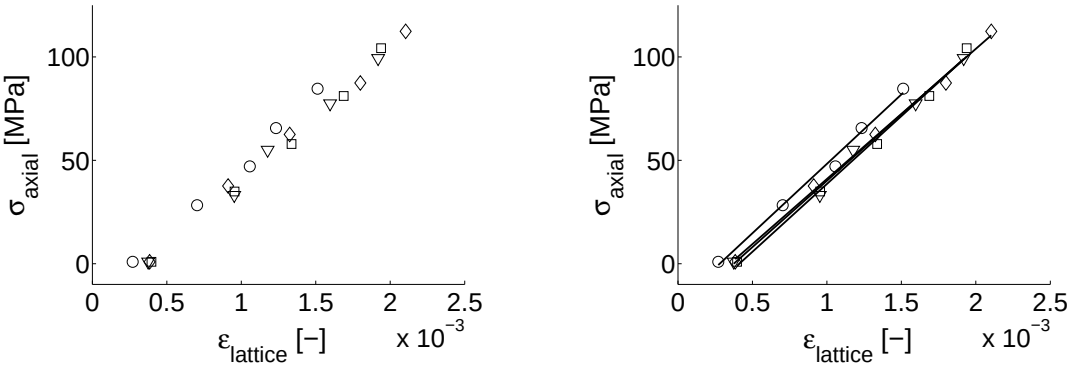

(a) Measured data.

(b) Data with linear fits to each unloading episode.

Figure 1.2: Each measurement of lattice strain in the $\langle 222 \rangle$ direction in the 2%Mg specimen. The slopes of the fit lines in (b) are values of $E^D_{\langle 222 \rangle}$. The different symbols represent separate unloading episodes.

$$\begin{Bmatrix} \sigma_{xx} \\ \sigma_{yy} \\ \sigma_{zz} \\ \sigma_{xy} \\ \sigma_{yz} \\ \sigma_{xz} \end{Bmatrix} = \mathbb{C} \begin{Bmatrix} \epsilon_{xx} \\ \epsilon_{yy} \\ \epsilon_{zz} \\ \epsilon_{xy} \\ \epsilon_{yz} \\ \epsilon_{xz} \end{Bmatrix} \qquad \text{with} \qquad \mathbb{C} = \begin{bmatrix} c_{11} & c_{12} & c_{12} & 0 & 0 & 0 \\ c_{12} & c_{11} & c_{12} & 0 & 0 & 0 \\ c_{12} & c_{12} & c_{11} & 0 & 0 & 0 \\ 0 & 0 & 0 & c_{44} & 0 & 0 \\ 0 & 0 & 0 & 0 & c_{44} & 0 \\ 0 & 0 & 0 & 0 & 0 & c_{44} \end{bmatrix}, \tag{1.9}$$

where the x, y, and z directions are aligned with the crystal axes. Equation 1.9 applies for cubic crystals; other crystal symmetries result in different components in the $\mathbb{C}$ matrix. Using this matrix of crystal stiffnesses the single crystal anisotropy can be defined as:

$$r_E = \frac{\frac{3}{2} c_{44}(c_{11} + c_{12})}{(c_{11} - c_{12})(c_{11} + 2c_{12} + \frac{1}{2} c_{44})}. \tag{1.10}$$

The sensitivity of r_E to each of the three crystal stiffnesses is not the same. The anisotropy is more sensitive to changes in c_{11} and c_{12} than to changes in c_{44}, as

figure 1.3 demonstrates. Therefore, uncertainty in measurements of these moduli can have a significant impact on handbook values of anisotropy.

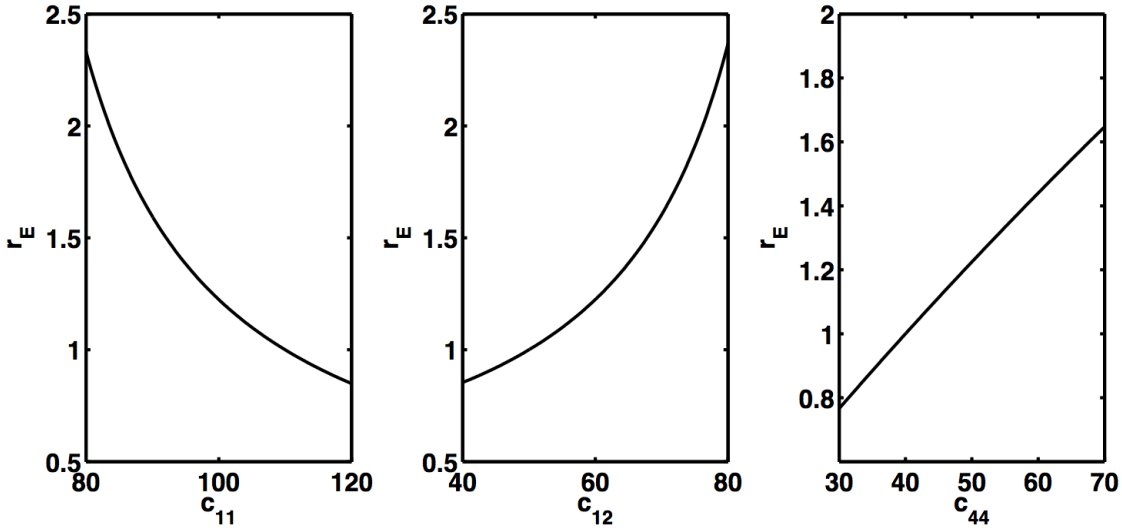

Figure 1.3: Changes in r_E due to changes in the three crystal stiffnesses. For each subfigure the remaining two stiffnesses have been held constant. The values shown range near the nominal values for aluminum.

1.4 *In situ* neutron diffraction experiments

This section describes the particular suite of experiments referred to throughout this study. It includes a description of the materials, the particular settings for the diffraction measurements themselves, the deformation history applied to each specimen, and the method of texture measurement.

1.4.1 Material composition and preparation

All of the materials tested were predominantly pure aluminum with small amounts of pure magnesium added. Table 1.1 shows some relevant handbook properties

Table 1.1: Basic properties of interest of aluminum and magnesium. Lattice parameters from [18] and anisotropy ratios from [12, 20].

Material	Crystal Structure	Lattice Parameter [Å]	Anisotropic Ratio
Aluminum	Face-Centered Cubic	a=4.049	1.22
Magnesium	Hexagonal	a=3.210, c=5.211	1.24

of aluminum and magnesium. The samples were all taken from castings in a book mold with approximate dimensions of 3×20×30 cm. The resulting blocks of material had a grain structure with varying grain size as is characteristic of cast parts: columnar grains grown in the direction of heat flux near the edges and smaller, nearly equiaxed grains in a region nearer the center [17]. The tensile samples were taken from a plane approximately 5 cm from the bottom of the mold at a point where the grains were relatively equiaxed.

The complete set of samples included some larger grained materials and some with TiB added as a grain refiner. The larger grained samples included 99.999% pure aluminum with 0, 2, 5, and 8% magnesium added. The three smaller grained materials had 0.5, 1.0, and 2.0% Mg. Micrographs of the larger grained samples indicate that some of the magnesium was not incorporated into the aluminum lattice but was present at grain boundaries, most likely in the form of the intermetallic compound Mg_5Al_8 [18]. At room temperature the maximum solubility of magnesium in aluminum is approximately 2% [19]. The grains in these samples were smallest (on the order of 200 μm) for the 2.0% magnesium (with TiB) and largest (on the order of 1000 μm) for the pure aluminum. The tension specimens had gauge sections of dimension 0.6×1.0×5.1 cm. These relatively large grain sizes affected the actual neutron diffraction as described below.

1.4.2 Diffraction measurement

The *in situ* diffraction experiments were performed with a uniaxial loading rig and a monochromatic neutron beam at the NRU reactor in Chalk River, Ontario. For each material composition we tested two samples: one oriented to examine axial strains and the other to examine transverse strains. A monochromating crystal of germanium selected neutrons of wavelength $\lambda = 0.155$ nm. Considering the larger grain size, illuminating a sufficient number of grains with the neutron beam required a relatively large aperture of approximately 1.5×4 cm. Such a wide aperture, however, could allow increased angular spread in the beams. Both the incident and reflected neutron beams were collimated using cadmium-coated slits to counteract that effect. The detector moved over a range of 2-3 degrees to capture the entire pattern of the Gaussian peak. One additional measure taken to increase the number of grains sampled was to oscillate the tension specimen through 4 degrees during the neutron counts. That oscillation increased the cone of orientations about the tension axis that contributed to the diffraction peak. This setup illuminated at least several thousand crystals during each test. In spite of these efforts to maximize the number of grains sampled, the resulting statistics on the pure aluminum samples were too poor to use. Slight changes in angle resulted in vastly different peak intensities, which indicates that the number of grains being illuminated was very small, and the data cannot be considered statistically significant. Table 1.2 shows the crystallographic planes examined along with their reference spacing and resulting peak position $\bar{\theta}^0_{hkl} = \sin^{-1} \lambda/2\bar{d}^0_{hkl}$ for a representative specimen. The reference spacings were all measured at a load of 50 N before any plastic strain had been introduced. That corresponds to a stress of approximately 0.8 MPa compared to a nominal yield strength of 35-130 MPa, depending on the magnesium content.

Table 1.2: Reference locations of diffraction peaks for several lattice planes in Al-2.0% Mg, as measured with a 50 N applied load. Changing the magnesium content shifts the reference peak positions by as much as 0.8 degrees.

(hkl)	$\bar{d}^0_{hkl}$ [Å]	$\bar{\theta}^0_{hkl}$ [degrees]
(220)	1.432	32.78
(311)	1.221	39.40
(222)	1.169	41.54
(400)	1.013	49.94

1.4.3 Loading history

The data of interest in these experiments all come from elastic loading (and unloading) of the samples. Each specimen was loaded to and unloaded at approximately 2%, 4%, and 6% macroscopic true strain, as shown in figure 1.4. During each of these unloading episodes five measurements of lattice strains for each of four (hkl)s were made. The lattice strains were measured at 90% of the peak load needed to achieve the macroscopic strain and again at 60%, 30%, 0%, and 60% of that peak load. The repetition of the point at 60% load was intended to verify that the unloading was indeed linear without any relaxation due to the hold time of approximately one hour at each load during neutron counting. The point at 0% of the load was actually measured with a 50 N load to avoid inadvertent compression of the specimens.

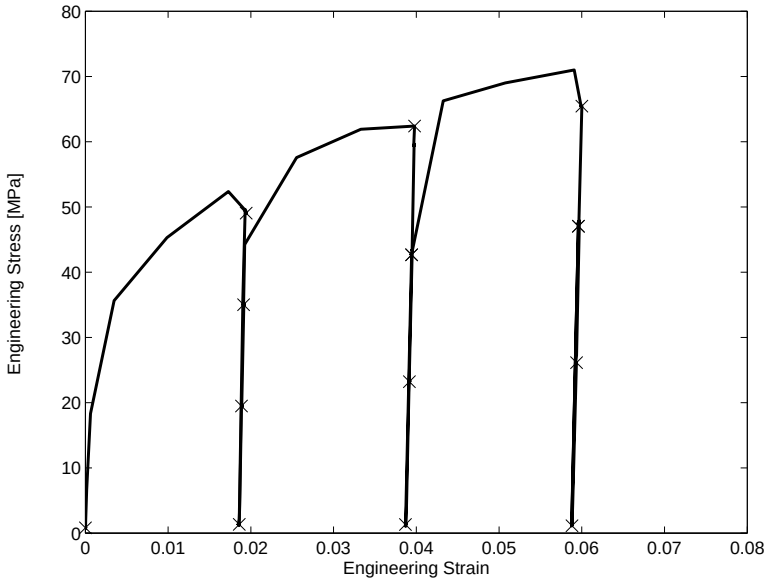

Figure 1.4: The macroscopic stress-strain curve from a representative sample (Al-2% Mg). The apparent jaggedness of the curve is due to a low sampling rate of data acquisition from the load cell; the actual loading was smooth.

1.4.4 Texture measurement

The final aspect of the experiments was measuring the crystallographic texture of the samples. The most important reason for measuring the texture is later comparison with finite element simulations, but even without the need for matching with simulations it was necessary to confirm that the initial texture was close to uniform (random). If a material has a significant texture, that may indicate that there are residual stresses, which would make measurements of reference lattice spacings inaccurate. Additionally, significant texture would influence the relationship between the crystal and diffraction moduli because of non-uniform neighborhoods of grains. After the first set of experiments on the 0%, 2%, 5%, and 8% magnesium samples, two cubes were cut from each tension specimen, one from the grip section and one from the gauge section. These cubes were each measured in a triple-axis

spectrometer at the NRU facility. Since deformation within the grip section was negligible, the grip section cubes represent the state of the materials before deformation. For all of the samples measured the change in texture was extremely mild. The grip sections showed no discernible pattern, and the gauge sections showed a weak pattern consistent with uniaxial extension to small total plastic strain. Figure 1.5 shows a representative set of pole figures from these materials.

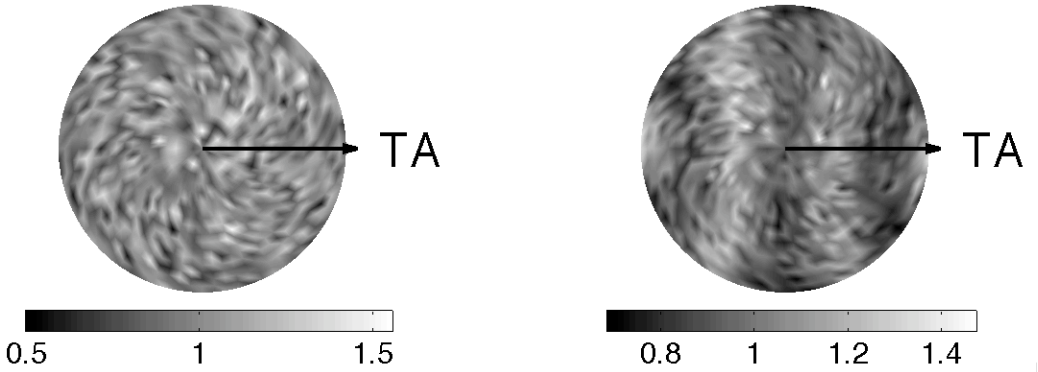

(a) Grip section. (b) Gauge section.

Figure 1.5: (200) Pole figures from a 2% Mg specimen. The tension axis is labeled and the scale is in multiples of a uniform distribution (MUD).

1.5 Experimental results and conclusions

The crystal lattice parameter, a, of the aluminum alloys increases slightly with increasing magnesium content. The lattice parameter for cubic crystals can be calculated from equation 1.11 as:

$$a = \bar{d}^0_{hkl}\sqrt{h^2+k^2+l^2} = \frac{\lambda}{2\sin\bar{\theta}^0_{hkl}}\sqrt{h^2+k^2+l^2}, \tag{1.11}$$

where h, k, and l are from the $\{hkl\}$ of the plane. Table 1.3 shows the lattice parameters calculated from the reference peak positions for each material. These

Table 1.3: Variation of the lattice parameter with magnesium content. The value for each material is the average of the values calculated from the four (hkl)s.

Magnesium content (%)	Lattice Parameter (Å)
0.5	4.0456
1.0	4.0480
2.0	4.0508
2	4.0640
5	4.0796
8	4.0894

values agree well with those found in [18]. Clearly, as the magnesium content increases, the lattice parameter also increases, which is to be expected based on the information in table 1.1.

Figures 1.6-1.8 show lattice strain versus macroscopic axial stress for the lower magnesium content materials. The dashed lines are least-squares fits to the data from each individual unloading episode. The slopes of these lines are the directional moduli. Figure 1.9 shows how the calculated moduli vary by unloading episode for each material. No clear trend is evident here relating increased specimen strain to a monotonic change in modulus. No one unloading episode appears any more or less reliable than the others. Therefore, we calculate the directional modulus in each direction for each material by averaging the values of the slopes over all of the individual unloading episodes. With the directional moduli in hand, we calculate r_D for each material as in equation 1.8. Figure 1.10 shows the trend in anisotropy over the range of composition. It includes a marker indicating r_D from the AA-5182 experiments in [4].

The first salient point from figure 1.10 is that the values are all lower than

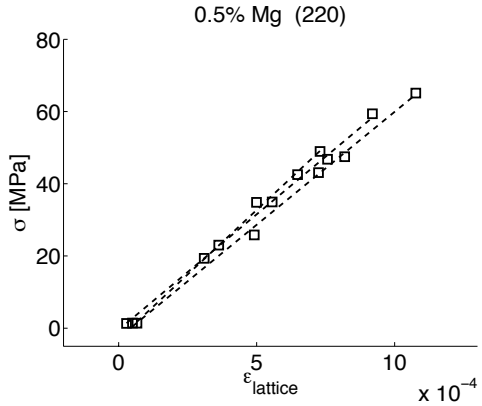

(a) Lattice strains normal to the (220) planes.

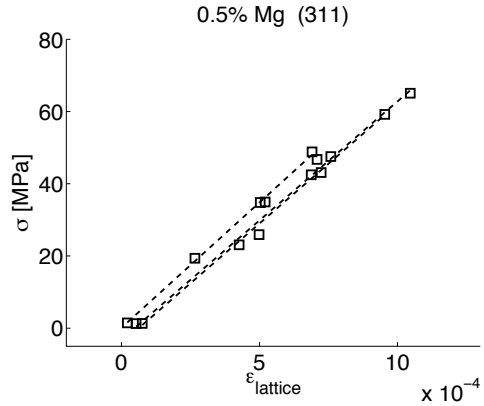

(b) Lattice strains normal to the (311) planes.

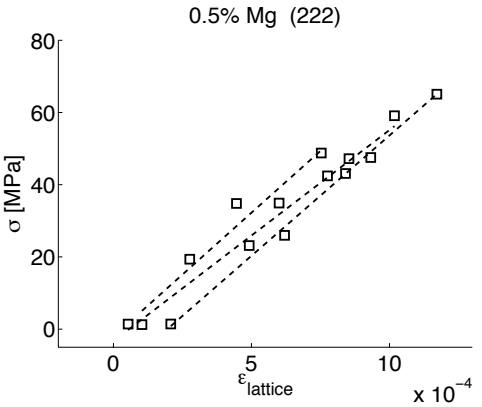

(c) Lattice strains normal to the (222) planes.

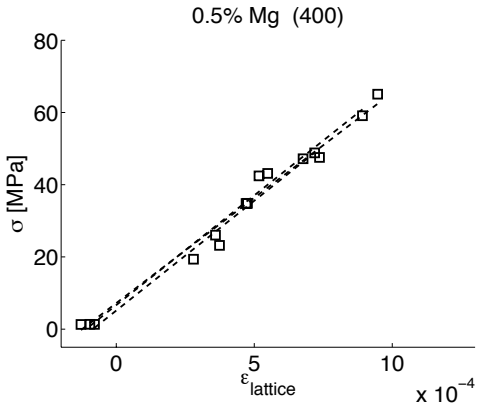

(d) Lattice strains normal to the (400) planes.

Figure 1.6: Lattice strain versus macroscopic stress for all lattice planes and unloading episodes for the Al-0.5% Mg axial scattering vector sample. The experimental data are marked as points, and the dashed lines are the least-squares fits to the individual unloading episodes.

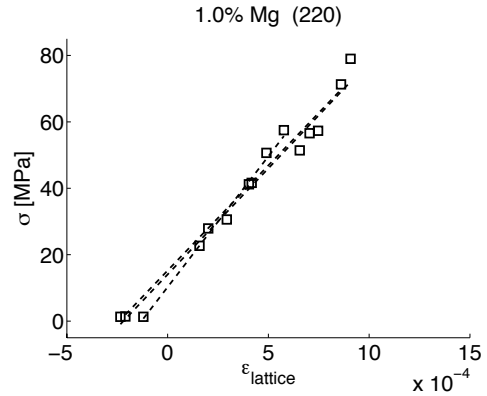

(a) Lattice strains normal to the (220) planes.

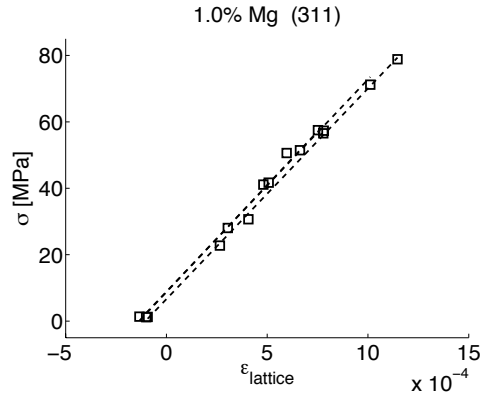

(b) Lattice strains normal to the (311) planes.

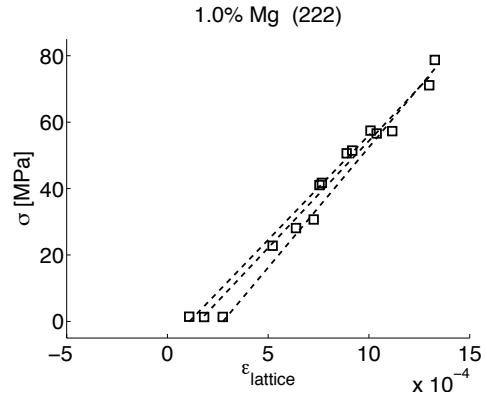

(c) Lattice strains normal to the (222) planes.

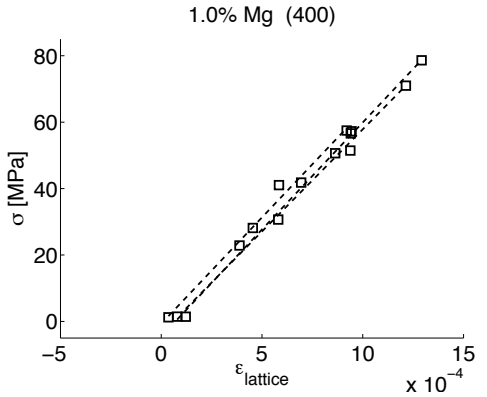

(d) Lattice strains normal to the (400) planes.

Figure 1.7: Lattice strain versus macroscopic stress for all lattice planes and unloading episodes for the Al-1% Mg axial scattering vector sample. The experimental data are marked as points, and the dashed lines are the least-squares fits to the individual unloading episodes.

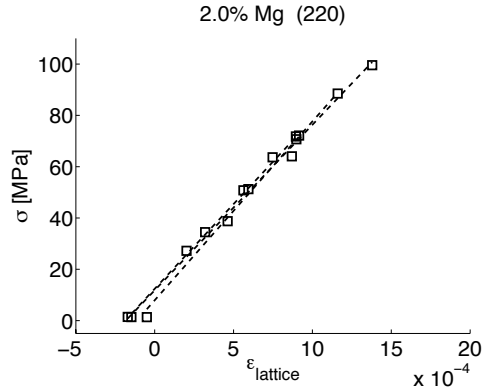

(a) Lattice strains normal to the (220) planes.

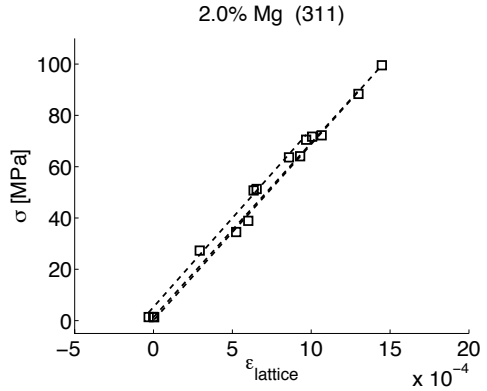

(b) Lattice strains normal to the (311) planes.

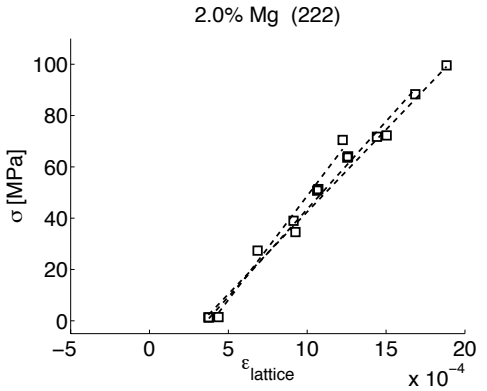

(c) Lattice strains normal to the (222) planes.

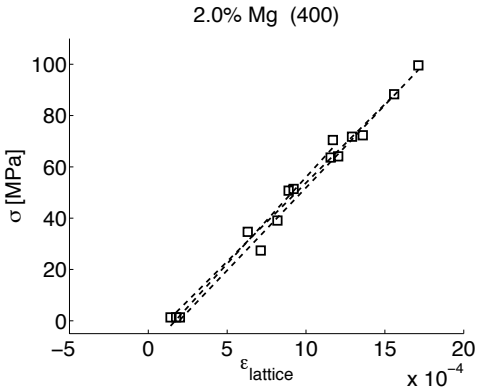

(d) Lattice strains normal to the (400) planes.

Figure 1.8: Lattice strain versus macroscopic stress for all lattice planes and unloading episodes for the Al-2% Mg (with smaller grain size) axial scattering vector sample. The experimental data are marked as points, and the dashed lines are the least-squares fits to the individual unloading episodes.

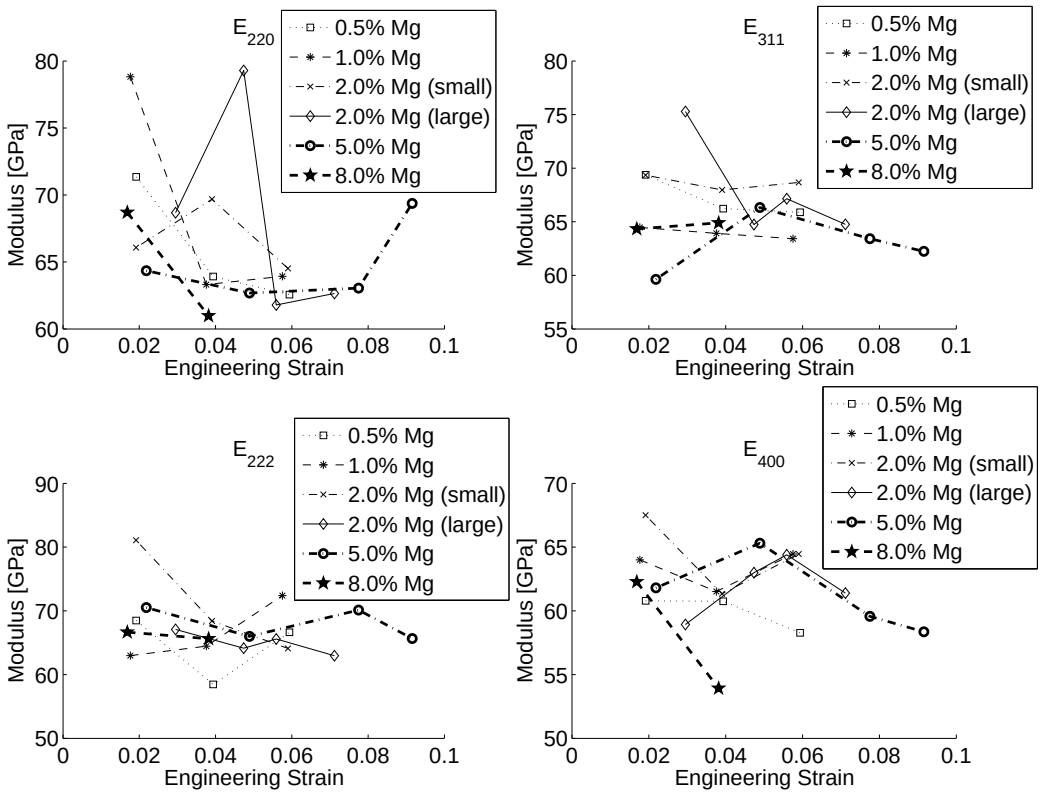

Figure 1.9: The directional moduli for each $\langle hkl \rangle$ and each material as a function of specimen strain at unloading.

the single crystal value for pure aluminum, which is expected. Experiments on bulk polycrystalline material do not isolate the single crystal response in any given direction. Each individual grain's response is influenced by its neighbors. This means that a grain that would normally appear compliant in the axial direction may be constrained by neighboring grains that are more stiff in that direction. Similarly, grains with a stiffer direction aligned axially may appear more compliant if surrounded by grains experiencing greater elongation. The overall effect is to shrink the range of apparent moduli and, therefore, the anisotropic ratio, in the polycrystal versus that in the single crystal. That said, these data can still indicate

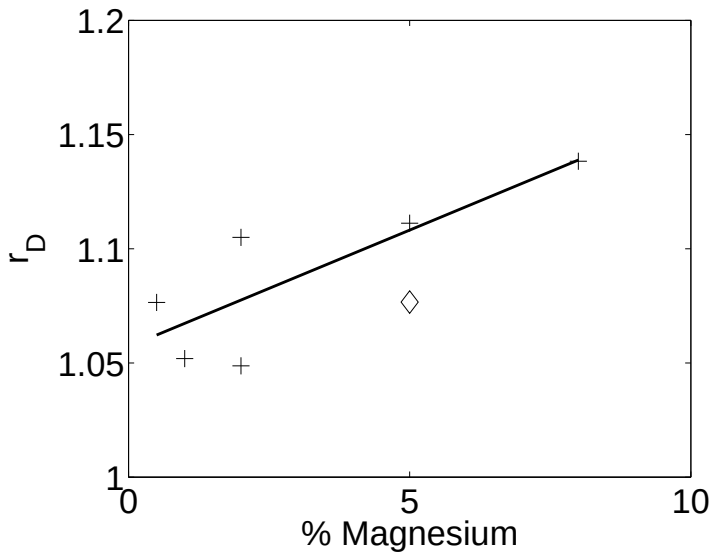

Figure 1.10: The anisotropic ratio, r_D, as a function of magnesium content. Each point is the calculated anisotropy for one material. The solid line is a least-squares fit of the data points. The diamond (not included in the fit data) indicates the anisotropic ratio of the AA-5182 from [4].

trends in the underlying material property. The averaging is sufficient to uncover significant systematic changes in the material properties.

Looking at figure 1.10, there is a slight trend in the data of increasing r_D with increasing magnesium content, but the change is not purely monotonic. Figure 1.11 shows the diffraction moduli versus magnesium content to determine whether the shift is due to a change in only one modulus but not the other. Looking particularly at the $E_{\langle 400 \rangle}$ and $E_{\langle 222 \rangle}$ subfigures, there does not appear to be a radical change in only one of the moduli. It is instead the ratio of the two that has a consistent change over the range of materials considered.

The total amount of change in r_D is approximately 8% over the range of compositions we have examined. To bring the finite element simulations from [4] into closest agreement with the AA-5182 experiments required a 40% increase in r_E.

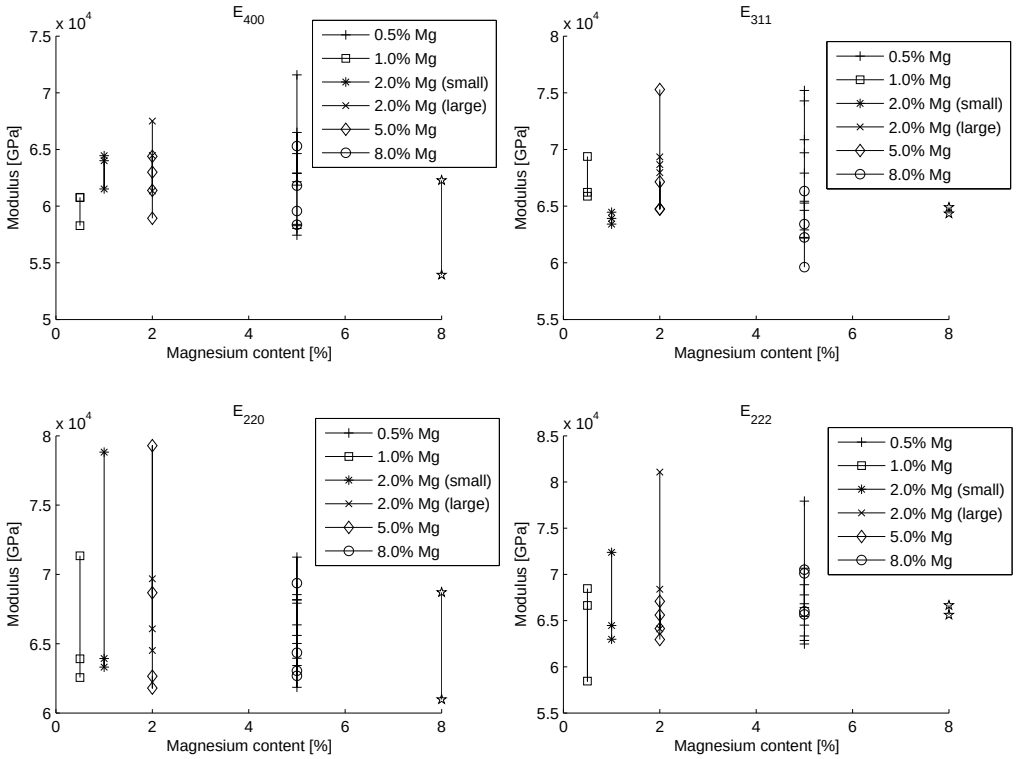

Figure 1.11: The directional moduli for each $\langle hkl \rangle$ and each unloading episode as a function of magnesium content.

It is unclear to what extent a percentage change in the single crystal quantity r_E will manifest itself in the hybrid polycrystal quantity r_D, so it is difficult to state definitively whether those numbers are in conflict. The conclusion is that the presence of magnesium in the aluminum alloy has a measurable effect on the single crystal elastic anisotropy. This change should be taken into account when initializing material properties during simulations.

1.6 Summary

Successfully modeling mechanical responses of polycrystalline materials requires an accurate knowledge of the mechanical properties of the single crystals in addition to sound averaging methods, among other factors. A previous study indicated that perhaps the single crystal elasticity parameters of pure materials cannot be automatically applied to their alloys. To determine the validity of such an assumption, we undertook a suite of *in situ* ND experiments on aluminum-magnesium alloys. An effective diffraction modulus was calculated in four crystallographic directions, and the ratio $E_{\langle 222\rangle}/E_{\langle 400\rangle}$ was examined as the measure of anisotropy. Over a range of compositions up to 8% Mg the change in the anisotropy was small yet measurable. This result does not preclude the presence of additional factors influencing the apparent anisotropy in finite element simulations of alloyed materials. Additionally, these experiments provide a set of data which can be used to initialize FE simulations and to which the results of those simulations can be compared.

CHAPTER 2

MODELING *IN SITU* NEUTRON DIFFRACTION EXPERIMENTS USING FINITE ELEMENT SIMULATIONS

The overarching principle behind this work is that data from both experiments and simulations can be greatly improved by comparison to each other. In this chapter the simulation frame work is presented in terms of both the theory behind the finite element simulations and the steps taken to model the experiments presented in the previous chapter. The method of determining r_D from the simulations is shown along with results for meshes with dodecahedral grains.

2.1 Polycrystal plasticity simulation framework

The simulations used in this study are performed using a parallel computational implementation of an elastoviscoplastic finite element formulation. The large scale parallel nature of the simulations gives the ability to have many degrees of freedom within each crystal in the bulk material while still following a volume large enough to accurately portray statistical trends. In this way it is possible to examine the essential focus of this study, the way strains and stresses develop in different grains.

When modeling polycrystalline material deformation there are several scales to consider, including most notably the scale of the bulk volume and the scale of the grains. In such models as we employ here the scale of dislocation motion is not considered; material deformation is assumed to take place through dislocation motion along slip planes, but the details are replaced by discrete slip modes. Properties and values quantifiable on the bulk scale include macroscopic specimen strain, macroscopic stress, and bulk elastic properties such as average Young's modulus and Poisson's ratio. Similar quantities are defined on the crystal scale, including lattice strains, anisotropic single crystal elastic moduli, crystal stresses,

and lattice orientation.

This section first presents the model equations and formulation used and then discusses instantiation of the specimens into the simulation framework using dodecahedral grains.

2.1.1 Mechanical response of virtual specimens

An elastoviscoplastic finite element formulation was used to simulate the response of the specimens to a loading history of uniaxial tension. This finite element formulation has the benefit of *a priori* satisfying compatibility everywhere like other displacement or velocity-based formulations through the use of continuous trial functions for the velocity. The equilibrium equations are satisfied in a weak sense. The deformation is assumed to be quasi-static; that is, the effects of momentum are small and can be neglected. The weak form of the equilibrium equations may be written as:

$$R_u = -\int_B \operatorname{tr}\left(\boldsymbol{\sigma}'^{\mathrm{T}} \operatorname{grad}\boldsymbol{\psi}\right) \mathrm{d}B + \int_B \pi \operatorname{div}\boldsymbol{\psi} \mathrm{d}B + \int_\Gamma \boldsymbol{t}\cdot\boldsymbol{\psi}\mathrm{d}\Gamma + \int_B \boldsymbol{\iota}\cdot\boldsymbol{\psi}\mathrm{d}B, \quad (2.1)$$

where R_u is the residual to be minimized, $\boldsymbol{\psi}$ are vector weighting functions, $\boldsymbol{t}$ is the traction vector, $\boldsymbol{\iota}$ is a body force per unit volume, B is the volume of the body, and Γ is its surface. The deviatoric Cauchy stress, $\boldsymbol{\sigma}'$, and mean stress (negative of the pressure, π) sum to the total Cauchy stress: $\boldsymbol{\sigma} = \boldsymbol{\sigma}' - \pi\mathbf{I}$, where $\mathbf{I}$ is the second order identity tensor. Traction or velocity is specified over the boundary.

The stress is replaced ultimately with the velocity field through introduction of the constitutive equations and the kinematic relation defining the velocity gradient. Equations for the elastic and plastic responses are required to model the regimes of behavior that exist in the tests. For the elastic behavior we use Hooke's Law for cubic symmetry. For the plastic behavior, we assume restricted slip along the close-packed planes and in the close-packed directions. The elastic and plastic behaviors

are combined through a kinematic decomposition of the total deformation gradient, $\mathbf{f}$, by the following three-part multiplicative decomposition:

$$\mathbf{f} = \mathbf{f}^{\flat}\mathbf{f}^{\star}\mathbf{f}^{\sharp} = \mathbf{v}^{\flat}\mathbf{r}^{\star}\mathbf{f}^{\sharp}. \tag{2.2}$$

Here $\mathbf{f}^{\sharp}$ is the purely plastic part of $\mathbf{f}$ arising from slip, $\mathbf{f}^{\star}$ is the lattice rotation which may be written as $\mathbf{r}^{\star}$, and $\mathbf{f}^{\flat}$ is the elastic part of $\mathbf{f}$. The deformation gradient $\mathbf{f}^{\sharp}$ can be used to define an intermediate configuration, $\hat{\mathcal{B}}$, which is a relaxed configuration obtained by unloading without rotation from the current configuration $\mathcal{B}$. Using this interpretation of $\hat{\mathcal{B}}$, the symmetric left elastic stretch tensor, $\mathbf{v}^{\flat}$, is introduced. For the case of small elastic strains ($\mathbf{e}^{\flat}$), $\mathbf{v}^{\flat} = \mathbf{I} + \mathbf{e}^{\flat}$, where $||\mathbf{e}^{\flat}|| << 1$.

The velocity gradient, $\mathbf{l}$ ($\equiv \frac{\partial \boldsymbol{u}}{\partial \boldsymbol{x}}$, where $\boldsymbol{u}$ is the velocity and $\boldsymbol{x}$ are the current coordinates), is obtained by differentiation of the deformation gradient with time and is split into the deformation rate tensor, $\mathbf{d} \equiv \mathrm{sym}(\mathbf{l})$, and the spin tensor, $\mathbf{w} \equiv \mathrm{skw}(\mathbf{l})$, expressed in the current configuration $\mathcal{B}$. These terms may be split further into spherical and deviatoric parts to give:

$$\mathrm{tr}(\mathbf{d}) = \mathrm{tr}(\dot{\mathbf{e}^{\flat}}), \quad \mathbf{d}' = \dot{\mathbf{e}^{\flat}}' + \hat{\mathbf{d}^{\sharp}}' + \mathbf{e}^{\flat\prime}\hat{\mathbf{w}}^{\sharp} - \hat{\mathbf{w}}^{\sharp}\mathbf{e}^{\flat\prime} \quad \text{and} \quad \mathbf{w} = \hat{\mathbf{w}}^{\sharp} + \mathbf{e}^{\flat\prime}\hat{\mathbf{d}^{\sharp}}' - \hat{\mathbf{d}^{\sharp}}'\mathbf{e}^{\flat\prime}, \tag{2.3}$$

where a prime ($\cdot'$) indicates the deviatoric component of a quantity and the $\hat{\cdot}$ superscript indicates mapping forward by $\mathbf{r}^{\star}$ according to:

$$\hat{\mathbf{w}}^{\sharp} = \mathbf{r}^{\star}\mathbf{w}^{\sharp}\mathbf{r}^{\star\mathrm{T}} \qquad \text{and} \qquad \hat{\mathbf{d}^{\sharp}}' = \mathbf{r}^{\star}\mathbf{d}^{\sharp\prime}\mathbf{r}^{\star\mathrm{T}} \tag{2.4}$$

to define the plastic deformation rate tensor, $\hat{\mathbf{d}^{\sharp}}'$, and the plastic spin tensor, $\hat{\mathbf{w}}^{\sharp}$, in the relaxed configuration $\hat{\mathcal{B}}$ (both $\mathbf{w}^{\sharp}$ and $\mathbf{d}^{\sharp\prime}$ are defined relative to $\mathbf{f}^{\sharp}$).

Equations for the elastic and plastic responses are introduced into the kinematic decomposition given by equation 2.3. The elastic response follows a linear relation:

$$\boldsymbol{\tau} = \mathbb{C}\mathbf{e}^{\flat} \qquad \text{with} \qquad \mathbb{C} = \mathbb{C}(\boldsymbol{r}), \tag{2.5}$$

where $\mathbb{C}$ is the tensor containing elastic moduli for cubic crystal symmetry, which depends on the orientation of the crystallographic lattice, $\boldsymbol{r}$. The Kirchhoff stress, $\boldsymbol{\tau}$, is related to the Cauchy stress, $\boldsymbol{\sigma}$, through $\boldsymbol{\tau} = \beta\boldsymbol{\sigma}$, where $\beta = \det(\mathbf{v}^\flat)$.

The viscoplastic flow rule is derived from the crystallographic slip and is defined as:

$$\hat{\mathbf{l}}^\sharp = \hat{\mathbf{d}}^{\sharp\prime} + \hat{\mathbf{w}}^\sharp = \dot{\mathbf{r}}^\star \mathbf{r}^{\star\mathrm{T}} + \sum_\alpha \dot{\gamma}^\alpha (\hat{\boldsymbol{T}}^\alpha), \tag{2.6}$$

where $\hat{\boldsymbol{T}}^\alpha$ is the Schmid tensor, $\hat{\boldsymbol{T}}^\alpha = \boldsymbol{b}^\alpha \otimes \boldsymbol{m}^\alpha$, and $\boldsymbol{b}^\alpha$ and $\boldsymbol{m}^\alpha$ are the slip direction and the slip plane normal for the α-slip system in configuration $\hat{\mathcal{B}}$. The assumed slip systems for the FCC crystals are the 12 systems with $\langle 110 \rangle$ directions and $\{111\}$ normals. Using these relations, the symmetric and skew symmetric parts of the plastic velocity gradient, $\hat{\mathbf{d}}^{\sharp\prime}$ and $\hat{\mathbf{w}}^\sharp$, respectively, are defined as:

$$\hat{\mathbf{d}}^{\sharp\prime} = \sum_\alpha \dot{\gamma}^\alpha \hat{\boldsymbol{P}}^\alpha \qquad \text{and} \qquad \hat{\mathbf{w}}^\sharp = \dot{\mathbf{r}}^\star \mathbf{r}^{\star\mathrm{T}} + \sum_\alpha \dot{\gamma}^\alpha \hat{\boldsymbol{Q}}^\alpha, \tag{2.7}$$

where

$$\hat{\boldsymbol{P}}^\alpha = \hat{\boldsymbol{P}}^\alpha(\boldsymbol{r}) = \mathrm{sym}\,(\hat{\boldsymbol{T}}^\alpha) \qquad \text{and} \qquad \hat{\boldsymbol{Q}}^\alpha = \hat{\boldsymbol{Q}}^\alpha(\boldsymbol{r}) = \mathrm{skw}\,(\hat{\boldsymbol{T}}^\alpha). \tag{2.8}$$

Using the symmetric portion of the Schmid tensor to define the stress active on the α-slip system , the plastic shearing rate, $\dot{\gamma}^\alpha$, is related to the resolved shear stress, τ^α, by a power law relation:

$$\dot{\gamma}^\alpha = \dot{\gamma}_0 \left(\frac{|\tau^\alpha|}{g^\alpha} \right)^{\frac{1}{m}} \mathrm{sgn}(\tau^\alpha) \qquad \text{with} \qquad \tau^\alpha = \mathrm{tr}(\hat{\boldsymbol{P}}^\alpha \boldsymbol{\tau}'), \tag{2.9}$$

where g^α is the slip system hardness, $\dot{\gamma}_0$ is a reference shear rate, and m is the rate sensitivity of slip. With the help of a time differencing of the elastic strain rate, the equations for the elastic and plastic responses are merged in the rate form of the kinematic decomposition and used to eliminate the stress in the equilibrium residual. The residual is cast in discretized form through the introduction of piecewise trial and weight functions to yield a matrix equation for the velocity field at the end of each time step.

To complete the solution methodology the lattice orientations, $\boldsymbol{r}$, and slip system strengths, g, must be advanced over time. The lattice orientation evolves as a consequence of the spin and is given by:

$$\dot{\boldsymbol{r}} = \frac{1}{2}\boldsymbol{\omega} + (\boldsymbol{\omega}\cdot\boldsymbol{r})\boldsymbol{r} + \boldsymbol{\omega}\times\boldsymbol{r} \qquad \text{where} \qquad \boldsymbol{\omega} = \text{vect}\left(\hat{\mathbf{w}}^{\sharp} - \sum_{\alpha}\dot{\gamma}^{\alpha}\hat{\boldsymbol{Q}}^{\alpha}\right). \quad (2.10)$$

Slip system strength (hardness) evolution is assumed to follow a Voce form, expressed as:

$$\dot{g} = h_0\left(\frac{g_s - g}{g_s - g_0}\right)^{n}\dot{\gamma} \qquad \text{where} \qquad \dot{\gamma} = \sum_{\alpha}|\dot{\gamma}^{\alpha}|. \quad (2.11)$$

The four material parameters in equation 2.11 are the initial slip system hardening rate, h_0, the saturation slip system strength, g_s, the initial slip system strength, g_0, and a hardening exponent, n. Each of these equations is numerically integrated in concert with the incremental solution for the motion. Determination of these parameters is presented in §2.2.

2.1.2 Instantiation of virtual specimens

Performing simulations using the FE code whose theory is detailed above requires a simulation domain. The domain comprises grains formed from finite elements. All elements in the mesh are 10-noded tetrahedra. The grains are formed by groups of neighboring elements sharing a common initial orientation. A complete grain is composed of 48 elements formed into the shape of a rhombic dodecahedron, though grains on the boundary of the domain may have fewer elements and their overall shape will differ from that of complete grains. The simulations presented in this chapter were all performed on the same mesh, which is shown in figure 2.1 with all of the boundary grains removed. The light box in the figure indicates the true extent of the domain but only the complete dodecahedral grains are shown. After the simulation begins the elements that began as part of a single grain are all able

to deform and reorient independently of each other. This can lead to variation in strain and stress and crystallographic misorientation within the grains. This mesh has 64,800 elements with over 800 interior grains (i.e. complete dodecahedra with 48 elements).

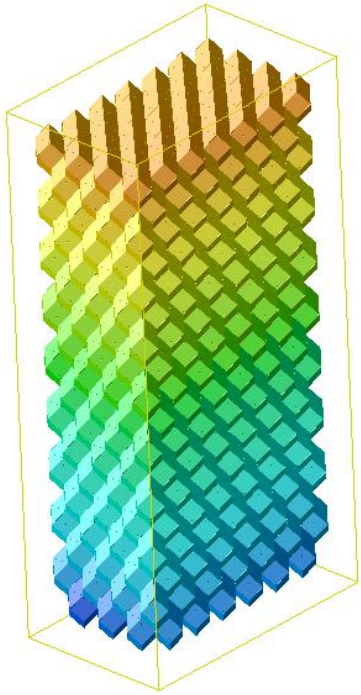

Figure 2.1: Interior grains in the finite element mesh. The grains are colored by z-coordinate to aid in visualization.

2.2 Initializing simulations to mimic experiments

The FE simulations must be matched to the experiments through the available inputs. These include the mesh of the domain itself, the boundary conditions applied to the mesh, the crystallographic orientations of the elements, and the material parameters, both elastic and plastic. We can then analyze the response of each simulation in terms of elastic moduli to observe whether a higher value

of r_E must be used to match experiments on different alloys. Therefore, as many variables as possible should be held constant between the various simulations. For each material simulated (various percentages of magnesium), there is a unique set of loads through which the mesh is deformed, an initial orientation distribution function (ODF), and a collection of material parameters that distinguish that material from the others. The plasticity parameters are unique for each material and the elasticity parameters are varied to give a predetermined set of values for r_E. The origin of each of the simulation inputs is described here.

2.2.1 Loading conditions

The boundary conditions are set to match the constant displacement rate of 4.23×10^{-3} mm/s (0.01 in/min) of the experiments on specimens with gage lengths of 50.8mm (2 in). Therefore, the approximate initial strain rate is $8.3 \times 10^{-5}\text{s}^{-1}$. For the FE mesh, the tension occurs in the z direction. Symmetry conditions are applied to the negative x, y, and z faces of the mesh to prevent rigid body motions. Free surface boundary conditions are applied to the positive x and y faces, which correspond to the lateral faces of the tension specimen. A constant displacement rate is applied to the positive z face to match the initial strain rate from the experiments.

The deformation history of every experiment followed the same protocol, as shown in figure 1.4. To recreate that deformation history, certain load setpoints are chosen for each material corresponding to the stress levels at which the unloading episodes initiated and at which the ND measurements were taken. Table 2.1 shows the nominal stress at which each unloading episode initiated for each material simulated.

Table 2.1: Nominal normal macroscopic stress (in MPa) at which each unloading episode initiated for the simulations.

Episode number	Al-2%Mg	Al-5%Mg	Al-8%Mg
1	94.0	137	167
2	111	173	198
3	116	200	219
4	125	208	225

2.2.2 Texture initialization

Bulk texture measurements of both the initial and final conditions were made on a triple-axis spectrometer for specimens of several of the materials [1]. Using these measurements we calculated the orientation distribution functions (ODFs) for those materials. For the simulations each grain must be initialized with a specific orientation. Though no attempt is made to exactly recreate, grain-by-grain, the orientations of the physical specimen, as a whole the orientational texture of the FE domain should match that of the physical domain. The current method of making that match is to create a list of thousands of orientations that, taken together, recreate the ODF. Initializing grain orientations sample randomly from that list. The ODF calculated from the mesh after such initialization is relatively close to that measured from the physical specimen. For the materials for which textures have been measured the initial texture is very close to uniform. Therefore, for the materials for which a measured texture is unavailable, we use a texture file that corresponds to a uniform ODF.

2.2.3 Material properties

The final type of input to consider is the material description. Both the elastic and plastic constitutive parameters must be specified for the simulations. Each material uses a unique set of parameters, some of which are determined solely from the experimental data and some of which vary as a parameter study. Since all the materials are cubic, there are three independent elastic moduli such as the single crystal elastic moduli commonly refered to as c_{11}, c_{12}, and c_{44} [21]. These also can be framed as an average Young's modulus, E; average Poisson's ratio, ν; and the elastic anisotropy, r_E [4]. For each of the different alloys modeled the value of Young's modulus is taken from monotonic tension tests (without diffraction) on an MTS machine. Three values of Poisson's ratio are used for each material: 0.25, 0.30, and 0.35. Finally, r_E is varied as a parameter taking the values 1.0, 1.2, and 1.7. For each material, therefore, nine sets of (c_{11}, c_{12}, c_{44}) are used corresponding to the invariant E and the three values each of ν and r_E.

The parameters associated with slip in equation 2.9 and equation 2.11 remain to be considered. Some of these parameters are held fixed for all simulations, namely $n = 1$, $m = 0.02$ and $\dot{\gamma}_0 = 1.0$, leaving the initial slip system hardening rate h_0, the initial slip system strength g_0, and the saturation slip system strength g_s yet to be determined. Using the same mesh used for all simulations, the slip parameters were varied for each material (that is, for each experimental macroscopic stress-strain curve and the loads and textures described above) until the macroscopic stress-strain curve from the simulation matched that from the experiment, as seen in figure 2.2. The value of r_E has very little effect on the macroscopic deformation since the values of E and ν remain constant.

Using a smaller mesh for material parameter determination would have saved a significant amount of computational time, since the parameters are found through

a "guess and check" method which requires a simulation be run until the top load of the final unloading episode is reached. However, when material properties were found using a smaller mesh and then those parameters were applied to the larger mesh, the macroscopic response changed. This is because a critical number of grains are needed in the mesh, and particularly through the cross section of tension, to have the result be independent of the particular choice for orientation of each element as long as the overall ODF is consistant. For example, in a smaller mesh there might be only on the order of 10 grains across the xy-plane, whereas the final mesh used had at least five times that many. With so few grains in the cross section, if one particular grain happens to be oriented with the most compliant direction aligned with tension, for example, it may have a disproportionate effect on its neighbors. The more elements through a cross section, the less significant each individual element orientation becomes to the overall response.

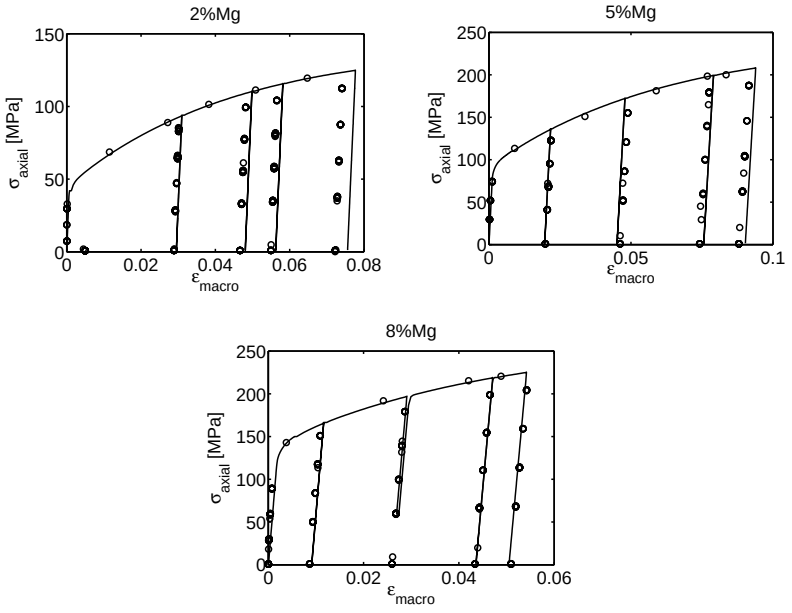

Figure 2.2: Macroscopic stress-strain curves showing the comparison between the experimental data and the simulations after the proper material parameters have been determined for each material.

Table 2.2: Viscoplastic material parameters used in FE simulations.

Material	h_0 [MPa]	g_0 [MPa]	g_s [MPa]
Al-2%Mg	350	21.5	72
Al-5%Mg	400	44	130
Al-8%Mg	425	67	137

2.3 Calculating r_D from simulation

The method of determining r_D is identical, whether working from experimental data or simulation results. In either case r_D comes from a ratio of slopes, each of which relates a change in macroscopic stress to a change in directional lattice strain. The method is illustrated for experimental data in §1.3.2. Finding r_D from the simulation results proceeds in much the same manner as from the experimental data. The first step is to find lattice strains at each stress level, measured in crystals satisfying equation 1.4. This is done by indicating those crystals which would contribute to a diffraction measurement, in the same way that the neutron beam and detector illuminate and count certain crystals in any given experimental configuration. For each element in the simulation, a misorientation angle, θ, is calculated between the $\{hkl\}$ plane normal, $\boldsymbol{c}$, and the scattering vector, $\boldsymbol{s}$:

$$\theta = \cos^{-1}\left(\mathbf{R}\boldsymbol{c} \cdot \boldsymbol{s}\right), \tag{2.12}$$

where $\mathbf{R}$ is the particular orientation of that element, expressed in matrix form. All elements that have a misorientation angle less than 5 degrees are considered contributory. An example showing elements that have been included in a particular measurement is given in figure 2.3 for a specific (hkl). A single data point on the macroscopic stress versus lattice strain plot is generated by taking the arithmetic mean of the normal lattice strains in the tension direction across all of the included

(a) Complete mesh with contributory elements highlighted.

(b) Only those elements which contribute to a diffraction measurement.

Figure 2.3: An illustration of elements that contribute to a single measurement during data reduction from a FE mesh. The elements shown are those that have a misorientation angle less than 5 degrees between their $\{100\}$ planes and the tension axis of the deformation.

elements:

$$\epsilon^{\text{sim}}_{\langle hkl\rangle} = \frac{1}{l}\sum_{i=1}^{l} \epsilon^{i}_{\langle hkl\rangle}, \tag{2.13}$$

where l is the number of contributory elements, $\epsilon^{i}_{\langle hkl\rangle}$ is $\epsilon_{\langle hkl\rangle}$ in the ith element, and $\epsilon^{\text{sim}}_{\langle hkl\rangle}$ is $\epsilon^{D}_{\langle hkl\rangle}$ as calculated for the simulation. This is similar to using the center of the Gaussian peak from the neutron diffraction data, as illustrated in figure 1.1. The stress level is found by taking the load (which is found by integrating the normal stress across all the surface elements that have an applied velocity) and dividing it by the initial cross-sectional area of the domain.

Exactly as for the ND data, the slope of a linear fit to the macroscopic stress versus lattice strain in each direction is defined as $E^{D}_{\langle hkl\rangle}$ in that direction. The ratio of $E^{D}_{\langle 111\rangle}$ to $E^{D}_{\langle 100\rangle}$ provides the value of r_D for that simulation.

The diffraction anisotropy is a hybrid quantity that includes information on both the macroscopic and lattice scales, as discussed in §1.3.2. This is because, while much information is available on the macroscopic scale, including the overall stress and strain through knowledge of the applied load and initial cross section

and through extensometer data, more limited information is available on the crystal scale. Lattice strains can be measured by means of diffraction, but the stresses cannot be measured directly in polycrystalline samples. A further complication arises in the neutron diffraction (ND) techniques employed here because the lattice strains are not measured in individual crystals but rather in groups of crystals sharing an axis of orientation, as described in §1.2. Since some information is lacking on the crystal scale or is known only as an average over a crystallographic fiber, it is necessary to invoke modeling assumptions to bridge the scales to the data that is available [22]. Previous efforts to bridge these scales include Voigt's isostrain (upper bound) [23], Reuss's isostress (lower bound) [24], and the work of Kroner [25], who utilized Eshelby's [26] self consistent model to find the polycrystal elastic constants based on the anisotropic single crystal elastic constants. Bollenrath *et al.* [27], Hayakawa *et al.* [28], De Wit [29], and Gnaupel-Herold *et al.* [30] have all extended Kroner's work to incorporate elastic moduli measurable through diffraction. These FE simulations provide another method of bridging the gap between the macroscopic and crystal lattice scales.

2.4 Simulation results

2.4.1 Texture

The pole figures from the experiments can be compared to the pole figures from the simulation results at the highest load. This is the load at which the most change in crystal orientation will be apparent. Since only a small amount of total strain was applied to each specimen, the amount of texture development was not significant. The patterns go from being disordered to those consistent with uniaxial tension, but the overall strength of the texture is weak, as shown in figure 2.4 and figure 2.5.

The simulation pole figures develop the same patterns as the simulation progresses, as demonstrated in figure 2.6 and figure 2.7. These results are not significantly affected by the particular choice of elasticity parameters. The patterns for the 200 pole figures appear to be slightly more accurate than those from the 220 pole figures, but in all cases the overall amount of texture development is small.

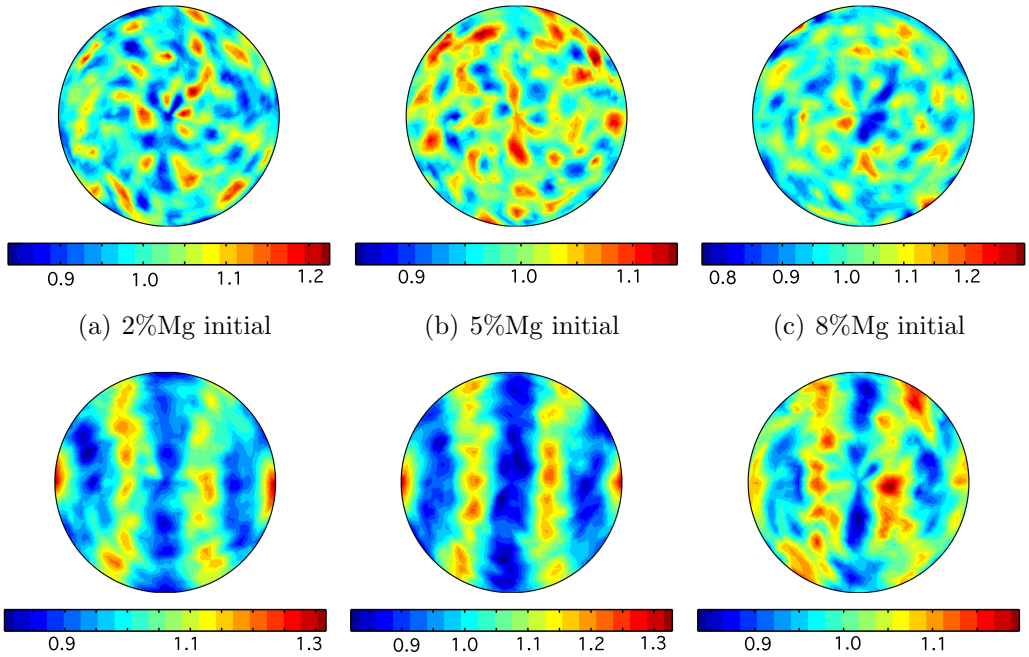

(a) 2%Mg initial (b) 5%Mg initial (c) 8%Mg initial

(d) 2%Mg final (e) 5%Mg final (f) 8%Mg final

Figure 2.4: 200 Pole figures both before (top row) and after (bottom row) deformation as measured in the experiments for three of the materials.

2.4.2 Elastic moduli

The elastic moduli have been calculated according to the methods outlined in §2.3 for each of the simulations. An example of the results is shown in figure 2.8 for the simulations of the 8%Mg material. Looking only at lattice strains in the axial direction, the value of ν does not significantly affect the strains. Therefore, in 2.8 results are shown for only one value of ν. Higher values of r_E change the moduli

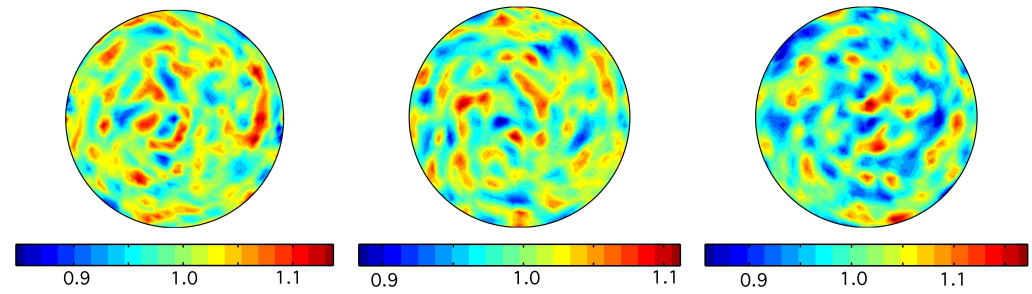

(a) 2%Mg initial (b) 5%Mg initial (c) 8%Mg initial

(d) 2%Mg final (e) 5%Mg final (f) 8%Mg final

Figure 2.5: 220 Pole figures both before (top row) and after (bottom row) deformation as measured in the experiments for three of the materials.

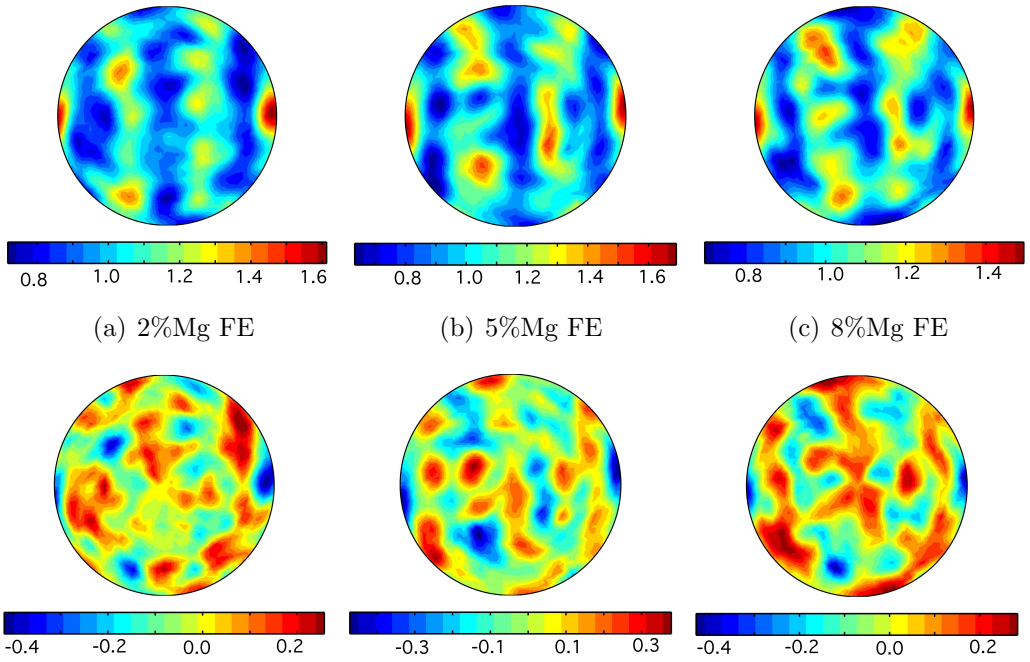

(a) 2%Mg FE (b) 5%Mg FE (c) 8%Mg FE

(d) 2%Mg difference (e) 5%Mg difference (f) 8%Mg difference

Figure 2.6: 200 Pole figures from the simulations (top row) and the difference between simulation and experiment (bottom row) for three of the materials.

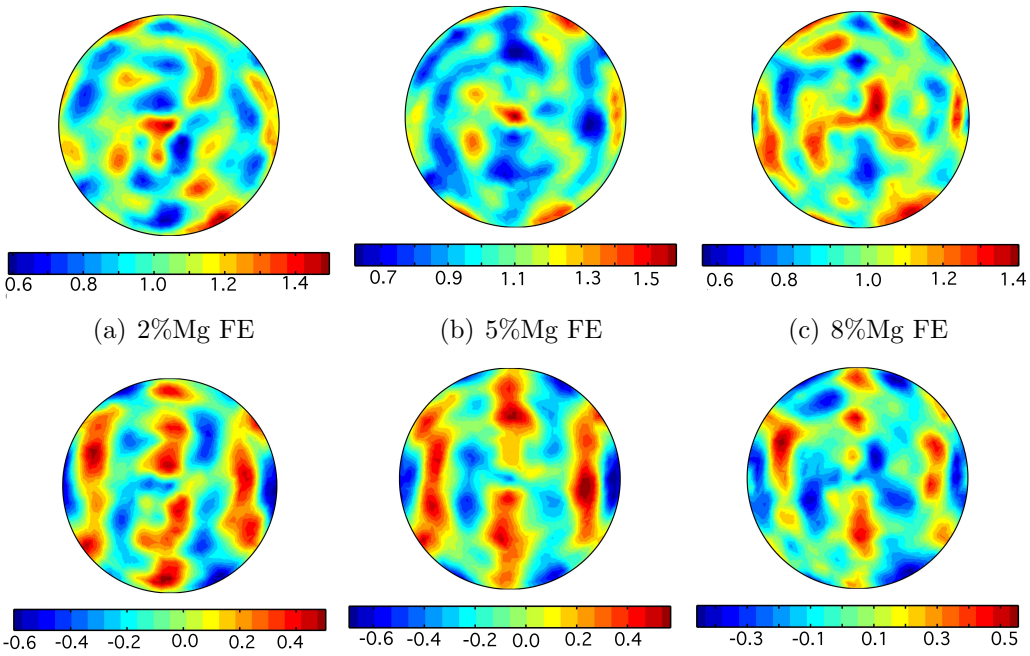

(a) 2%Mg FE (b) 5%Mg FE (c) 8%Mg FE

(d) 2%Mg difference (e) 5%Mg difference (f) 8%Mg difference

Figure 2.7: 220 Pole figures from the simulations (top row) and the difference between simulation and experiment (bottom row) for three of the materials.

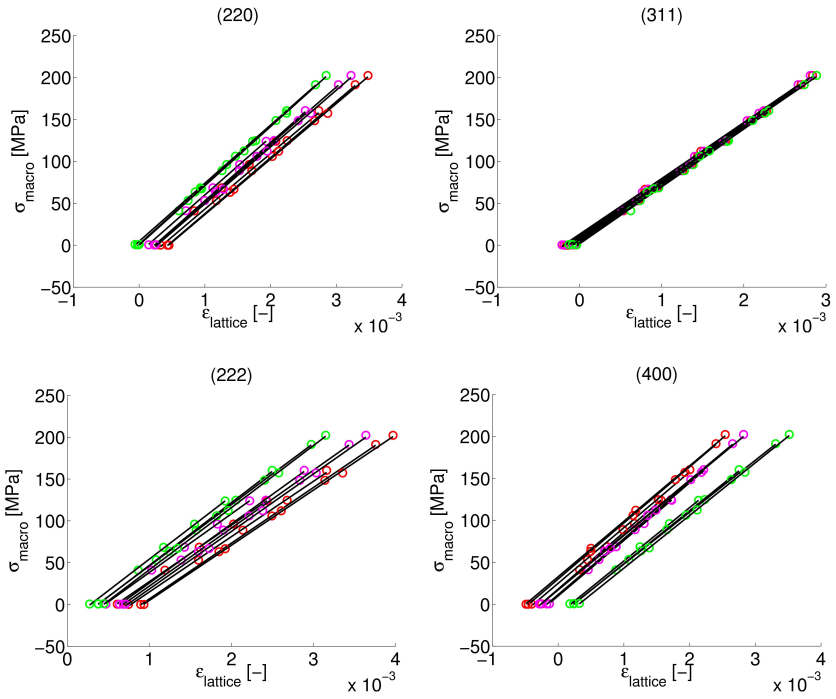

Figure 2.8: For the Al-8%Mg simulations, the data from which the directional moduli were calculated are shown. The colored data points represent the different values of r_E: red corresponds to r_E=1.0, magenta is r_E=1.2, and green is r_E=1.7. The solid lines are least squares curve fits to the data from individual unloading episodes.

in the different crystal directions, as expected. Using the slopes of the 400 and 222 data, the values of r_D can be found from each simulation. Figure 2.9 shows those results for all of the materials simulated and all values of r_E. For higher magnesium content a large value of r_E is needed in the simulation to generate an output value of r_D close to the experimental results, as expected. Notice that for

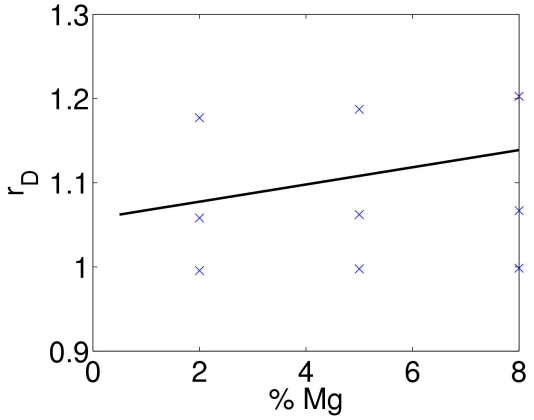

Figure 2.9: Diffraction anisotropy as a function of magnesium content. Results are shown for all values of r_E. The solid line in the figure is taken from figure 1.10 and is included for comparison.

an input value of r_E=1.0 (the bottom row of data points in the figure) the output value of r_D is also very close to 1.0. For higher values of r_E the value of r_D does not match the input value.

2.5 Summary

Using the elastoviscoplastic finite element formulation, the diffraction experiments presented in chapter 1 have been modeled and the results compared according to both crystallographic texture and elastic moduli. The textures, while weak in both experiments and simulations, have shown general agreement in form and scale. The diffraction moduli have been calculated for several input values of r_E.

CHAPTER 3

SENSITIVITY OF THE SIMULATED CRYSTAL STRESS DISTRIBUTION TO GRAIN DISCRETIZATION

3.1 Introduction

Having introduced the modeling framework and presented the results of simulations using one particular mesh and various material parameters, the influence of varying an additional aspect of the simulations is now addressed. For polycrystals, the rendering of an aggregate can be an important contribution towards the total simulation result. Variables available for creating the aggregate domain in a finite element simulation include the type of elements, the shape of the domain, the number of degrees of freedom within each crystal, the morphology (shape) of the crystals, and the topology associated with their arrangement. These simple variables can have an important impact on bulk behaviour. For example, Bunge, *et al.* [31] explored the effects of grain shape and packing on the elastic properties of polycrystals, using grains of three different shapes to do so. They found that the influence of these factors can be up to 25% of the total texture influence. This chapter explores the influence of these geometric properties of the grains on the fidelity of the simulation results, particularly the stresses within crystals.

For polycrystals, grain interactions occur via intergranular tractions. These intergranular tractions are the local boundary conditions for grains and thus control the stress internal to the grains. The stress observed at the macroscopic scale may be computed from averaging over an external surface of an aggregate. To fully assess a model it is necessary to compare model results to experimental results not only through this aggregate average, but also through the distribution of crystal stresses within the aggregate, assuming that a goal of the model is to illuminate

how crystals act collectively. Since the created domain can never be completely naturalistic it is possible that some aspect of the virtual samples may introduce an aphysical artifact. By insisting on assessment of the accuracy at the crystal level as well as for the aggregate average to determine that any artifacts are at an acceptably small level, it is necessary to have measurements of the response at the scale of crystals as a basis for comparison. Diffraction measurements with *in situ* mechanical loading provide that experimental basis for comparison.

Knowing the extent to which the grain and bulk instantiation (i.e. formation of the FE representation of the physical specimen) influence the simulation results in terms of not only elastic anisotropy, but also stress distributions throughout the aggregate (both within each crystal and across the entire domain) may shed further light on the discrepancy between simulated and physical manifestations of diffraction anisotropy. Additionally, it is necessary to understand the influence of specimen instantiation before the simulations can be used with confidence in either of two predictive capacities: predicting aggregate behaviors from those of single crystals; and inferring single crystal properties from aggregate averages.

Stress Distributions

Elastic anisotropy has already been discussed at length in previous chapters. A second aspect of the mechanical response of polycrystals that relates to the interaction of grains under load is the variability of stress within and among the crystals constituting the bulk. The mutual constraints that grains place on each other are affected by a variety of factors, including the degree of mechanical anisotropy, the strength of the crystallographic texture, and the geometry of the grains. Thus, the manner in which grains are discretized in a simulation plays a role in the degree of variability in the computed stresses. While isolated grains of the same orientation

and shape would exhibit identical responses according to the model, stress variation can stem from the influence of abutting grains. Each unique neighborhood of grains can lead to unique constraints. Locally, stress may be elevated over volumes that experience a strong influence of the constraints. The domains where stress concentrations arise are of interest in assessing where plastic flow initiates and in predicting the location of failure sites.

Published literature on this topic reports that variability in the stress exists during loading and following unloading. The most direct evidence is available from X-ray diffraction methods that permit interrogation of individual grains under *in situ* loading, such as the experiments presented in [32]. The standard deviation of the axial component of the lattice strain in copper under tensile loading was examined for twenty crystals sharing the same Bragg condition. The standard deviations of the strain were computed from the peak shifts with changes in load and were on the order of 6% of the average values.

The difficulty in experimentally quantifying the spatial distribution of stress over a polycrystal motivates the use of simulation to assist in this task and places a high expectation on the quantitative accuracy of numerical estimates. Again, the sensitivity of the computed responses to the grain discretization is potentially an issue. Intra- and inter-grain variabilities are expected to depend on discretization owing to the differences in the numbers of neighbors with various discretizations and to the manner in which particular grain geometries can be divided by tetrahedral elements.

3.2 Instantiating the virtual specimens

When dividing the FE domain into grains there are many choices including both regular tessellations using one shape congruently repeated throughout space and

irregular tessellations using multiple (and not necessarily congruent) shapes to fill space. Using irregular tessellations it may be possible to generate a less idealized and more realistic array of grain shapes, but there are drawbacks. It often takes many more elements to represent a smaller number of grains. Also, since we wish to observe the influence of grain shape and organization on crystal stress distributions we prefer to use only regular tessellations which have more easily quantifiable and homogeneous attributes throughout the mesh. There are a limited number of parallelohedra (polyhedra that fill space via parallel translations) in $\mathbb{R}^3$ [33]. These are cubes, hexagonal prisms, truncated octahedra, hexarhombic dodecahedra, and rhombic dodecahedra. We chose cubes, truncated octahedra, and rhombic dodecahedra, following the choices in [31], and created FE meshes of a unit cube with grains in each of those shapes. In all cases the elements are 10-noded tetrahedra and grains are formed by sharing a common initial crystal orientation between groups of these elements arranged in the correct shapes. The tetrahedral elements are preferable over hexahedral (or "brick") elements since it is easier to form relatively smooth crystal shapes from multiple tetrahedra than from bricks. Figure 3.1 shows a small number of grains from each of the meshes used, and figure 3.2 shows the complete mesh of octahedral grains, both with and without the boundary grains, which demonstrates that incomplete grains are present at the boundaries of the mesh to build a smooth unit cube volume. A cubic domain gives the greatest volume-to-surface-area ratio, which in turn allows more of the crystals composing the aggregate to be fully formed interior crystals rather than being on the surface and possibly comprising fewer finite elements.

When a complete mesh is composed from each of the grain shapes, a unique packing structure results. If you consider the centroid of each grain to be a lattice point and compose unit cells based on the locations of these lattice points, cubic

grains create unit cells equivalent to a simple cubic (SC) pattern. Similarly, dodecahedral grains lie on lattice points whose unit cell is equivalent to a face-centered cubic (FCC) lattice, and the octahedral grains form a body-centered cubic (BCC) unit cell. These patterns are illustrated in figure 3.1. Table 3.1 shows some interesting and relevant properties of the different grains. The attributes assumed to be of most importance are the number of nearest neighbors and the number of degrees of freedom per grain [34].

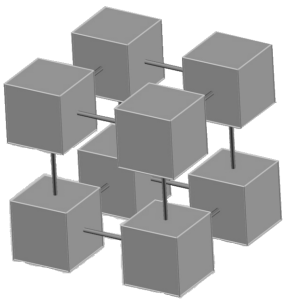

(a) Cubic grains. (24 elements, SC structure)

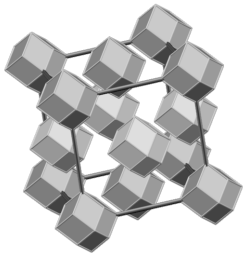

(b) Dodecahedral grains. (48 elements, FCC structure)

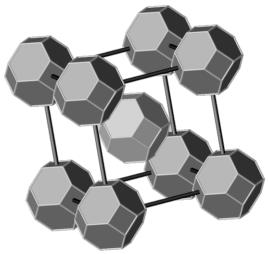

(c) Truncated octahedral grains. (72 elements, BCC structure)

Figure 3.1: A small cluster of grains (showing the packing type) for each of the three grain discretizations used in the FE simulations. The distance between the centroids of the grains has been increased to emphasize the grain shape and packing structure; the actual meshes are space-filling.

Table 3.1: Geometric properties of different grain shapes and the meshes composed from them. The "surface area per unit volume" measurement assumes each grain has volume $1[L^3]$ and the measurement itself is in units of $[L]$.

Grain Shape	Cube	Rhombic Dodecahedron	Truncated Octahedron
Packing Structure	SC	FCC	BCC
Vertices	8	14	24
Edges	12	24	36
Faces (Nearest neighbors)	6	12	14
Surface area per unit volume	6.00	5.35	5.31
Elements per grain	24	48	72
Degrees of freedom per grain	195	303	550
Grains in mesh	3375	2360	1241
Elements in mesh	81000	81000	73728

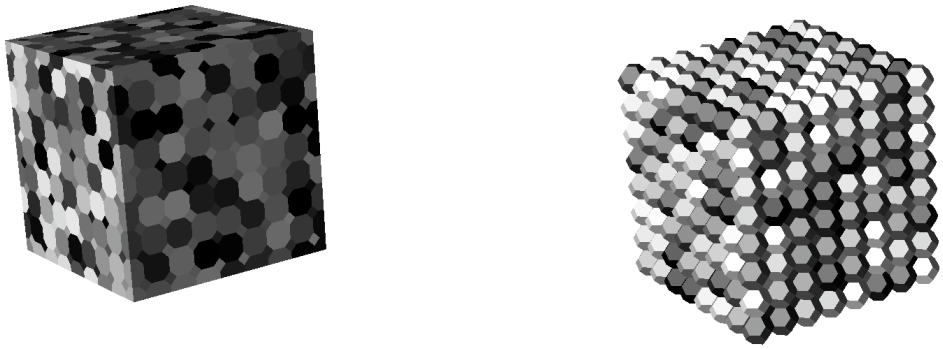

(a) Complete mesh, filling a unit cube of volume exactly.

(b) Only the grains which have 72 elements, forming complete octahedra. All partial grains have been stripped away from the boundary.

Figure 3.2: Mesh composed of octahedral grains. All elements forming a single grain are given the same random shading to aid in visualizing the grains.

3.3 Initializing simulations to mimic experiments

Comparing the simulation results for different meshes must be done with as many other simulation variables as possible held constant. The Al-Mg experiments are used to initialize the simulations and for reference when examining r_D for each mesh. Results in terms of stress distributions are compared to the results in [32] for reference. The experiments in that paper consist of measurement of {440} reflections in 20 individual grains in a bulk copper polycrystal measured with high energy XRD. These simulations are not explicitly based on those experiments but the stress distributions found here are compared to those from [32].

The goal is to uncover any grain discretization dependent effects on the elastic anisotropy and lattice strain (and therefore stress) variability of the FE simulations. Therefore, as many variables as possible must be held constant between the various simulations. Necessary inputs include: (i) meshes, (ii) boundary conditions and deformation histories, (iii) initial textures, and (iv) material parameters.

Much of this initialization proceeds exactly as described in §2.2. The boundary conditions are identical on all meshes and generate the same initial strain rate of $8.3 \times 10^{-5}\text{s}^{-1}$. The deformation history is generated by the list of load setpoints which are particular to each material and match the macroscopic stresses at which ND measurements were taken and unloading episodes initialized. The textures are initialized as described in §2.2.2 with each grain (composed of neighboring elements in the particular shape for that mesh, sharing the same initial orientation) taking a random orientation from a list of several thousand which together generate the ODF from experiment (or a uniform ODF).

The same sets of elastic parameters are used for all simulations. The value of Young's modulus is 66.5 GPa for all simulations, which is an average of the values measured from the macroscopic stress-strain curves for each material. The value of Poisson's ratio is kept constant at 0.35. Finally, r_E is varied as a parameter taking the values 1.0, 1.2, and 1.7. For each material, therefore, three sets of (c_{11}, c_{12}, c_{44}) are used corresponding to the invariant E and ν and the three values of r_E, as shown in table 3.2. It is interesting to note that to effect a change on the order of 50% in the single crystal anisotropy it is only necessary to change the individual elastic constants between approximately 8% and 30%.

The plasticity parameters as found by curve fitting using the dodecahedral mesh (figure 3.3(a)) were used for the simulations on all three meshes, as shown in figure 3.3(b) for one of the materials, which demonstrates the effect of sharing constitutive parameters across meshes. Note that the grain shape appears to affect the hardening rate slightly, which can increase the stress at a given strain. Since the unloading episodes are triggered by a macroscopic stress and not a plastic strain, differences in the ordinate are more significant than differences in the abscissa in figure 3.3(b). Using the same slip parameters for the different grain shapes

Table 3.2: Elastic material parameters used in FE simulations. All moduli are given in GPa.

r_E	c_{11}	c_{12}	c_{44}
1.0	106.7	57.4	49.2
1.2	103.4	59.1	54.2
1.7	97.3	62.1	63.3

Table 3.3: Viscoplastic material parameters used in FE simulations. The values $n = 1$, $m = 0.02$ and $\dot{\gamma}_0 = 1.0$ are invariant over all simulations.

Material	h_0 [MPa]	g_0 [MPa]	g_s [MPa]
Al-1%Mg	340	17	51
Al-2%Mg	350	21.5	72
Al-5%Mg	400	44	130
Al-8%Mg	425	67	137

appears to be a valid choice. The final choices for material parameters are shown in table 3.3.

A total of 36 simulations have been performed and analysed here: each of three sets of elasticity parameters with each of four sets of plasticity parameters on each of three meshes.

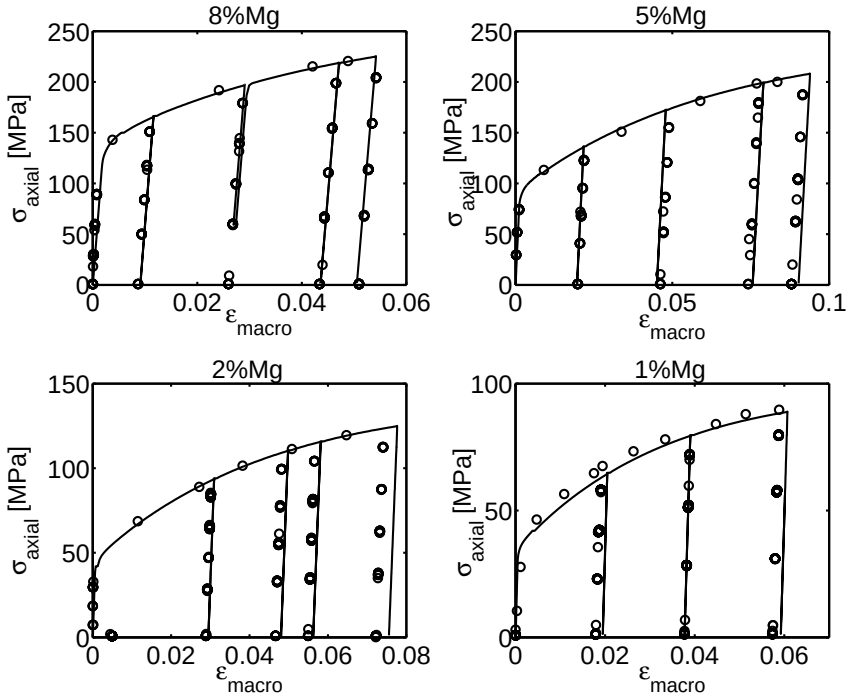

(a) All materials simulated with dodecahedral grains. The solid lines are the simulation results and the marks indicate experimentally measured data.

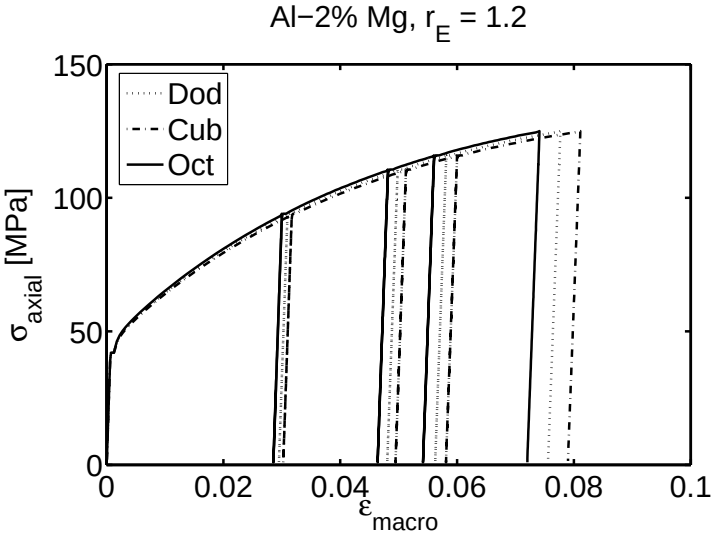

(b) Results from the three mesh types for a single common set of both elastic and plastic constitutive parameters.

Figure 3.3: Macroscopic stress-strain curves showing the comparison between the experimental data and the three different grain-type meshes.

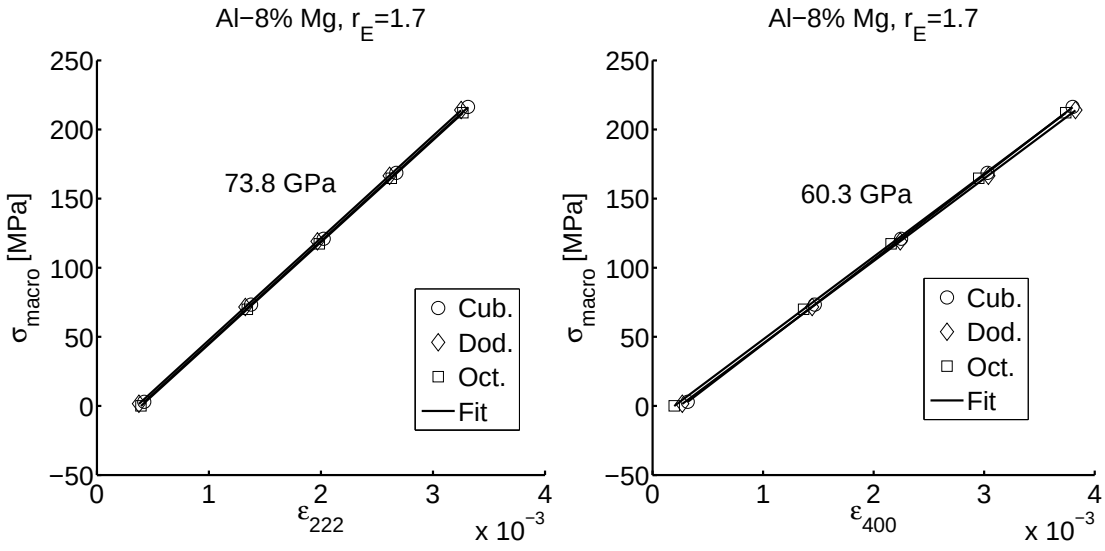

Figure 3.4: For the simulations of Al-8%Mg with r_E=1.7, the macroscopic axial stress is shown versus the lattice strains. The slope of each line, averaged over the three grain shapes, is shown in each figure.

3.4 Results of grain discretization study

3.4.1 Diffraction moduli

Following the scheme detailed in §2.3, values of r_D are determined from each simulation. A typical example of the plots from which $E^D_{\langle 222\rangle}$ and $E^D_{\langle 400\rangle}$ are calculated is shown in figure 3.4. Any difference in diffraction moduli between the simulations with different grain shapes appears negligible. This means that the diffraction anisotropy appears relatively insensitive to the grain discretizations used here.

In the experiments there is a slight trend of increasing r_D with increasing magnesium content. Using FE simulations, we introduce a method of relating the measureable r_D back to the actual material property r_E. The resulting value of r_D from specified r_E is shown in figure 3.5 for two sets of plasticity parameters. Slight variations appear between different grain shapes, but figure 3.4 has demonstrated

that those variations are small and not systematic. The significance of this plot is the amount of damping seen between r_E and r_D. A single crystal value of r_E=1 results in apparent isotropy in the diffraction moduli, as expected. If the single crystal properties are isotropic, the particular arrangement of grains should not influence the resulting lattice strains since all directions should be equivalent. As the single crystal anisotropy increases, so too does the diffraction anisotropy. Over the range of r_E studied here, the FE simulations predict an approximate relationship between r_D and r_E as $(\partial r_D/\partial r_E) \approx 0.3$. Averaging over groups of crystals, each of which experiences unique conditions from its neighbors, reduces the apparent elastic anisotropy by up to 30% from the true single crystal property.

It is important to ask whether changes in other material parameters can impact r_D as well. Relationships between r_D and the three slip system parameters that varied between simulations of different materials (h_0, g_0, and g_s) are shown in figure 3.6. Clearly the values of these slip system parameters do not affect r_D. Given the material deformation model in use here, the only material parameter that has a significant impact on r_D is r_E.

3.4.2 Stress distributions

Two main types of stress distributions are considered: intergranular (among grains) and intragranular (within grains). Intergranular stress variation is calculated by finding the *average value* of σ_{zz} over all elements within each grain at any given load level during a simulation, then calculating the standard deviation of those averages throughout the mesh. Intragranular stress variation is calculated by finding the *standard deviation* of σ_{zz} within each grain and averaging those standard deviations over all grains in a mesh. The intergranular stress may be thought of as the variation of stress from one grain to another whereas the intragranular stress may

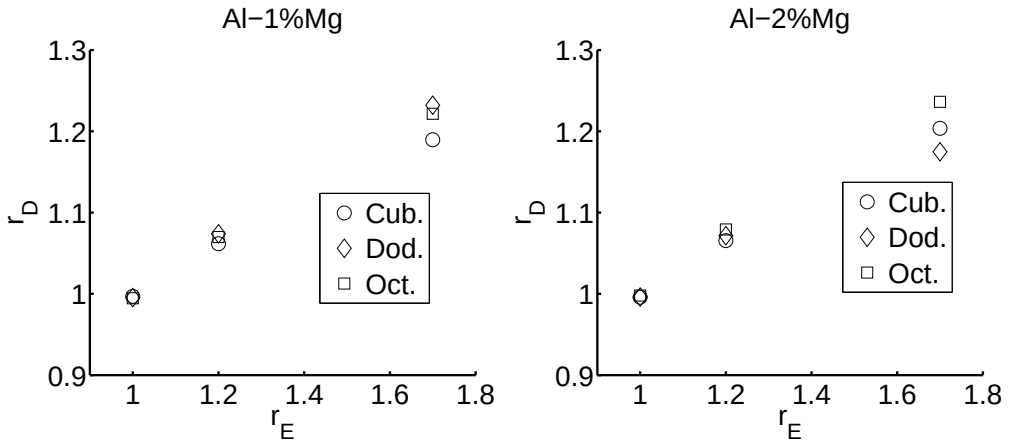

Figure 3.5: For the simulations of particular materials, r_D is shown versus the input value of r_E for each grain discretization.

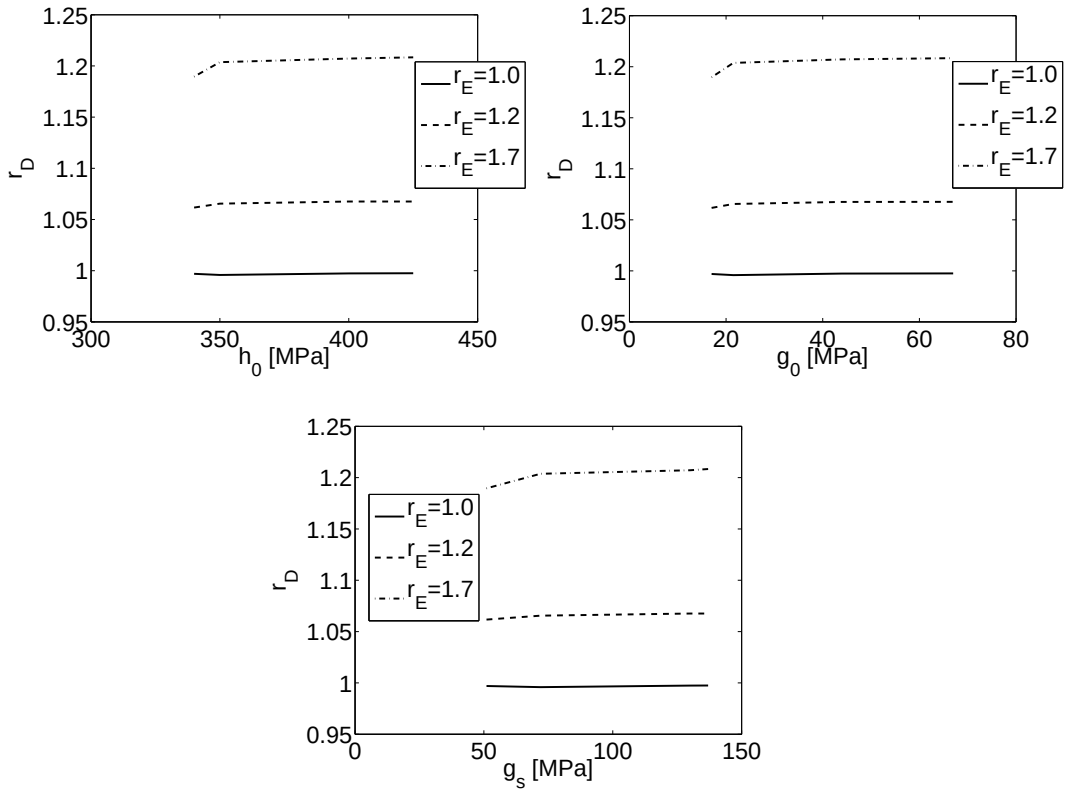

Figure 3.6: For the simulations with cubic grains, r_D is shown versus the input value of various material parameters.

be thought of as the amount of variability of stress within each grain.

Standard deviations of the axial component of intergranular stresses are shown in figure 3.7 for one material. Comparable trends are seen in each material modeled. The top and bottom of the last unloading episode are used to generate the data shown. The most variation is seen in the simulations with cubic grains, the least in the octahedral grains. As discussed in §3.1, typical values found in experiments for variation of strain between different grains satisfying the same diffraction condition are approximately 6% of the average value. It is difficult to make an analogous calculation here since elements that begin the simulation sharing an identical orientation do not always maintain that close orientational relationship through the deformation. In the simulations, a diffraction condition is satisfied (or not) by elements, not by grains, as seen in figure 2.3(b). Here, we consider all grains in the mesh and see variation in stress of approximately 12%. This higher value is not surprising since portions of the material with different orientations should be expected to experience different stresses.

The trends of intragranular variations are shown in figure 3.8, and they are opposite to those of intergranular stresses in terms of grain shape dependence: cubic grains show the least variation and octahedral grains the most. The larger number of neighbors experienced by the octahedral grains may generate a greater variety of boundary conditions on a single grain than in the cubic grains. This explains both the larger variation of stress within each grain and the smaller variation of stress between grains for the octahedral shape. If each grain is allowed to conform to the neighboring crystals on each side, though the variation within a grain may be relatively large, each grain in the mesh will experience that condition; in effect each grain is becoming more like the whole, which can act to diminish differences between different grains. In the cubic grains (with only six neighbors) each grain

can act more independently and is less likely to be experiencing a neighborhood similar to other grains, thereby emphasizing differences between grains. One aspect of the differences in grain discretizations whose influence cannot be ruled out is the greater number of elements comprising the octahedral grains. Due to their differences in shape it is difficult to mesh each type of grain with identical numbers of elements, and thus to remove this unwanted degree of freedom, while still generating as many grains as possible within each mesh. The larger number of degrees of freedom within the octahedral grains may enhance the effects of having more neighbors.

Looking at the magnitudes of the standard deviations in figures 3.7 and 3.8, it is at first somewhat surprising that the amount of stress variation within grains is equal to or greater than the stress variation between different grains. This is most likely due to the averaging of stress within grains that takes place for the intergranular stress calculation. The standard deviation of stress over all elements in the mesh, with no averaging within grains, is shown in figure 3.9 for the same conditions as figures 3.7 and 3.8. There the magnitude is greatest of all, as expected.

In both the intergranular and intragranular stress variations there is a common trend wherein the standard deviations are independent of r_E in the loaded state but highly dependent on r_E in the unloaded state. The stress state is constrained by the plasticity model to lie on the flow surface during plastic flow. Recall that while modeling deformation of each material, the plasticity parameters do not change while r_E does. Therefore, the flow surface is relatively independent of the elasticity parameters. Similar, but not identical, stress states are reached once the material yields and begins to flow. This produces comparable values of standard deviation of the stress distribution. In contrast, unloading from the plastic regime

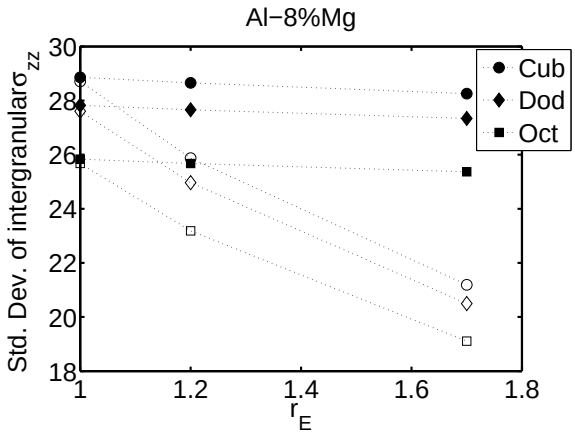

Figure 3.7: Trends in stress among grains (intergranular) are shown for both loaded (solid markers) and unloaded (empty markers) configurations. For each grain an average stress value is computed, and the standard deviation between those granular averages is shown in units of MPa. The macroscopic stress level in the loaded state is ∼200MPa.

is essentially an elastic event, and changes in stress with unloading are directly dependent on the elastic moduli. Interestingly, the stress changes occurring under higher elastic anisotropy produce a more uniform stress state (lower values of the standard deviation of stresses) than if the elasticity is more isotropic. As can be seen, for the elastically isotropic case of r_E=1.0 there is very little difference between the loaded and unloaded states. This is expected since as the loads are removed all crystals will tend to relax and unload to the same degree, which would give no source for changing the relative stress levels that were established under load. For FCC crystals with $r_E >$ 1.0, the crystallographic dependence of the strength and elasticity both show an increase from the 100 to the 111 directions, which may allow crystals with high stress to more readily relax upon unloading, bringing their stress values closer to those of the the less highly stressed (and less compliantly oriented) crystals.

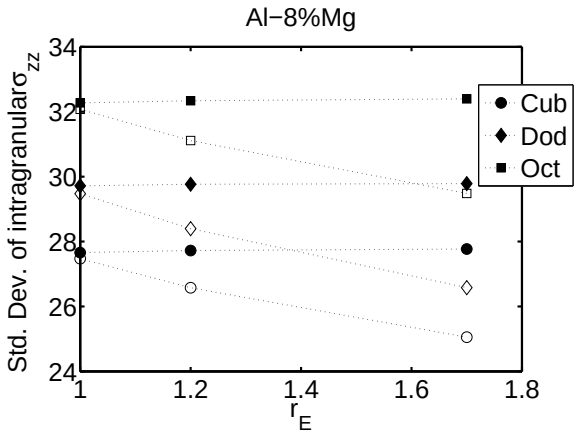

Figure 3.8: The average standard deviation of the axial component of stress within grains (intragranular) is shown for both loaded (solid markers) and unloaded (empty markers) configurations in units of MPa. The macroscopic stress level in the loaded state is ∼200MPa.

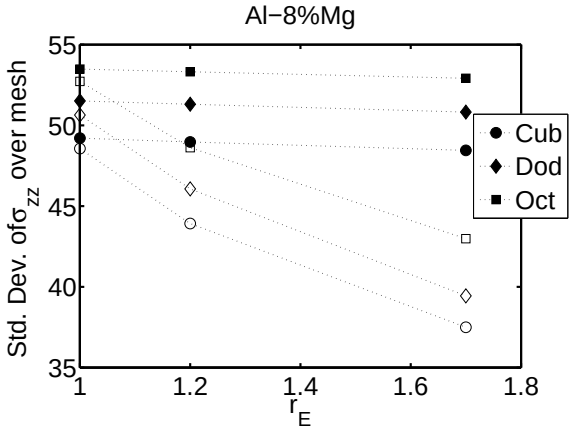

Figure 3.9: The standard deviation of the axial component of stress over all elements in the mesh is shown for both loaded (solid markers) and unloaded (empty markers) configurations in units of MPa. The macroscopic stress level in the loaded state is ∼200MPa.

3.5 Conclusions of grain discretization study

Deformation and *in situ* ND of several aluminum alloys has been modeled using elastoviscoplastic FE simulations with meshes formed from grains of different shapes and packing arrangements. The diffraction anisotropy calculated from the simulation results has been compared across meshes and materials. By changing the individual single crystal elastic moduli by less than 30%, the single crystal anisotropy has been changed by over 50%. In doing so, the simulations show a relationship between r_D and r_E of $(\partial r_D/\partial r_E) \approx 0.3$ independent of the grain discretization.

Intergranular and intragranular stress variations are found to depend consistently on the grain shape, with octahedral grains showing the most intragranular and least intergranular variation, and vise versa for cubic grains. The amount of stress variation for all meshes is reasonably consistent with values found in experiments. For all grain shapes, stress variation is maximal at higher loads and decreases upon unloading. Larger elastic anisotropy causes a larger drop in stress variation with unloading.

When deciding which grain discretization to utilize in finite element simulations it is necessary to weigh the relative benefits of different options. Cubic grains, as realized in this study, have fewer degrees of freedom, sharper corners, and fewer neighbors than octahedral grains. This allows a greater number of crystals to be modeled with a given allotment of computing resources. If the main interest of the project is something for which a greater number of grains would be a major benefit (for example, texture evolution) this may be a good choice. If, however, capturing trends in stress development and variation is more important, the additional degrees of freedom and more realistic neighborhoods of the octahedral grains may be a better choice.

CHAPTER 4

USING THE SINGLE CRYSTAL YIELD SURFACE TO ESTIMATE STRESS IN FCC POLYCRYSTALS

4.1 Introduction

Diffraction experiments on polycrystalline samples typically generate data pertaining to lattice strains in groups of crystals sharing particular orientations. If those data can be coupled with stress information it is common to consider the elastic moduli of the polycrystal. Unfortunately, moduli depend on local measurements of both strain and stress, but stress cannot be measured on a local basis and strain is not generally measured in each individual grain during diffraction of bulk specimens, but rather in groups of grains. It is therefore necessary to make assumptions about both the stress and strain to reach any conclusions about moduli in polycrystalline samples. The stress in each crystal is generally assumed to be equal to the macroscopic stress of the bulk polycrystal. The lattice strains as measured are assumed to be equal in all crystals contributing to the diffraction measurement (which are in turn assumed to have identical orientation), when in fact each measurement is due to many crystals with different orientations and possibly a wide range of strain states. If either the assumptions pertaining to stress or strain can be improved upon, the resulting consideration of elastic moduli may be much enhanced. A further assumption generally made is that the stress in each crystal is unaffected by whether or not a significant amount of plastic deformation has taken place. In fact, after a sufficient amount of deformation has taken place, crystal stresses will surpass the initial yield strength of the material and will lie on the single crystal yield surface, eventually tending towards a vertex in that yield surface which can accommodate the deformation taking place within

the crystal, as discussed in §4.2.2. Using knowledge of the yield surface along with finite element simulations of *in situ* diffraction measurements of uniaxial loading on polycrystalline specimens provides improved estimates of crystal stresses in the bulk.

In using simulations to analyze the type of data that may be obtained during *in situ* mechanical loading of polycrystalline bulk materials with neutron or x-ray diffraction, it is necessary to treat the data as if it has come from such experiments. Diffraction measurements of lattice strains take place over groups of crystals on a common crystallographic fiber. Crystallographic fibers are groups of crystals that have identical orientations, save a rotation about a single axis [35]. Typically, a fiber will be described by an axis in the crystal framework being parallel to one in the sample framework. This is the group of grains that contributes to a measurement during a diffraction experiment, as discussed in §4.4.2. For much of this study analysis takes place by finite elements grouped along fibers, thereby mimicking the *in situ* diffraction experiments. The macroscopic stress state, the yield surface vertices, and the lattice stresses on the finite elements are all considered to determine the most accurate and practical estimates of stresses to use in determining moduli from experiments.

This chapter begins with a discussion of single crystals, particularly the conventions for performing calculations with stress, and the relevant aspects of the single crystal yield surface. It then goes on to discuss the important aspects of combining single crystals into a polycrystal aggregate, including crystal orientations, crystallographic fibers, and various methods of data analysis from a polycrystal. The methodology used in this study follows, including the finite element (FE) simulations and the methods of data reduction from them. An overview of the data obtained from the FE simulations is included, followed by the results presented

in terms of lattice strains, stresses along crystallographic fibers, and diffraction moduli, and concluding with an in depth discussion of those results, focussing on the impact that the yield surface has on elastic anisotropy.

4.2 Single crystal relations

When examining the behavior of polycrystal aggregates the first step is to understand the relevant properties and behaviors of the single crystals that compose those aggregates. This section begins with a presentation of the conventions used to describe and compare stresses, provides a brief overview of the kinematics and elasticity formulation used, and then discusses the single crystal yield surface.

4.2.1 Representing stress

All stress states considered are 3-dimensional Cauchy stress tensors, $\boldsymbol{\sigma}$. As will be discussed further in §4.2.2 below, the deviatoric portion of the stress, $\boldsymbol{\sigma}'$, is often of interest, and can be calculated as:

$$\boldsymbol{\sigma}' = \boldsymbol{\sigma} + \pi \mathbf{I}, \tag{4.1}$$

where $\pi \equiv -\frac{1}{3}\mathrm{tr}\,\boldsymbol{\sigma}$ is the pressure and $\mathbf{I}$ is the identity tensor. It is often convenient to work with the stresses as vectors instead of matrices, mainly for ease of performing many calculations simultaneously during the data reduction process. The full stress matrix is reduced to its deviatoric vector form, σ, as per the following

convention:

$$\boldsymbol{\sigma} = \begin{bmatrix} \sigma_{xx} & \sigma_{xy} & \sigma_{xz} \\ \sigma_{xy} & \sigma_{yy} & \sigma_{yz} \\ \sigma_{xz} & \sigma_{yz} & \sigma_{zz} \end{bmatrix} \quad \text{becomes} \quad \sigma = \begin{Bmatrix} \frac{\sigma_{yy}-\sigma_{xx}}{\sqrt{2}} \\ \frac{2\sigma_{zz}-\sigma_{xx}-\sigma_{yy}}{\sqrt{6}} \\ \frac{2\sigma_{yz}}{\sqrt{2}} \\ \frac{2\sigma_{xz}}{\sqrt{2}} \\ \frac{2\sigma_{xy}}{\sqrt{2}} \end{Bmatrix}. \tag{4.2}$$

Note that $\boldsymbol{\sigma}$ has six independent components while σ is five dimensional. The pressure is the remaining independent degree of freedom in this formulation. Since the stress can be considered to consist of a magnitude and a direction in the deviatoric stress space, with the definition of the vectorized form of the deviatoric stress it is possible to use a dot product to understand the relationship between stress states. The coaxiality, $\phi_{\mathrm{a}}^{\mathrm{b}}$, between σ_{a} and σ_{b} is calculated as:

$$\phi_{\mathrm{a}}^{\mathrm{b}} = \cos^{-1}\left(\frac{\sigma_{\mathrm{a}} \cdot \sigma_{\mathrm{b}}}{\|\sigma_{\mathrm{a}}\|\|\sigma_{\mathrm{b}}\|}\right). \tag{4.3}$$

If σ_{a} and σ_{b} have the same direction in deviatoric stress space then $\phi_{\mathrm{a}}^{\mathrm{b}}$, which is the angle between the two vectors, will be 0. The smaller the magnitude of $\phi_{\mathrm{a}}^{\mathrm{b}}$, the more closely aligned are the two stress states being compared. In general $\phi_{\mathrm{a}}^{\mathrm{b}}$ will have a maximum value of 180° which occurs when the stresses point in opposite directions in deviatoric stress space. Note that $\phi_{\mathrm{a}}^{\mathrm{b}} = \phi_{\mathrm{b}}^{\mathrm{a}}$ and the two may be used interchangeably. Throughout this paper a and b may take the value of m to represent macroscopic stress, c to represent crystal stress, and v to represent a yield surface vertex stress.

4.2.2 Single crystal yield surface

Yield surfaces dictate how a material may plastically deform. We consider the case of face centered cubic (FCC) crystals deforming via slip on $\{111\}$ planes in $\langle 1\bar{1}0\rangle$

directions [12]. Slip occurs if the resolved shear stress, τ^α, on a slip system α is equal to the critical resolved shear stress, g^α, on that system, as in:

$$\tau^\alpha \equiv (\boldsymbol{b}^\alpha \otimes \boldsymbol{m}^\alpha) : \boldsymbol{\sigma} = g^\alpha, \tag{4.4}$$

where $\boldsymbol{b}^\alpha$ and $\boldsymbol{m}^\alpha$ are the slip direction and slip plane normal for the α slip system, respectively, and $\boldsymbol{\sigma}$ is the stress state in the crystal [20]. In the rate dependent case g^α is a function of temperature and strain rate; in the rate independent case it is not. Rate independence is the limit of behavior for vanishing strain rate sensitivity. Given the low rate sensitivity of the metals of interest, the rate independent limit provides an excellent approximation to the rate dependent surface both algorithmically and conceptually [20, 36]. The single crystal yield surface (YS) is formed by, for each slip system, plotting in six-dimensional stress space the plane defined by equation 4.4. The inner envelope of all these planes is the YS [37]. If the stress is within that envelope for a given crystal, that crystal is elastically deforming. If the stress is on the surface, slip is occurring on the slip system which forms the face of the surface on which the stress lies, and the crystal is plastically deforming.

The YS is considered "open" if there is a direction in stress space for which no magnitude of stress will intersect the YS. For the plasticity formulation considered here, the FCC yield surface is open in the direction of hydrostatic stress ($\sigma_{xx} = \sigma_{yy} = \sigma_{zz}$). Therefore, we consider here the YS in deviatoric stress space only, where it is closed. The shape of the YS includes facets where one slip system is yielding, edges where between two and four slip systems are yielding, and vertices where at least five slip systems are yielding and "polyslip" may be said to occur [38]. Polyslip is a condition that can accommodate arbitrary deviatoric strain. For the case we consider here there are 24 facets corresponding to the positive and negative stresses on the 12 FCC slip systems and 56 vertices in the YS in deviatoric stress space. We treat the positive and negative vertices simultaneously,

thereby limiting ourselves to consider 28 vertices. The 56 vertices (or 28 positive vertices) that result from intersections of at least five slip systems on the FCC YS may be grouped into five distinct types or families of polyslip, which are discussed in Appendix B.

When the stress in a crystal is on the YS the strain increment is always perpendicular to the YS [39, 40]. This means that for any prescribed stress state it is likely that the strain will be limited to one of 24 directions, which are the perpendiculars to the facets. Also, for a proscribed strain state, the stress will likely be limited to one of 56 possible states, which are the YS vertices. The stress within crystals can never exceed the bounds of the yield surface, which grows with work hardening. Therefore, for crystals within an aggregate that is subjected to an increasing external stress, the stress within each crystal will first ramp up, presumably parallel to the external stress, until it reaches a facet of the YS. As the macroscopic load continues to increase there will be a strain increment, $\mathbf{d}\boldsymbol{\epsilon}$, in each grain perpendicular to the YS facet with a corresponding stress component parallel to $\mathbf{d}\boldsymbol{\epsilon}$; the remaining portion of the macroscopic stress with necessarily be parallel to the YS facet and will cause the stress within the grain to move in the direction of that remaining portion, towards another facet of the YS and eventually into a vertex in order to accommodate any arbitrary direction of macroscopic stress. This means that after a sufficient amount of plastic strain in a bulk material, it is likely that the deviatoric stresses within each crystal will correlate well with vertices on the YS [41].

4.3 Polycrystal aggregates

When analyzing experimental or simulation data from aggregates it is necessary to understand how information from the single crystals is transmitted to the bulk

level. This section begins with a brief description of crystal orientations and then proceeds to describe crystallographic fibers and pole figure calculation. Diffraction moduli as measured from experiments or simulations are also defined.

4.3.1 Crystal orientations

Each grain within an aggregate has a set of local orthonormal coordinate axes $(\boldsymbol{C}_1, \boldsymbol{C}_2, \boldsymbol{C}_3)$ tied to its crystal lattice. Any direction or plane within a grain is defined with respect to these axes. When describing the orientation of a grain relative to the coordinate system of the specimen or laboratory, $(\boldsymbol{S}_1, \boldsymbol{S}_2, \boldsymbol{S}_3)$, there is an orientation matrix $\mathbf{R}$ that acts as a transformation matrix taking a vector in crystal coordinates, $\boldsymbol{v}^{\boldsymbol{c}}$, into the sample framework, $\boldsymbol{v}^{\boldsymbol{s}}$:

$$\mathbf{R}\boldsymbol{v}^{\boldsymbol{c}} = \boldsymbol{v}^{\boldsymbol{s}}. \tag{4.5}$$

In addition to the orientation matrix, a grain's crystallographic orientation may be represented using an angle-axis parameterization [42–44]. One such parameterization is due to Rodrigues:

$$\boldsymbol{r} = \boldsymbol{n} \tan \frac{\beta}{2}, \tag{4.6}$$

where the Rodrigues vector, $\boldsymbol{r}$, is calculated from the axis of rotation, $\boldsymbol{n}$, (expressed in terms of the $\boldsymbol{S}_i$) and the angle of rotation about that axis, β. This parameterization will be used for plotting purposes in the data analysis.

It is important to note that the cubic crystals considered here have a high degree of symmetry, as discussed in Appendix A.

4.3.2 Crystallographic fibers

Since our ultimate goal is a better understanding of the information available from *in situ* diffraction experiments, we must examine data similar to that available

from such tests. A typical diffraction measurement shows information from all crystals having a particular crystal axis, $\boldsymbol{c}$, aligned with the scattering vector, $\boldsymbol{s}$. This includes all crystals with their orientation, $\mathbf{R}$, satisfying:

$$\mathbf{R}\boldsymbol{c} = \pm\boldsymbol{s}. \tag{4.7}$$

The collection of crystals satisfying that equation is the fiber of $\boldsymbol{c} \parallel \boldsymbol{s}$ and can be represented by $\mathbf{R}_{\{\boldsymbol{c}\}[\boldsymbol{s}]}$. This work focuses on situations with the scattering vector parallel to the specimen loading direction. For simplicity's sake, we refer to $\mathbf{R}_{\{hkl\}[001]}$ as "the hkl fiber." Several of the fibers considered in this study are shown through the Rodrigues space cubic fundamental region in figure 4.1. When crystal orientations are plotted in Rodrigues space all crystallographic fibers appear as a straight line [45].

If only the fundamental region of Rodrigues space is considered, i.e. the subset of all orientations that includes all symmetrically unique possible orientations given a certain crystal symmetry, each fiber may appear as several straight line segments, emerging from and reentering the fundamental region several times, as seen in figures 4.1(b)-4.1(d). This attribute of representing crystallographic fibers as straight line segments makes Rodrigues space an ideal choice for visualizing crystal properties throughout orientation space.

Returning now to the issue of YS vertex families, figure 4.2 demonstrates the existence of these families. It shows $\phi_{\mathrm{v}}^{\mathrm{m}}$ calculated from equation 4.3 using σ_{v} for each of the 28 positive vertices and $\sigma_{\mathrm{m}} = \left[0\ \frac{2}{\sqrt{6}}\ 0\ 0\ 0\right]$ (i.e. $\sigma_{zz} = 1$ and all other $\sigma_{ij} = 0$) for several fibers. For each fiber the crystal orientation has been taken into account in addition to crystal symmetries, $\mathbf{R}^{\mathrm{sym}}$, since the vertex stress states are relative to the crystal axes. Any orientation along a single fiber will result in the same degree of coaxiality between a vertex and the macroscopic stress. This is because the macroscopic stress is aligned with $\boldsymbol{s}$ used to calculate the fiber.

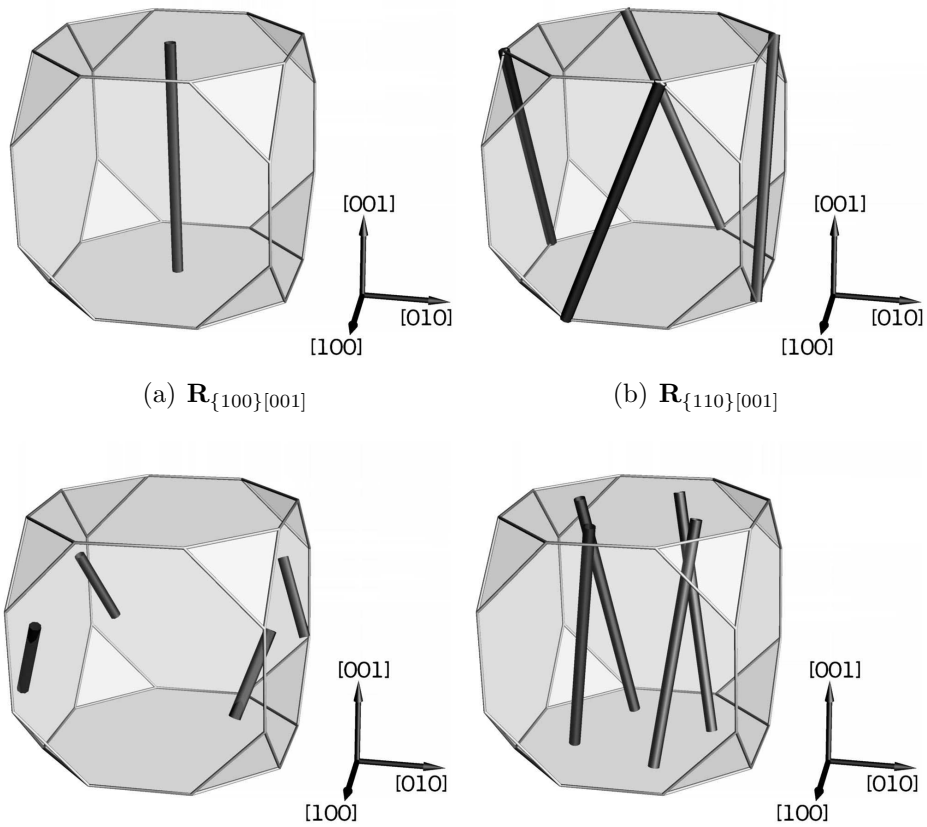

(a) $\mathbf{R}_{\{100\}[001]}$ (b) $\mathbf{R}_{\{110\}[001]}$

(c) $\mathbf{R}_{\{111\}[001]}$ (d) $\mathbf{R}_{\{311\}[001]}$

Figure 4.1: Several fibers shown in the cubic fundamental region of Rodrigues space. All of these fibers have a crystal axis parallel to the [001] sample direction, which is the tension axis in the simulations.

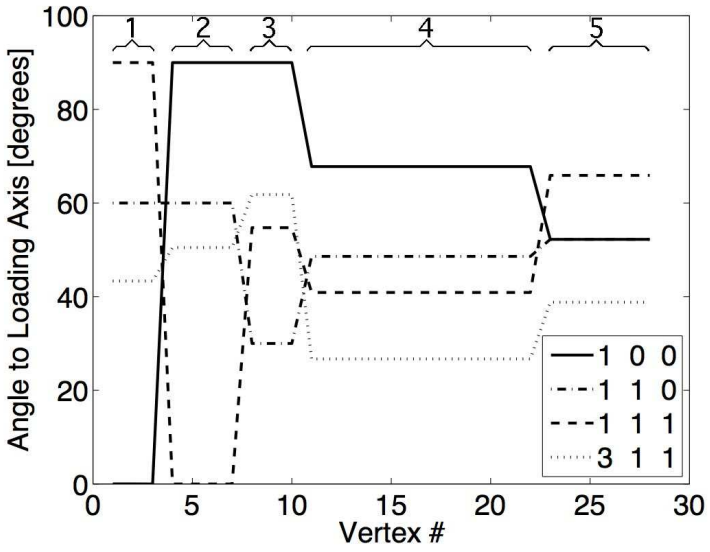

Figure 4.2: For several fibers, $\phi_{\mathrm{v}}^{\mathrm{m}}$ is shown for each of the vertices and a macroscopic stress state of uniaxial tension along the z-axis. Five symmetrically unique vertex families are labeled at the top of the figure.

Therefore only a single representative orientation is needed to calculate the vertex coaxialities to the macroscopic stress for each fiber, and $\phi_{\mathrm{v}}^{\mathrm{m}}$ is calculated using $\boldsymbol{\sigma}_{\mathrm{v}} = \mathbf{R}\mathbf{v}\mathbf{R}^T \quad \forall \quad \mathbf{R} \in \mathbf{R}^{\mathrm{sym}}$. The minimum value over all symmetries is saved as the coaxiality between that vertex and the macroscopic stress for that fiber.

The angle of coaxiality between the vertices and the given macroscopic stress state falls into 5 discrete values for each fiber. Vertices numbered 1 through 3 comprise the first family, numbers 4-7 comprise the second family, and so on. These families, numbered along the top of figure 4.2, correspond to types A-E of polyslip from [38].

It is important to recall that while figure 4.2 represents one specific macroscopic stress state, the same vertex families appear for any choice of macroscopic stress. The particular distances between each fiber and σ_{m} will change, but the existence of the fibers themselves depends only on crystal symmetry.

4.3.3 Pole data

Having identified those crystals which lie along a crystallographic fiber and contribute to a diffraction measurement, it is now possible to take averages of values along that fiber and construct pole figures. For example, to construct a lattice strain pole figure, for one choice of $\boldsymbol{c}$ the $\mathbf{R}_{\{\boldsymbol{c}\}[\boldsymbol{s}]}$ fiber is found for many sample directions. Each component of lattice strain can then be averaged among all of the crystals which lie along each fiber, giving the value of that component of lattice strain on the $\boldsymbol{c}$ lattice strain pole figure. In this study we use $\epsilon_{\langle hkl \rangle}$ to represent the normal component of lattice strain on the point on the hkl lattice strain pole figure calculated from $\boldsymbol{s} = [001]$.

4.4 Methodology

4.4.1 Data source

The data used here to explore stresses on a crystal level as related to macroscopic stresses and yield surface vertices come from the finite element simulations which are described in detail in chapter 3. Most of the results presented come from the dodecahedral meshes, but similar trends occurred for all meshes. Plasticity parameters representing a range of materials have been used, as well as elasticity parameters representing three levels of single crystal elastic anisotropy ($r_E = 1.0, 1.2, 1.7$). In general the results have been found not to depend on the choice of plasticity parameters, so a single set has been used for all data presented. Results are shown for several values of r_E.

4.4.2 Element orientations and fibers

The crystallographic, or lattice, orientation associated with each element has been considered in two different ways: one for calculation of crystallographic fibers, and one for plotting purposes. In all cases the element's lattice orientation is mapped back to the fundamental region of Rodrigues space. For some plots that display a distribution of values over all of orientation space, a piecewise linear polynomial representation is used over the fundamental region based on a mesh with 254 unique nodes. Each element in the simulation is associated with the node in the fundamental region whose orientation most closely matches its own. After all elements in the simulation have been processed there are anywhere from 50 to 800 crystals represented at each node in orientation space. It is then possible to plot, for example, the average of a value throughout the space, or the standard deviation of a value amongst all crystals which nominally share an orientation. For calculating which elements belong to which fibers, the elements' orientations are used directly without reference to a discretization of orientation space.

The elements contributing to a fiber are found by first calculating the misorientation angle, θ, between each element and $\mathbf{R}_{\{\boldsymbol{c}\}[\boldsymbol{s}]}$ via equation 4.8, which takes advantage of the fact that both $\boldsymbol{c}$ and $\boldsymbol{s}$ are unit vectors:

$$\theta = \cos^{-1}\left(\mathbf{R}\boldsymbol{c} \cdot \boldsymbol{s}\right). \tag{4.8}$$

The misorientation angle represents how much one orientation much be rotated to coincide with another [46]. When calculating θ we apply all crystal symmetries $\mathbf{R}^{\text{sym}}$ to the orientation of the element and test each resulting orientation, saving only the equivalent orientation which results in the lowest value of θ. Once the misorientation is found between each element's lattice and the desired fiber, a cutoff of a certain allowable misorientation is used to decide if an element's lattice lies on the fiber. We generally use $\theta < 5^\circ$ as the criterion. This is slightly larger than

a typical value from diffraction experiments, but to provide a reasonable number of elements for each fiber this value is necessary. Elements can now be treated in groups by fiber, which is similar to the way crystals are grouped during data collection in diffraction experiments, as discussed in §4.3.2 and §4.3.3.

4.4.3 Comparing stresses

During the data analysis we use equation 4.3 to compare stress states where a and b can take the value of c for crystal stresses, m for macroscopic stress, and v for YS vertex stresses. The methods of finding σ_{m}, σ_{c}, and σ_{v} are described here.

The macroscopic stress state is always assumed to be purely uniaxial with tension aligned in the mesh z-direction. When the magnitude of the macroscopic stress is needed, it is found by averaging the individual elemental stresses over the entire mesh and taking the σ_{zz} component. When taking that average over all elements the actual values of the other stress components are non-zero but small, with a magnitude ranging between 0.2 and 2.0 MPa compared with a maximum $\sigma_{zz} \approx 180$MPa. Though the finite elements begin the simulation associated with a particular grain, each element is allowed to deform and undergo lattice reorientation independently; therefore each element is considered individually when examining crystal stresses.

Calculating the coaxiality of a crystal stress to a vertex stress is done by applying the elemental orientation as well as all crystal symmetries to the vertex stress and taking the minimum $\phi_{\mathrm{v}}^{\mathrm{c}}$ over all of those symmetries. The angle between any element's crystal stress and each vertex can be found, but in general only those elements contributing to a particular fiber are considered.

4.5 Simulation data set

The data available from FE simulations are presented here in terms of the relation of the crystal (elemental) stresses to the macroscopic stress. The total stress, including both the magnitude and the direction, experienced by any grain in a polycrystal aggregate is due to a combination of factors, including the macroscopic stress state, the orientation of the grain (which effects its apparent stiffness), and its neighborhood. Even for such a seemingly simple macroscopic stress state as uniaxial tension, significant grain to grain variation can exist as shown in figure 4.3, which demonstrates variations in both the magnitude of the deviatoric stress (figure 4.3(a)) and the pressure (figure 4.3(b)) for a mesh under load. The variations in average pressure throughout orientation space are large, but do not appear to be systematically related to orientation. The magnitude of the deviatoric stress, however, clearly is systematically related to crystal orientation. Larger stresses occur in crystals whose coordinate axes are less closely aligned with the sample tension axis.

The amount of variation based on orientation is more significant than the amount of variation at any particular orientation, as can be seen by comparing figure 4.3(a) and figure 4.4(a). Recall that each node in the orientation space mesh represents simulation results from between approximately 50 and 800 elements. Figure 4.4(a) shows the standard deviation of the deviatoric stress magnitude over all the elements contributing to each point in orientation space. The standard deviation has a smaller magnitude range and a different and distinct pattern from the averages. There is orienational dependance, but more specifically, it appears to be related to the fiber on which a crystal orientation lies. The patterns in figure 4.4(a) seem to match closely with the fibers in figure 4.1. Similar patterns appear in figure 4.5, which shows $\phi_{\mathrm{c}}^{\mathrm{m}}$ for the domain under load. The standard deviation of

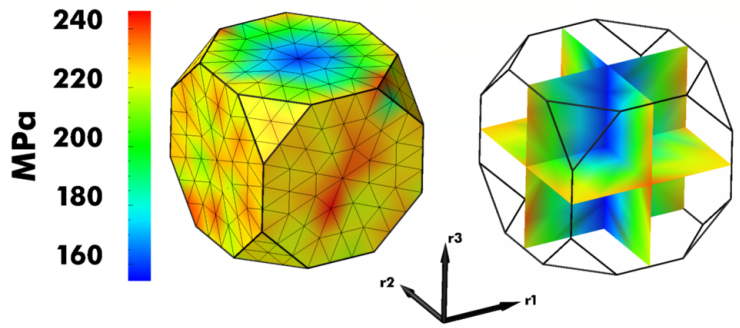

(a) Average magnitude of deviatoric stress

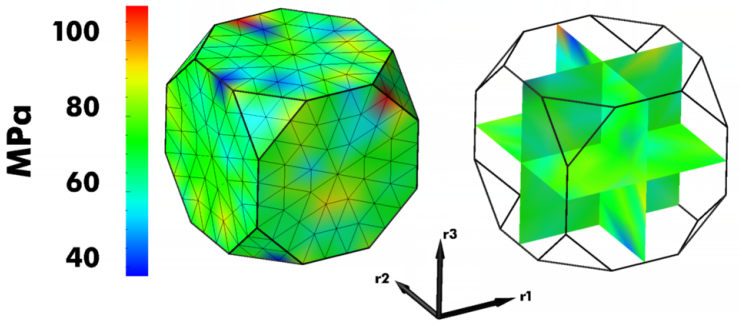

(b) Average pressure

Figure 4.3: Average stress magnitudes shown throughout orientation space. The value at each point in orientation space is the average of all elements sharing that orientation.

deviatoric stress magnitude and ϕ_c^m both appear to be lower for $\mathbf{R}_{\{111\}[001]}$ and $\mathbf{R}_{\{100\}[001]}$. This seems reasonable since a lower value of ϕ_c^m indicates a higher level of alignment between the crystal and macroscopic stresses, and stresses that are more highly aligned with the macroscopic stress have less source of variation.

Figures 4.3-4.5 show results for the highest stress occurring throughout the deformation; that is, the top load of the last unloading episode. The deviatoric stresses in the unloaded state (at the bottom of the same unloading episode) also exhibit patterns related to crystal orientation, as seen in figure 4.6. In the unloaded state the crystal stresses are no longer on the yield surface and therefore need not have any relation to the vertex stresses; this is played out in figure 4.7, which shows most crystals having deviatoric stress states more perpendicular than parallel to the macroscopic deviatoric stress.

The trends shown here appear to be independent of material parameters related to plasticity, but the elastic constants do have an effect in the unloaded case, as demonstrated in figures 4.8 and 4.9. The stress in the loaded states are almost indistinguishable from one value of r_E to the next, but for the higher value of anisotropy in the unloaded state, while the trends remain very similar, the range of stress magnitude decreases. Looking at the coaxialities in the unloaded state (figure 4.9), it seems that the range of values and also the trends change slightly with changing anisotropy. In the more isotropic cases the least alignment between crystal and macroscopic stresses is along $\mathbf{R}_{\{100\}[001]}$ whereas it is seen along $\mathbf{R}_{\{311\}[001]}$ in the more anisotropic case. As mentioned previously, the crystal stress should not be expected to correlate well with the macroscopic stresses in general in the unloaded state as the macroscopic load is close to zero, so it is unclear the extent to which patterns in ϕ_c^m are significant in the unloaded state.

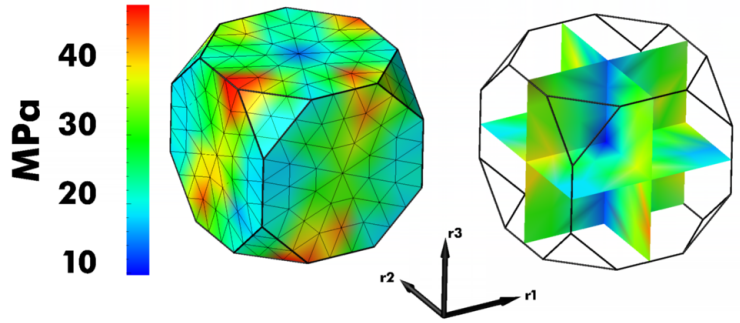

(a) Standard deviation of magnitude of deviatoric stress

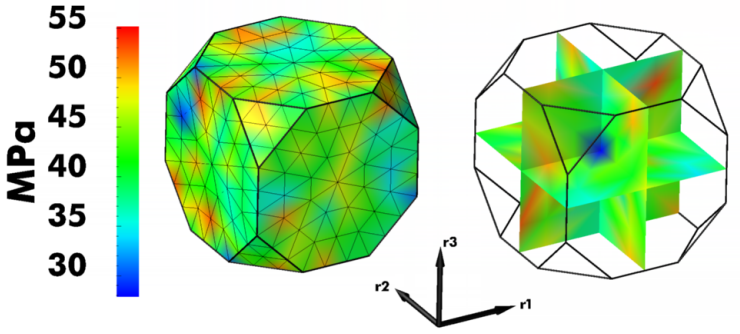

(b) Standard deviation of pressure

Figure 4.4: Standard deviation of stress magnitudes shown throughout orientation space. The value at each point in orientation space is due to all elements sharing that orientation.

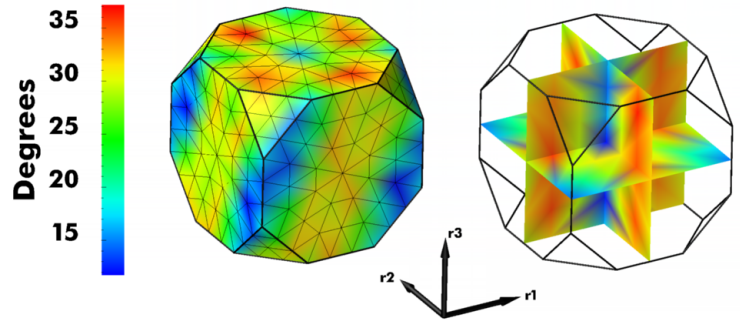

(a) Average ϕ_c^m

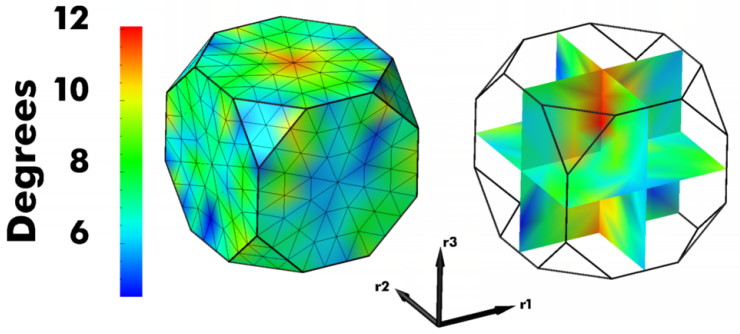

(b) Standard deviation of ϕ_c^m

Figure 4.5: Average and standard deviation of the angle of coaxiality between crystal stresses and the macroscopic stress shown throughout orientation space.

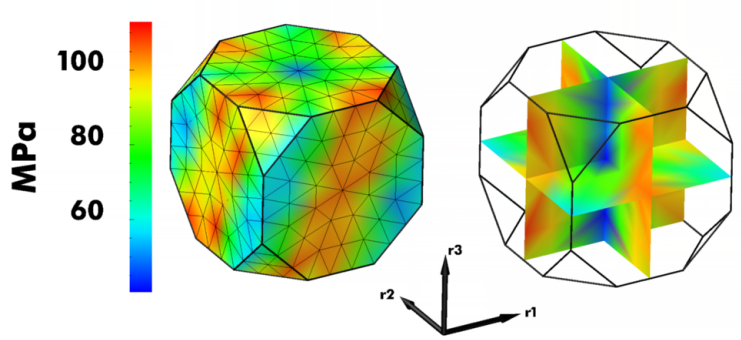

(a) Average deviatoric stress

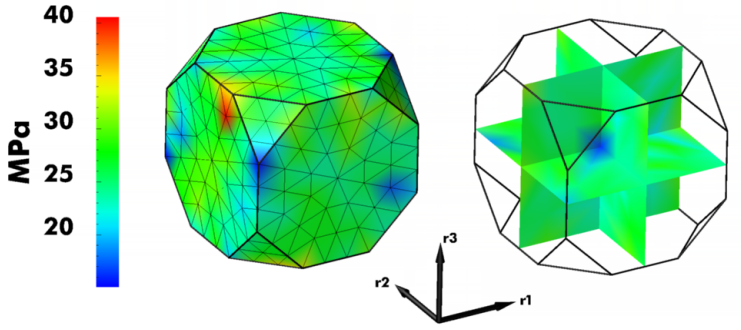

(b) Standard deviation of magnitude of deviatoric stress

Figure 4.6: Deviatoric stresses in the unloaded state shown throughout orientation space. The value at each point in orientation space is due to all elements sharing that orientation.

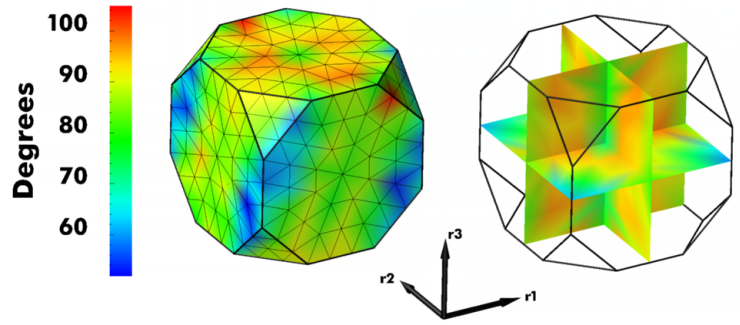

(a) Average ϕ_c^m

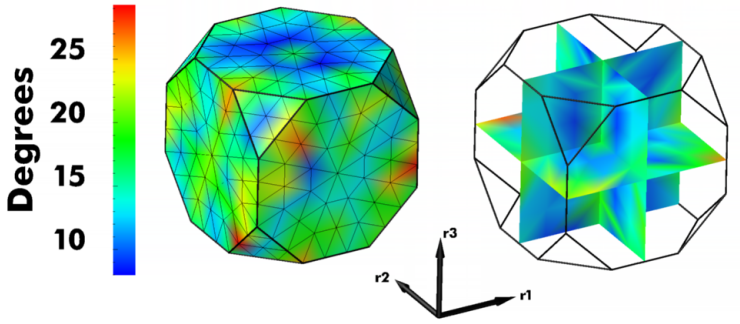

(b) Standard deviation of ϕ_c^m

Figure 4.7: Coaxiality between crystal and macroscopic stresses in the unloaded state shown throughout orientation space. The value at each point in orientation space is due to all elements sharing that orientation.

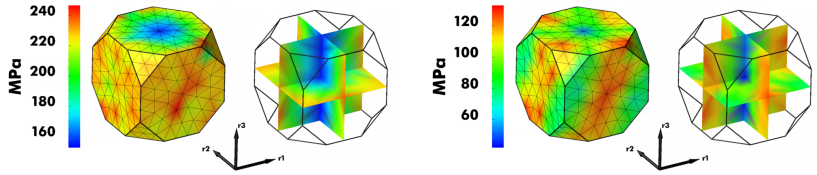

(a) r_E=1.0: high load

(b) r_E=1.0: unloaded

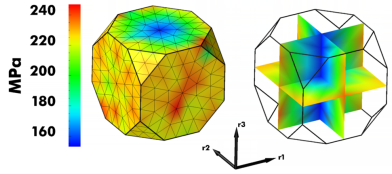

(c) r_E=1.2: high load

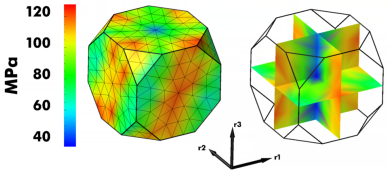

(d) r_E=1.2: unloaded

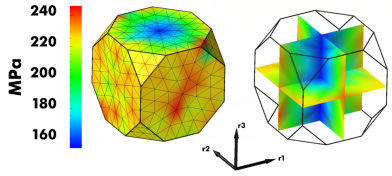

(e) r_E=1.7: high load

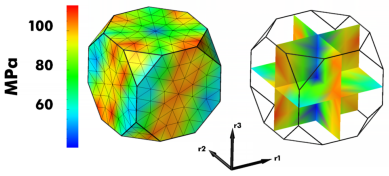

(f) r_E=1.7: unloaded

Figure 4.8: Average magnitude of deviatoric stress in both loaded and unloaded states for several values of elastic anisotropy.

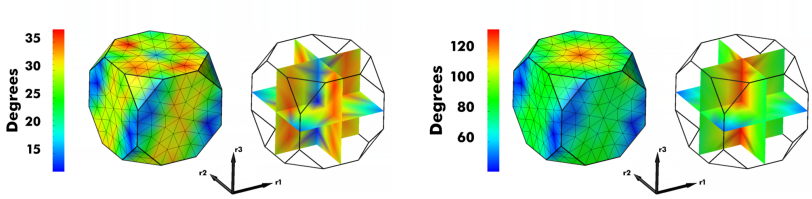

(a) r_E=1.0: high load (b) r_E=1.0: unloaded

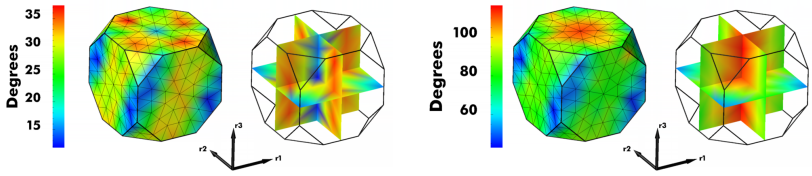

(c) r_E=1.2: high load (d) r_E=1.2: unloaded

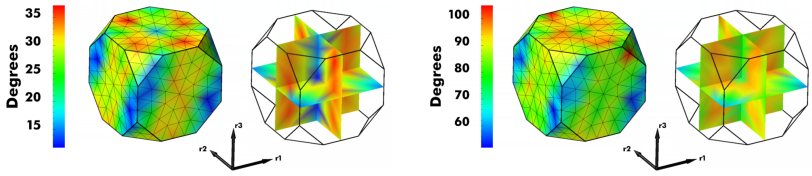

(e) r_E=1.7: high load (f) r_E=1.7: unloaded

Figure 4.9: Average coaxiality between crystal and macroscopic stresses, $\phi_{\mathrm{c}}^{\mathrm{m}}$, in both loaded and unloaded states for several values of elastic anisotropy.

4.6 Results for elastic moduli

Elastic moduli are calculated as a ratio of change in stress to change in strain for different crystal lattice directions, as in equation 1.6. Since neither of those quantities are generally measured individually on bulk polycrystalline specimens, some assumptions must be made. The lattice strains measured by *in situ* diffraction tests are averaged over all crystals contributing to a fiber, with the assumption that each crystal contributing to that fiber shares the same lattice strain. The crystal stresses cannot be measured, so the usual assumption for calculating diffraction elastic moduli is that each crystal experiences the macroscopic stress state, regardless of crystal orientation. Figure 4.10 explores the validity of the first assumption and figure 4.11 explores the second.

The variation in strain along a fiber is either slightly less than or approximately equal to the variation in strain between different fibers, as seen in figure 4.10. The assumption of all crystals along a fiber sharing a common strain state is not a particularly strong one, but cannot be improved upon at this time, and is used for modulus calculation. The assumption of all crystals in the domain sharing a common stress state equal to the macroscopic stress state is not a good one, as seen in figure 4.11. In experiments it is not possible to measure the stresses directly, but in finite element simulations a closer examination is possible. It is interesting to note that typically anisotropy in the elastic response is calculated as being primarily due to differences in strains between crystals of different orientations, whereas the more significant differences between fibers appear to be in the stresses experienced by the different crystals. The differences that result in the crystal moduli between an assumption of the macroscopic stress state and the use of the actual average stress state for each fiber are shown in figure 4.12. The diffraction elastic anisotropy, r_D, would be calculated as $73.0/59.5 = 1.23$ if the macroscopic

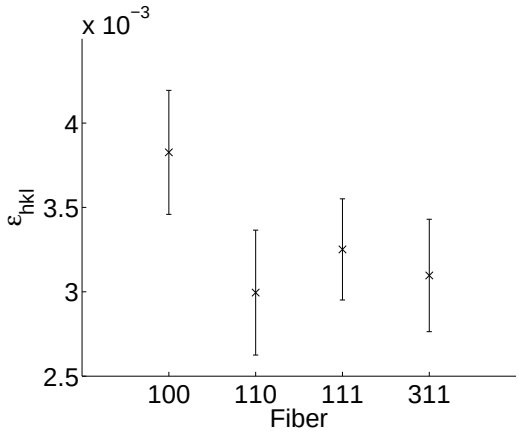

Figure 4.10: For each fiber, the average normal component of lattice strain in the specimen loading direction is shown along with error bars indicating the standard deviation of that strain amongst all elements contributing to the fiber. The data are shown for the maximum plastic strain occurring during the simulation.

stress is used in calculating $E_{\langle 111 \rangle}$ and $E_{\langle 100 \rangle}$, but it would be 80.9/51.9 = 1.56 if the fiber stress is used in addition to the fiber strain in the calculations; the single crystal anisotropy in this simulation is r_E=1.7. An explanation of the difference between the macroscopic and fiber stresses can be found in the yield surface and is explored in the following section.

4.7 Discussion of stress coaxialities

4.7.1 Vertex stress vs. macroscopic stress

Since we assume that, as crystals deform, their stress states tend towards vertices in the yield surface instead of towards the macroscopic stress state, it is important to know how closely aligned the vertices are with the macroscopic stress. That alignment influences which vertex is most likely to be active for any particular fiber. The coaxiality of each vertex to the macroscopic stress was shown in figure 4.2.

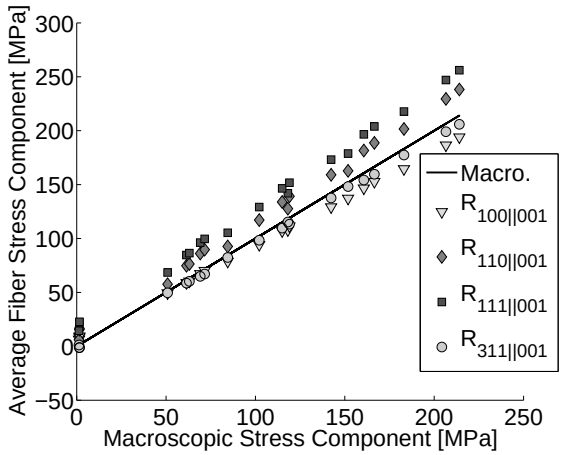

Figure 4.11: The average normal component of stress for each fiber is shown as a function of macroscopic stress during all unloading episodes. The solid line represents what would be seen if the crystal stresses matched the macroscopic stress.

Each fiber has one vertex family that is most closely aligned with the macroscopic stress. For $\mathbf{R}_{\{100\}[001]}$ and $\mathbf{R}_{\{111\}[001]}$, $\phi_{\mathrm{v}}^{\mathrm{m}}$ is 0°, or perfect alignment for vertex families 1 and 2, respectively. For $\mathbf{R}_{\{110\}[001]}$ and $\mathbf{R}_{\{311\}[001]}$ the closest vertex is much farther away, at 30° and approximately 26.7°, respectively. Looking again to figure 4.5(a), it appear that the angle between the crystal stresses and the macroscopic stress for the 110 and 311 fibers is approximately $30 - 35°$, which is consistent with the separation between those fibers' vertex stresses and the macroscopic stress.

4.7.2 Crystal stress vs. vertex stress

When examining the relationship of crystal stresses to vertex stresses, we are concerned primarily with those elements contributing to fibers that may be measured during *in situ* diffraction experiments. Figure 4.13 shows a histogram of $\phi_{\mathrm{c}}^{\mathrm{v}}$ for each fiber, indicating each element's distance to the most closely aligned vertex family, and also includes a histogram of which vertex family generates that value.

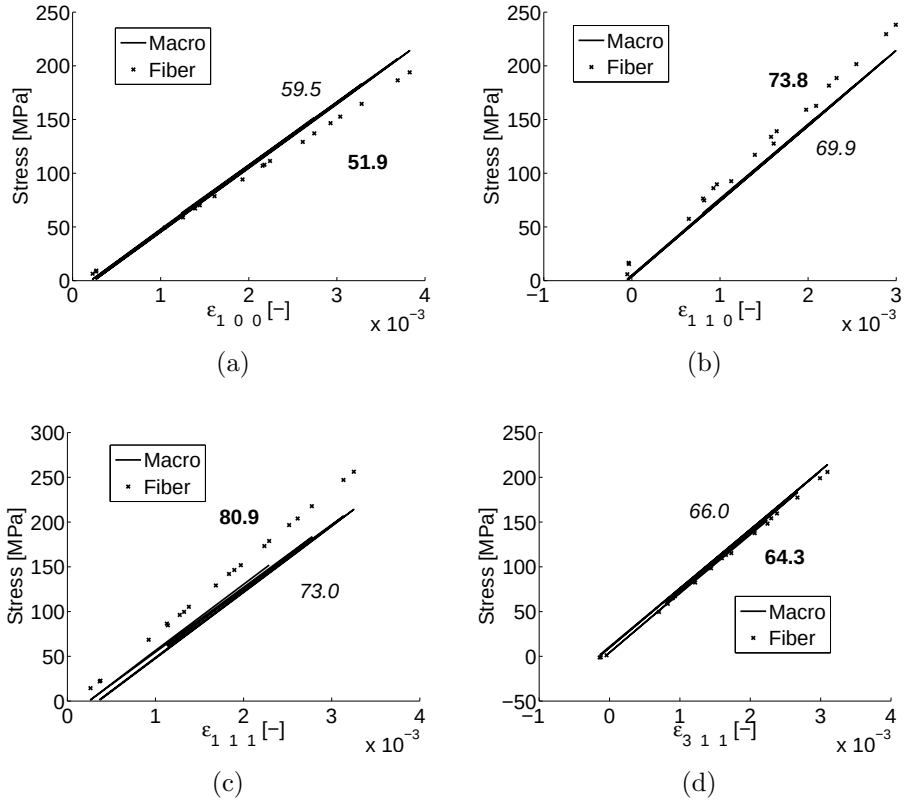

Figure 4.12: For each fiber, the stress is plotted as a function of average normal lattice strain. Both the macroscopic stress and the fiber stress are used. The slope of each line in GPa, which is the directional elastic modulus for that fiber, is printed on the plot in lighter italic type for the assumption of macroscopic stress, and in bolder type when using the fiber stress. For this simulation, r_E=1.7.

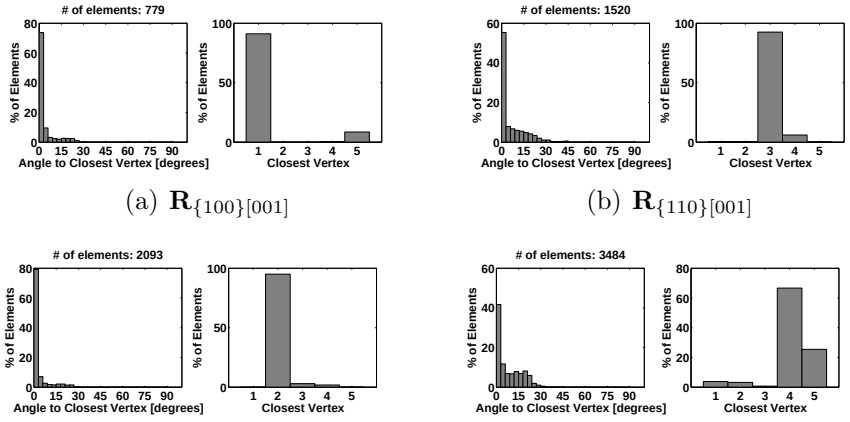

(a) $\mathbf{R}_{\{100\}[001]}$ (b) $\mathbf{R}_{\{110\}[001]}$

(c) $\mathbf{R}_{\{111\}[001]}$ (d) $\mathbf{R}_{\{311\}[001]}$

Figure 4.13: Histograms of $\phi_{\mathrm{c}}^{\mathrm{v}}$ for the nearest vertex family and which vertex family that is for crystal stresses from four fibers.

These data are for the peak load in the last unloading episode, at approximately 8% specimen strain. Compare figure 4.13 to figure 4.2. The most popular vertex family for each fiber in figure 4.13 matches the vertex family in figure 4.2 with the smallest value of $\phi_{\mathrm{v}}^{\mathrm{m}}$ for that fiber. Recall that figure 4.2 has been generated without using FE simulations. The coaxialities in that figure are based solely on crystal orientation for each fiber and YS vertices which are tied to the crystal lattice, along with an assumed macroscopic stress state. In contrast, the coaxialities in figure 4.13 are calculated directly from the simulation results. Each element has a particular orientation, and using that orientation and the stress which results from the simulation, $\phi_{\mathrm{c}}^{\mathrm{v}}$ is calculated. The stresses tend towards the vertex family that is most closely aligned with the macroscopic stress state, which confirms the assumption that crystal stress will tend towards YS vertices and will be only as closely aligned with the macroscopic stress as is possible given the vertices on the crystal YS. Certain fibers have more variation than others in terms of which vertex is most likely to be active. This corresponds to the fibers that have no vertex particularly well aligned with the macroscopic stress, i.e. $\mathbf{R}_{\{110\}[001]}$ and $\mathbf{R}_{\{311\}[001]}$.

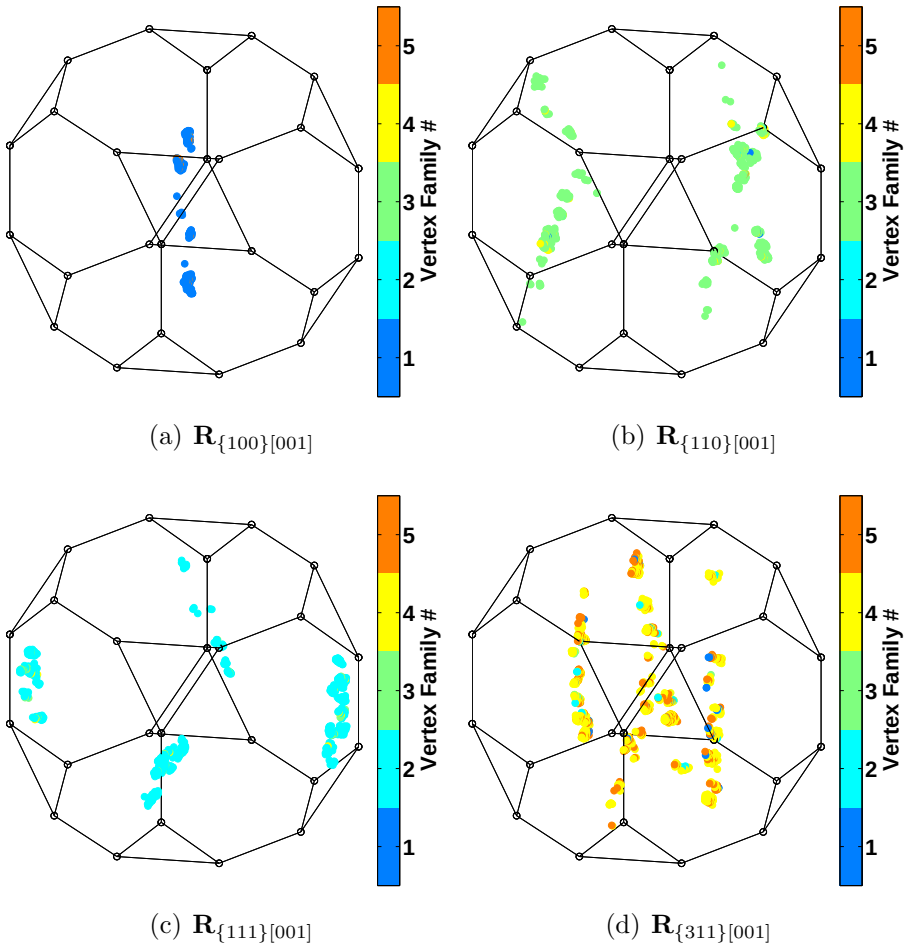

(a) $\mathbf{R}_{\{100\}[001]}$ (b) $\mathbf{R}_{\{110\}[001]}$

(c) $\mathbf{R}_{\{111\}[001]}$ (d) $\mathbf{R}_{\{311\}[001]}$

Figure 4.14: Each element contributing to a fiber, colored by the vertex family to which the crystal stress most closely aligns.

The variation in angle to the nearest vertex does not appear to be related to a crystal's orientation within a fiber, as is shown in figure 4.14 where each element in the fiber appears as a point in Rodrigues space colored according to the vertex family that is active. Looking at figure 4.14(d), the majority of the elements are associated with vertex family 4, but the spattering of 1, 2, and 5 appear evenly distributed along the length of the fiber.

When researchers calculate elastic moduli from diffraction experiments, they must make some assumption about the stress state of the crystals. The usual assumption is that the crystal stress matches the macroscopic stress. Figure 4.15

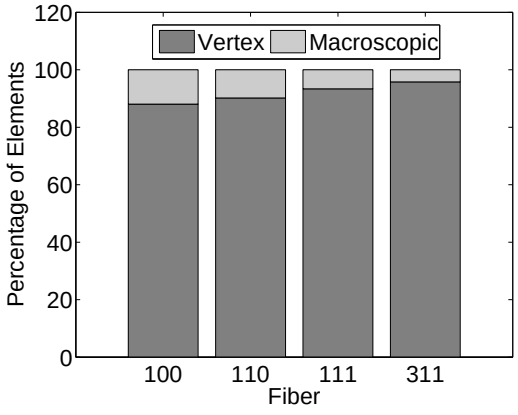

Figure 4.15: The percentage of elements contributing to each fiber that have stresses more closely aligned with the nearest vertex stress than with the macroscopic stress, and vice versa.

demonstrates how good or bad that assumption may be. It depicts the percentage of elements with a crystal stress more closely aligned with the nearest vertex stress versus those most closely aligned with the macroscopic stress for each fiber. The vast majority of elements are more closely aligned with the nearest vertex stress than with the macroscopic stress state. That is true both for fibers where a vertex is very highly aligned with the macroscopic stress and fibers for which the alignment is less close. At least 85% of the elements contributing to each fiber have a lower value of $\phi_{\mathrm{c}}^{\mathrm{v}}$ than $\phi_{\mathrm{c}}^{\mathrm{m}}$ (indicating closer alignment to the vertex stress than the macroscopic stress) regardless of elastic or plastic material parameters.

4.7.3 Elastic moduli

Considering the information regarding alignment of the vertex stresses with the macroscopic stress for the 100 and 111 fibers, it is at first surprising that there is not greater agreement between the crystal stresses for those fibers and the macroscopic stress. Part of that difference may be due to the 5° misorientation angle

Table 4.1: Magnitude of the deviatoric vectorized form of each YS vertex family.

Vertex Family Number	Relative magnitude of v
1	2.00
2	3.00
3	3.46
4	2.65
5	2.45

allowed between the crystal lattice and a true fiber orientation. Calculating $\phi_{\mathrm{v}}^{\mathrm{m}}$ using a crystal orientation 5° off from the fiber can result in a change in the value of approximately 8°. Therefore, for crystals actually participating in the measurement, the YS vertex nearest to the loading direction will in fact have some small separation, even for the 100 and 111 fibers.

In addition to the orientation of the deviatoric crystal stress for various fibers, the magnitude of the overall stress is important. In fact, it is the magnitude of the normal crystal stress in the global z-direction that should ultimately be used to determine the diffraction moduli. Since we have determined that the fiber stresses will be strongly correlated with the YS vertex stresses, we can use additional knowledge of the vertex stress magnitudes to estimate the relative stress magnitudes for the various fibers. We assume that g^{α} grows uniformly for all slip systems (ignoring latent hardening). Since the vertex stresses are all calculated based on the intersections of facets in the YS, as the size of the YS grows the vertex stresses will grow in a constant proportion to each other. We can determine their relative magnitude by taking the norm of their vector representations, which are shown in table 4.1. For the particular loading considered here (i.e. uniaxial

tension in the z-direction) each fiber has a particular preferred vertex and it is then possible to use the relative magnitudes of the vertex stresses to estimate the relative magnitudes of the fiber stresses. One additional piece of information is needed to determine an estimate for the particular stress magnitude instead of only ratios of magnitude. We must know how the fiber stresses relate to the macroscopic stress. This is highly dependent on the texture of the material as well as the multiplicity of the crystal orientations. If a specimen has many more crystals on one fiber we can expect that fiber to be weighted more heavily in the macroscopic stress. The simulations used here have relatively uniform texture, so no weighting by ODF will be used. In cubic materials the {311} planes have very high multiplicity. The 311 fiber stress is often very close to the macroscopic stress. To find an estimate for the fiber stresses we can therefore make the following assumptions:

1. The deviatoric crystal stresses for each fiber are equal to the vertex stress for the vertex family with the lowest $\phi_{\mathrm{v}}^{\mathrm{m}}$ for that fiber
2. The macroscopic σ_{zz} is equal to σ_{zz} for the 311 fiber.
3. The ratio of deviatoric fiber stress magnitudes goes as the ratio of vertex magnitudes for the preferred vertex family for each fiber.
4. The pressure (mean stress) on each fiber is identical and equal to the macroscopic pressure.

The method of going from the measured macroscopic stress state to the estimate of stress in each fiber is as follows: for the peak of an unloading episode, while the aggregate is actively plastically deforming, assume the macroscopic stress, $\boldsymbol{\sigma}_{\mathrm{macro}}$ has the form

$$\boldsymbol{\sigma}_{\mathrm{macro}} = \begin{bmatrix} 0 & 0 & 0 \\ 0 & 0 & 0 \\ 0 & 0 & T \end{bmatrix}, \tag{4.9}$$

where T is the measured macroscopic stress. The zz component of the 311 fiber stress is then also equal to T, as per assumption 2 above. The pressure, π, is $T/3$ for the macroscopic stress as well as on each fiber, as per assumption 4. The deviatoric fiber stress vector for the 311 fiber, σ_{311} has a coaxiality angle ϕ^{m}_{311} to σ_{macro} as described in §4.7.1. Since we know the magnitude of the projection of σ_{311} in the σ_{macro} direction, we can find the magnitude of the entire vector from:

$$\|\sigma_{311}\| = \frac{\sigma^{311\prime}_{zz}}{\cos\phi^{\mathrm{m}}_{311}} = \frac{2T}{3\cos\phi^{\mathrm{m}}_{311}}. \tag{4.10}$$

Then, using assumption 3, the magnitude of any other fiber stress can be calculated as:

$$\|\sigma_{hkl}\| = \|\sigma_{311}\| \times \frac{\|v_{hkl}\|}{\|v_{311}\|}, \tag{4.11}$$

where $\|v_{hkl}\|$ is the magnitude of the vertex family prefered by the hkl fiber. Finally, the zz component of any fiber stress can be found by again using the projection in equation 4.10 for the proper hkl and adding the pressure term back in:

$$\sigma^{hkl}_{zz} = \pi + \sigma^{hkl\prime}_{zz} = \pi + \frac{2T}{3}\frac{\cos\phi^{\mathrm{m}}_{\mathrm{hkl}}}{\cos\phi^{\mathrm{m}}_{311}}\frac{\|v_{hkl}\|}{\|v_{311}\|}. \tag{4.12}$$

Equations 4.9-4.12 apply to only the peak loads. To find the estimate of fiber stress after the load has been decreased and the crystals stresses are no longer on the yield surface some additional assumption is necessary. The simplest is to find $\Delta\sigma_{macro}$ between the current load and the most recent load resulting in plastic deformation and apply the same change in stress to each fiber stress. Figure 4.16 shows the results of these estimations. How accurate is that assumption? By examining the eigenvectors of the crystal stresses it is possible to study how the stress directions change during unloading. Figure 4.17 shows, for each fiber, how the angle between the macroscopic tension direction and the eigenvector (corresponding to the largest eigenvalue) of the crystal stress changes during unloading. Load numbers 1, 6, 11, and 16 are peak loads and load numbers 5, 10, 15, and 20

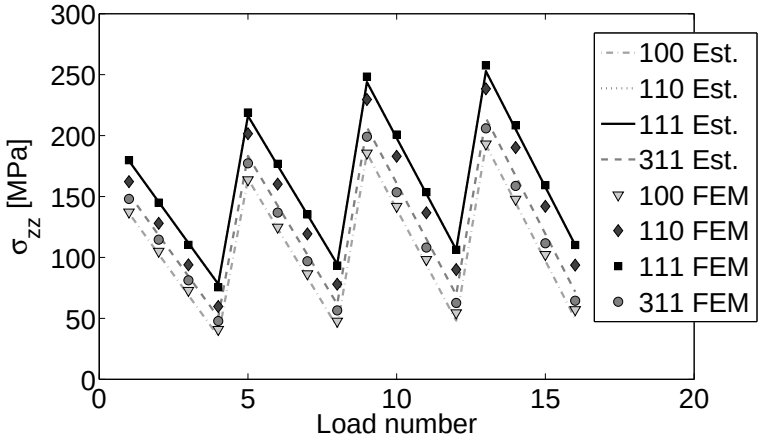

Figure 4.16: Estimate of fiber stress based on new assumptions along with the average fiber stress from the simulation. The estimate of the $\mathbf{R}_{\{110\}[001]}$ stress is almost immediately below the estimate of the $\mathbf{R}_{\{111\}[001]}$ stress and the two cannot be distinguished on this plot.

are the unloaded states. Results are shown for both the elastically isotropic case and one anisotropic case. In the completely unloaded case the eigenvectors are not at all well aligned with the loading axis, as expected. In the beginning of each unloading episode, however, the eigenvectors slowly move further from the parallel state. If during unloading the crystal stresses all reduced load radially towards the origin of stress space the lines in figure 4.17 would be horizontal with a constant angle between each fiber stress and the macroscopic tension. That is clearly not the case.

Looking at the eigenvectors of the $\Delta\sigma$ matrix, formed by subtracting the crystal stress states at the peak of each episode from the crystal stresses at the third load of each episode, gives an indication of the direction of unloading. The coaxialities between those eigenvectors and the tension direction are shown in figure 4.18. For the isotropic case, figure 4.18(a), the values are all essentially zero, indicating unloading perfectly parallel to the macroscopic load for each fiber (though each fiber still has its own stress state related to the YS, as seen above). For the

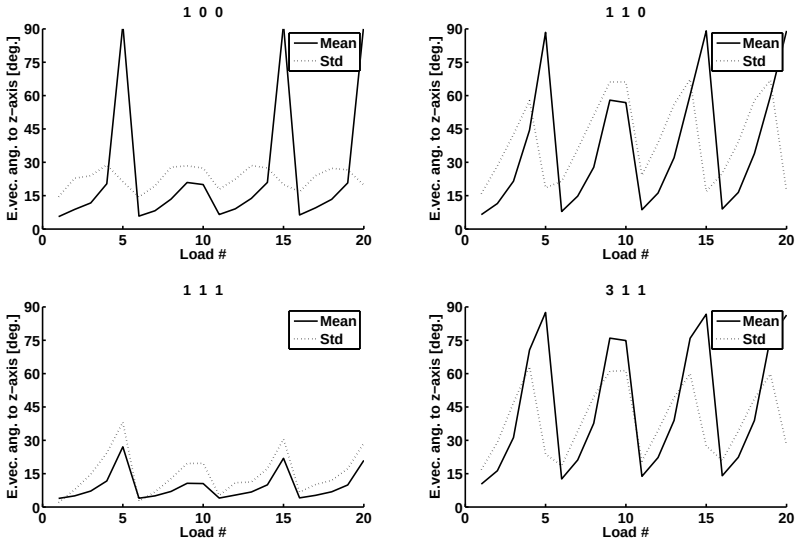

(a) $r_E = 1.0$

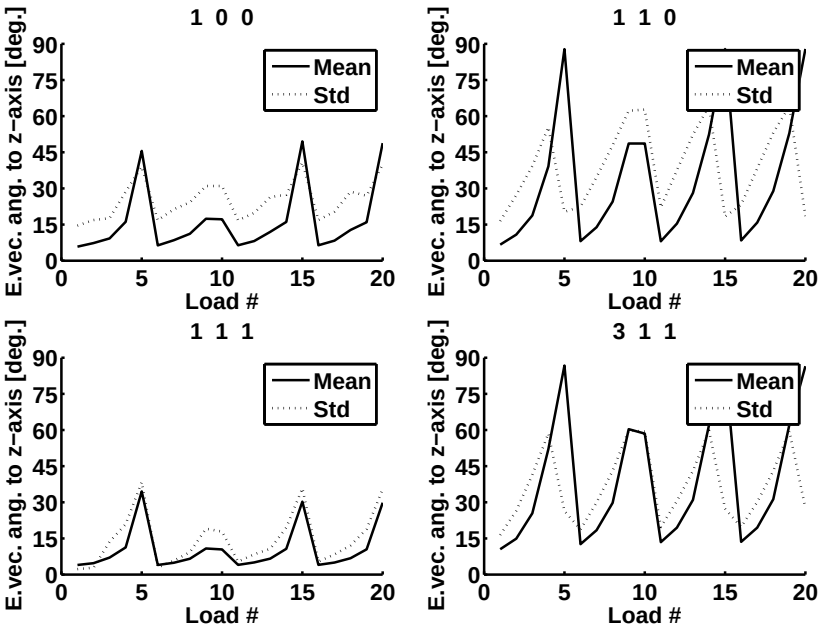

(b) $r_E = 1.7$

Figure 4.17: Coaxiality between the eigenvector corresponding to the first principal stress component and the tension axis. The averages and standard deviations are over all elements contributing to each fiber.

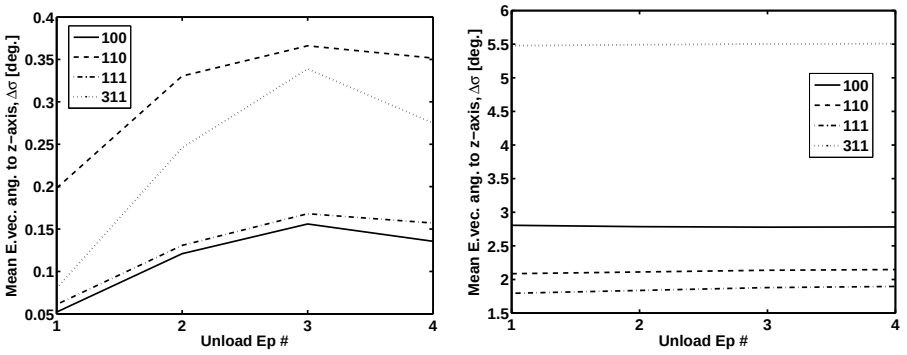

(a) $r_E = 1.0$ (b) $r_E = 1.7$

Figure 4.18: Coaxiality between the eigenvector corresponding to the first principal component of the $\Delta\sigma$ matrix (calculated over the first three loads of each unloading episode) and the tension axis.

anisotropic case the coaxialities are separate for each fiber, but in all cases are quite close to zero, indicating near-parallel unloading to the macroscopic stress. However, if the fiber unloading is parallel to the macroscopic unloading, why are all slopes in figure 4.11 not parallel? Examining the eigenvalues of the $\Delta\sigma$ matrices, as in figure 4.19 provides further insight. In the isotropic case, figure 4.19(a), the amount of unloading is identical for all fibers, as expected. No elastic anisotropy allows no variation in unloading between fibers (though variations in the peak load, governed by plastic anisotropy, are still present and expected). For the anisotropic case, as in figure 4.19(b), however, each fiber unloads a different amount, though all unload in essentially parallel directions. This change in amount of unloading contributes to the different slopes in figure 4.11.

Table 4.2 shows estimates of $E^D_{\langle hkl \rangle}$ and r_D using the average lattice strains for each fiber and three methods of determining the fiber stress: fiber stress equals macroscopic stress, fiber stress as described immediately above using the YS vertices, and fiber stress averaged over all contributing elements.

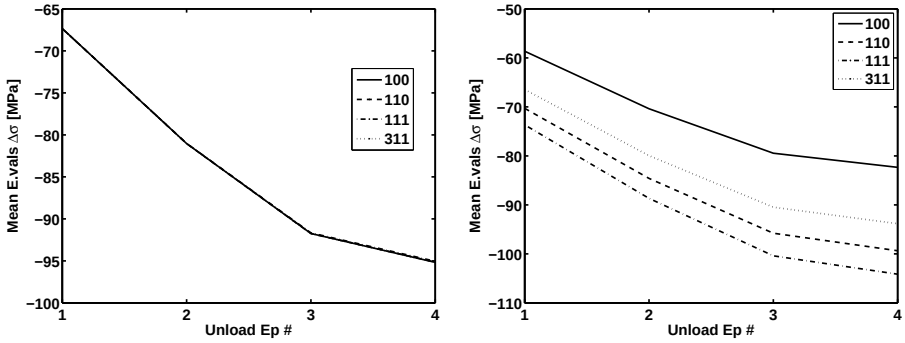

(a) $r_E = 1.0$ (b) $r_E = 1.7$

Figure 4.19: First principal eigenvalues of $\Delta\sigma$ calculated over the first three loads of each unloading episode.

Table 4.2: Diffraction moduli and calculated r_D for three methods of data reduction. "Macro" indicates that all fiber stress are assumed to have the macroscopic stress, "Proportional" indicates that the fiber stresses are calculated in proportion to their vertex stress magnitudes, and "FEM" indicates that the actual average crystal stresses from the FE simulations have been used. The same lattice strains are used for all three methods. The single crystal anisotropy r_E= 1.7 for this data.

	Macro	Proportional	FEM
$E^D_{\langle 100\rangle}$	59.5	59.0	51.9
$E^D_{\langle 110\rangle}$	69.9	70.9	73.8
$E^D_{\langle 111\rangle}$	73.0	74.2	80.9
$E^D_{\langle 311\rangle}$	66.0	66.0	64.3
r_D	1.23	1.26	1.56

4.8 Conclusions of yield surface application to stress estimation

Stresses in polycrystal aggregates cannot easily be measured within populations of crystals. When working with *in situ* measurements from diffraction data it is necessary to either know the material properties well and measure strain in many directions to estimate the stresses from the fully populated lattice strain tensors, or it is necessary to estimate the stresses from the measured lattice strains and assumptions about stress partitioning. Using knowledge of the single crystal yield surface and simulations of polycrystal aggregates deformed under uniaxial tension we have introduced a candidate set of assumptions to apply to stress determination for crystals along different crystallographic fibers. Examining stresses in crystals throughout orientation space it is visually apparent that separating and analyzing crystals by fiber is an appropriate method. After deformation has entered the plastic regime, crystal stresses will be aligned with vertices in the yield surface. Crystals along each fiber will tend towards certain preferred vertices in the yield surface and using the relative magnitude of those vertex stresses we estimate the values of the fiber stresses, based on the measured macroscopic stress. This provides an improvement over the common assumption of the macroscopic stress state applying to each crystal and gives a more accurate portrait of the stress distribution within a polycrystal aggregate.

CHAPTER 5

SUMMARY AND FINDINGS

Several aspects of modeling elastic anisotropy as observable from *in situ* diffraction experiments have been studied. The work began with a set of experiments on several aluminum-magnesium alloys which provided a comprehensive data set on which to base subsequent simulations and to which the results of those simulations have been compared. The experimental data included lattice strains measured in the axial direction during uniaxial tension loading of the specimens through several load excursions, accumulating 5-10% plastic strain in total for each material. The lattice strains were measured for four crystallographic fibers. The data revealed a slight dependence of the elastic anisotropy on the amount of magnesium in the alloy. This finding is consistent with some results in the literature. The amount of dependence is not sufficient to account for the total increase in r_E over handbook values necessary in the elastoplastic polycrystal plasticity finite element simulations to capture r_D from experiments. Uncertainty in individual crystal stiffnesses (e.g. c_{12}) of as little as 10-15% can change the resulting r_E up to 15-25%. It is possible, therefore, that actual single crystal anisotropies are somewhat greater than those tabulated in literature.

A large suite of FE simulations including meshes with rhombic dodecahedral, truncated octahedral, and cubic grain shapes was undertaken to explore any effects of grain discretization on the stress observed throughout the domain. While the elastic anisotropy was found to be independent of the grain discretization over the range of meshes tested here, significant systematic trends in terms of stress distribution throughout the domain were observed. The mesh comprising cubic grains, which have both the smallest number of neighbors and the fewest degrees of freedom within each grain, showed the most intergranular and least intragranular

stress variation, while the opposite is true for the octahedral grains, which have both the most neighbors and the most degrees of freedom within the grains. These trends were observed to be independent of the plasticity parameters over the range of values explored. Changes in r_E resulted in the same trend for all meshes: the stress variations at full load are independent of r_E but the stress variation in an unloaded state decreases significantly for higher values of r_E.

A final aspect of approaching the stresses observable in *in situ* ND experiments is to use the single crystal yield surface to make predictions of the stresses in various crystallographic fibers. A method has been presented to estimate stresses in different fibers based only on a measured macroscopic stress and knowledge of the yield surface vertices. This has limited capabilities since there are only five independent vertices in the FCC yield surface, but the method performs well in estimating stresses in the $\mathbf{R}_{\{100\}[001]}$ and $\mathbf{R}_{\{111\}[001]}$ fibers for the uniaxial loading studied. Since those two fibers represent the extremes of response in most FCC materials, accurately capturing the stresses in those fibers is a significant improvement over assuming identical stress states equal to the macroscopic stress in all grains throughout a polycrystal aggregate. The novel approach used takes into account the five unique vertex families and that crystal stresses will migrate towards those YS vertices based almost entirely on their lattice orientations (i.e. to which fiber they contribute).

Using the YS alone enables estimation of fiber stresses at full load (i.e. on the yield surface itself). As soon as elastic unloading takes place the crystal stresses begin to veer from the vertices as they retreat to the interior of the yield surface. Analysis of the eigenvectors of fiber stresses has shown that the crystal stresses do not unload radially, but rather parallel to the direction of the macroscopic stress. Each fiber, however, unloads at a different rate. This change in stress

(and its influence on the strains) determines the true polycrystal elastic anisotropy of the bulk. A more accurate representation of the elastic anisotropy requires taking into account these differences in both strain and stress components from one fiber to another; however, in analyzing simulation data along the same method generally available for experimental *in situ* diffraction data stress differences are not considered.

If the ultimate goal is to exactly reproduce results from experiments, the currently utilized FE formulation, implementation, or post-processing falls short. Stronger, stiffer crystals seem to deform more relative to more compliant grains than measurements from experiment indicate happens in a physical specimen. Using different grain discretizations does not alleviate that discrepancy, although it does allow more flexibility in focussing simulations towards applications wherein more grains are desired versus those where a greater number of degrees of freedom within each crystal are preferable. It is possible that with additional computing resources the number of grains could be increased allowing the elements contributing to each fiber to be more selective. Currently, misorientations of 5° from the fiber orientation are necessary to accumulate a sufficient number of contributing elements for each fiber. A smaller angular range could serve to focus the results instead of averaging over a larger portion of the total polycrystal, however with the current available resources there would not be a satisfactorily large sampling volume for each fiber if the orientational tolerance is decreased. This undesirable averaging may make stiffer crystals appear more compliant and vice versa.

If however, the ultimate goal is a greater understanding of stresses throughout all portions of a bulk's loading history, the YS provides a valuable and powerful tool for understanding stresses in crystals based on their orientation and the macroscopic stress state.

APPENDIX A

CUBIC CRYSTAL SYMMETRY

Crystal lattices are formed from regular repeating patterns of a "unit cell" of atoms and therefore have a large degree of symmetry. In cubic crystals the unit cell of the lattice is a hexahedron with all angles between faces 90° and all edge lengths equal to the single lattice parameter, a. In face-centered cubic crystals the lattice sites with atoms are all eight corners of the unit cell and the centers of all six faces. Any rotation, $\mathbf{G}$, that brings all atoms to occupied lattice sites when applied to the unit cell is a symmetry operation. This means that $\mathbf{G}\boldsymbol{v}^{\boldsymbol{c}}$, where $\boldsymbol{v}^{\boldsymbol{c}}$ is any directional vector in the crystal framework, cannot be distinguished from that vector $\boldsymbol{v}^{\boldsymbol{c}}$.

For example, in a cubic crystal a counter clockwise rotation of 90° about $\boldsymbol{C}_x$ will generate a new set of axes $\mathbf{G}\boldsymbol{C}_i = \boldsymbol{C}_i^g$ in which $\boldsymbol{C}_x^g = \boldsymbol{C}_x$, $\boldsymbol{C}_y^g = \boldsymbol{C}_z$, and $\boldsymbol{C}_z^g = -\boldsymbol{C}_y$. In fact, each of the $\boldsymbol{C}_i$ are 4-fold symmetry axes about which a rotation of $90°, 180°, 270°$ or 360° will result in an indistinguishable orientation. Table A.1 lists all unique cubic symmetries and shows $\boldsymbol{C}_i^g$ expressed in terms of $\boldsymbol{C}_i$ for each one [47]. There are many additional symmetry operations not listed in the table. For example, a rotation of 360° about any axis is a symmetry operation (in fact, the identity operation), and is therefore represented in the first line of the table. Also, a 90° rotation about $-\boldsymbol{C}_i$ is equivalent to a 270° rotation about $\boldsymbol{C}_i$ and need not be included explicitly in the group of symmetry operations. The rotation matrices which can be generated from the 24 symmetry operations in table A.1 compose $\mathbf{R}^{\text{sym}}$.

Since a crystal's orientation matrix, $\mathbf{R}$, takes a vector in crystal coordinates to sample coordinates and any member of $\mathbf{R}^{\text{sym}}$ creates a symmetrically equivalent copy of a vector in the crystal framework,

$$\mathbf{R}\boldsymbol{v}^{\boldsymbol{c}} = \mathbf{R}\mathbf{G}\boldsymbol{v}^{\boldsymbol{c}} = \boldsymbol{v}^{\boldsymbol{s}} \quad \forall \quad \mathbf{G} \in \mathbf{R}^{\text{sym}}, \tag{A.1}$$

Table A.1: Symmetry operations for cubic crystals, expressed in terms of an axis and a rotation in degrees about that axis. The new crystal axes, $\boldsymbol{C}_i^g$, resulting from the symmetry operation are given in terms of the original axes, $\boldsymbol{C}_i$.

Rotation axis	Angle [degrees]	$\boldsymbol{C}_x^g$	$\boldsymbol{C}_y^g$	$\boldsymbol{C}_z^g$
[100]	0	$\boldsymbol{C}_x$	$\boldsymbol{C}_y$	$\boldsymbol{C}_z$
[100]	90	$\boldsymbol{C}_x$	$\boldsymbol{C}_z$	$-\boldsymbol{C}_y$
[100]	180	$\boldsymbol{C}_x$	$-\boldsymbol{C}_y$	$-\boldsymbol{C}_z$
[100]	270	$\boldsymbol{C}_x$	$-\boldsymbol{C}_z$	$-\boldsymbol{C}_y$
[010]	90	$-\boldsymbol{C}_z$	$\boldsymbol{C}_y$	$\boldsymbol{C}_x$
[010]	180	$-\boldsymbol{C}_x$	$\boldsymbol{C}_y$	$-\boldsymbol{C}_z$
[010]	270	$\boldsymbol{C}_z$	$\boldsymbol{C}_y$	$-\boldsymbol{C}_x$
[001]	90	$\boldsymbol{C}_y$	$-\boldsymbol{C}_x$	$\boldsymbol{C}_z$
[001]	180	$-\boldsymbol{C}_x$	$-\boldsymbol{C}_y$	$\boldsymbol{C}_z$
[001]	270	$-\boldsymbol{C}_y$	$\boldsymbol{C}_x$	$\boldsymbol{C}_z$
[110]	180	$\boldsymbol{C}_y$	$\boldsymbol{C}_x$	$-\boldsymbol{C}_z$
[101]	180	$\boldsymbol{C}_z$	$-\boldsymbol{C}_y$	$\boldsymbol{C}_x$
[011]	180	$-\boldsymbol{C}_x$	$\boldsymbol{C}_z$	$\boldsymbol{C}_y$
[111]	120	$\boldsymbol{C}_y$	$\boldsymbol{C}_z$	$\boldsymbol{C}_x$
[111]	240	$\boldsymbol{C}_z$	$\boldsymbol{C}_x$	$\boldsymbol{C}_y$
$[\bar{1}11]$	120	$-\boldsymbol{C}_z$	$-\boldsymbol{C}_x$	$\boldsymbol{C}_y$
$[\bar{1}11]$	240	$-\boldsymbol{C}_y$	$\boldsymbol{C}_z$	$-\boldsymbol{C}_x$
$[1\bar{1}1]$	120	$\boldsymbol{C}_z$	$-\boldsymbol{C}_x$	$-\boldsymbol{C}_y$
$[1\bar{1}1]$	240	$-\boldsymbol{C}_y$	$-\boldsymbol{C}_z$	$\boldsymbol{C}_x$
$[11\bar{1}]$	120	$-\boldsymbol{C}_z$	$\boldsymbol{C}_x$	$-\boldsymbol{C}_y$
$[11\bar{1}]$	240	$\boldsymbol{C}_y$	$-\boldsymbol{C}_z$	$-\boldsymbol{C}_x$
$[\bar{1}10]$	180	$-\boldsymbol{C}_y$	$-\boldsymbol{C}_x$	$-\boldsymbol{C}_z$
$[\bar{1}01]$	180	$-\boldsymbol{C}_z$	$-\boldsymbol{C}_y$	$-\boldsymbol{C}_x$
$[0\bar{1}1]$	180	$-\boldsymbol{C}_x$	$-\boldsymbol{C}_z$	$-\boldsymbol{C}_y$

and $\mathbf{R}$ is symmetrically equivalent to $\mathbf{RG}$. Furthermore, any stress state $\boldsymbol{\sigma}$ in a crystal is indistinguishable from $\mathbf{G}^{\mathrm{T}}\boldsymbol{\sigma}\mathbf{G}$. When performing calculations with a crystal's orientation or stress it is important to apply all crystal symmetries before determining a final result.

APPENDIX B

YIELD SURFACE VERTEX FAMILIES

The 28 positive vertices in the single crystal yield surface represent five distinct types of polyslip. These are [100] tension, [111] tension, (100) [010] shear, [100] compression with (100) [011] shear, and (100) [010] shear with (110) [110] shear [41, 48]. For each of these types a unique vertex, $\mathbf{v}$, can be found via equation B.1 by taking the symmetric part of the outer product of the plane normal, $\boldsymbol{n}$, and the traction direction, $\boldsymbol{t}$, and then finding the deviatoric portion of that stress:

$$\boldsymbol{\sigma} = \mathrm{sym}(\boldsymbol{n} \otimes \boldsymbol{t}), \qquad \mathbf{v} = \boldsymbol{\sigma}'. \tag{B.1}$$

For example, the second family of vertices can be generated by finding the deviatoric stress state due to any of the following $(\boldsymbol{n}, \boldsymbol{t})$ pairs: $((111), [111])$, $((\bar{1}11), [\bar{1}11])$, $((1\bar{1}1), [1\bar{1}1])$, $((11\bar{1}), [11\bar{1}])$, $((\bar{1}\bar{1}1), [\bar{1}\bar{1}1])$, $((1\bar{1}\bar{1}), [1\bar{1}\bar{1}])$, $((\bar{1}1\bar{1}), [\bar{1}1\bar{1}])$, $((\bar{1}\bar{1}\bar{1}), [\bar{1}\bar{1}\bar{1}])$. Applying equation B.1 to each of those pairs results in only four unique vertex stress states since, for example, both $((111), [111])$ and $((\bar{1}\bar{1}\bar{1}), [\bar{1}\bar{1}\bar{1}])$ generate:

$$\mathbf{v} = \begin{bmatrix} 0 & 1 & 1 \\ 1 & 0 & 1 \\ 1 & 1 & 0 \end{bmatrix}.$$

The stress states in family 2 have all zero normal stresses and all shear stresses of equal magnitude, with at most one negative shear. However, these four seemingly unique stress states are in fact indistinguishable from each other when the crystal symmetry is taken into account, as described in Appendix A. Although in finite element simulations it is possible to define a particular orientation for an element or grain and therefore to differentiate between a stress state close to one of these vertices versus another, in an actual material it is impossible to distinguish between symmetrically equivalent orientations, and therefore impossible to

distinguish between these four vertex stresses. The same can be said of the other four vertex families. When performing comparisons between vertex stresses and macroscopic stresses (via equation 4.3) it is necessary to use only one member of each vertex family along with all symmetry operators in $\mathbf{R}^{\text{sym}}$.

BIBLIOGRAPHY

[1] H Ritz, P Dawson, and R Rogge. Measuring the influence of magnesium on the elastic anisotropy of aluminum using *in situ* neutron diffraction. *Journal of Neutron Research*, in press, 2008.

[2] EB Marin and PR Dawson. Elastoplastic finite element analyses of metal deformations using polycrystal constitutive models. *Computer Methods in Applied Mechanics and Engineering*, 165:23–41, 1998.

[3] EB Marin and PR Dawson. On modelling the elasto-viscoplastic response of metals using polycrystal plasticity. *Computer Methods in Applied Mechanics and Engineering*, 165:1–21, 1998.

[4] P Dawson, D Boyce, S MacEwen, and R Rogge. On the influence of crystal elastic moduli on computed lattice strains in AA-5182 following plastic straining. *Materials Science and Engineering*, A313:123–144, 2001.

[5] P Dawson, D Boyce, S MacEwen, and R Rogge. Residual strains in hy100 polycrystals: comparisons of experiments and simulations. *Metallurgical and Materials Transactions*, 31A:1543–1555, June 2000.

[6] B Clausen and MAM Bourke. Lattice plane response during tensile loading of an aluminum 2 percent magnesium alloy. *Metallurgical and Materials Transactions*, 32A:691–694, March 2001.

[7] AK Singh. Analysis of lattice strains measured under nonhydrostatic pressure. *Journal of Applied Physics*, 83(12):7567, 1998.

[8] H-R Wenk, I Lonardeli, J Pehl, J Devine, V Prakapenka, G Shen, and HK Mao. In situ observation of texture development in olivine, ringwoodite,

magnesiowüstite and silicate perovskite at high pressure. *Earth and Planetary Science Letters*, 226(3-4):507–519, 2004.

[9] AD Krawitz. *Introduction to Diffraction in Materials Science and Engineering*. Wiley, New York, 2001.

[10] BD Cullity and SR Stock. *Elements of X-Ray Diffraction*. Prentice Hall, New Jersey, 2001.

[11] WL Bragg. The diffraction of short electromagnetic waves by a crystal. *Proceedings of the Cambridge Philosophical Society*, 17:43–57, 1913.

[12] WF Hosford. *The Mechanics of Crystals and Textured Polycrystals*. Oxford University Press, New York, 1993.

[13] DJ Weidner, L Li, M Davis, and J Chen. Effect of plasticity on elastic modulus measurements. *Geophysical Research Letters*, 31:L06621, 2004.

[14] S Merkel and N Miyajima. Lattice preferred orientation and stress in polycrystalline hcp-co plastically deformed under high pressure. *Journal of Applied Physics*, 100:023510, 2006.

[15] S Merkel and T Yagi. Effect of lattice preferred orientation on lattice strains in polycrystalline materials deformed under high pressure: Application to hcp-co. *Journal of Physics and Chemistry of Solids*, 67:2119–2131, 2006.

[16] NW Ashcroft and ND Mermin. *Solid State Physics*. Thomson Learning, 1976.

[17] W Kurz and DJ Fisher. *Fundamentals of Solidification*. Trans Tech Publications LTD, Switzerland, 1998.

[18] AA Nayeb-Hashemi and JB Clark, editors. *Phase Diagrams of Binary Magnesium Alloys*. ASM International, Metals Park, OH, 1988.

[19] *ASM Handbook: Alloy Phase Diagrams*, volume 3. ASM International, Metals Park, OH, 1992.

[20] UF Kocks, CN Tomé, and H-R Wenk. *Texture and Anisotropy*. Cambridge University Press, 1998.

[21] JF Nye. *Physical Properties of Crystals*. Oxford University Press, London, 1967.

[22] S Matthies, HG Priesmeyer, and MR Daymond. On the diffractive determination of single-crystal elastic constants using polycrystalline samples. *Journal of Applied Crystallography*, 34:585–601, 2001.

[23] W Voigt. *Lehrbuch der Kristallphysik*. Teubner, Berlin, 1928.

[24] A Reuss. Berechnung der fliessgrenze von mishkristallen auf grund der plastizitatsbeding fur einkristalle. *Zeitschrift für Angewandte Mathematik und Mechanik*, 9(1):49, 1929.

[25] E Kroner. Berechnung der elastischen konstanten des vielkristalls aus den konstanten des einkristalls. *Zeitschrift für Physik*, 151:504–518, 1958.

[26] JD Eshelby. *Progress In Solid Mechanics*, volume II. North-Holland, Amsterdam, 1961.

[27] F Bollenrath, V Hauk, and EH Muller. On the calculation of polycrystalline elasticity constants from single crystal data. *Zeitschrift für Metallkunde*, 58 (1):76–82, 1967.

[28] M Hayakawa, S Imai, and M Oka. Determination of single-crystal elastic constants from a cubic polycrystalline aggragate. *Journal of Applied Crystallography*, 18:513–518, 1985.

[29] R de Wit. Diffraction elastic constants of a cubic polycrystal. *Journal of Applied Crystallography*, 30:510–511, 1997.

[30] T Gnaupel-Herold, PC Brand, and HJ Prask. Calculation of single-crystal elastic constants for cubic crystal symmetry from powder diffraction data. *Journal of Applied Crystallography*, 31:929–935, 1998.

[31] HJ Bunge, R Kiewel, Th Reinert, and L Fritsche. Elastic properties of polycrystals - influence of texture and stereology. *Journal of the Mechanics and Physics of Solids*, 48:29–66, 2000.

[32] U Lienert, T-S Han, J Almer, PR Dawson, T Leffers, L Margulies, SF Nielsen, HF Poulsen, and S Schmidt. Investigating the effect of grain interaction during plastic deformation of copper. *Acta Materialia*, 52:4461–4467, 2004.

[33] M Senechal. Which tetrahedra fill space? *Mathematics Magazine*, 54(5): 227–243, 1981.

[34] DP Mika and PR Dawson. Effects of grain interaction on deformation in polycrystals. *Materials Science and Engineering: A*, 257(1):62–76, 1998.

[35] H-R Wenk, editor. *Preferred Orientation in Deformed Metals and rocks: An Introduction to Modern Texture Analysis*. Academic Press, Inc., Florida, 1985.

[36] JR Klepaczko and CY Chiem. On Rate Sensitivity of F. C. C. Metals, Instantaneous Rate Sensitivity and Rate Sensitivity of Strain Hardening. *Journal of the Mechanics and Physics of Solids*, 34(1):29–54, 1986.

[37] UF Kocks. The relation between polycrystal deformation and single crystal deformation. *Metallurgical Transactions*, 1:1121–1143, 1970.

[38] UF Kocks. Polyslip in single crystals. *Acta Metallurgica*, 8:345–352, 1960.

[39] GR Canova, UF Kocks, CN Tome, and JJ Jonas. The Yield Surface of Textured Polycrystals. *Journal of the Mechanics and Physics of Solids*, 33(4): 371–397, 1985.

[40] A Phillips and RL Sierakowski. On the concept of the yield surface. *Acta Mechanica*, 1(1):29–35, 1965.

[41] UF Kocks, GR Canova, and JJ Jonas. Yield vectors in f.c.c. crystals. *Acta Metallurgica*, 31(8):1243–1252, 1983.

[42] SL Altmann. *Rotations, Quaternions, and Double Groups*. Dover Publications, Mineola, New york, 1986.

[43] R Becker. Crystal Rotations Represented as Rodrigues Vectors. *Textures and Microstructures*, 10(3):167–194, 1989.

[44] A Morawiec and J Pospiech. Some information on ouaternions useful in texture. *Textures and Microstructures*, 10:211–216, 1989.

[45] A Kumar and PR Dawson. Computations modeling of f.c.c. deformation textures over rodrigues' space. *Acta Materialia*, 48:2719–2736, 2000.

[46] NR Barton and PR Dawson. A methodology for determining average lattice orientation and its application to the characterization of grain substructure. *Metallurgical and Materials Transactions A*, 32(8):1967–1975, 2001.

[47] MJ Buerger. *Elementary Crystallography*. Wiley & sons, New York, 1978.

[48] JFW Bishop. A theoretical examination of the plastic deformation of crystals by glide. *Philosophical Magazine*, 44:51–64, 1953.